Fission within the Time Dependent Superfluid Local Density Approximation

Ibrahim Abdurrahman

A dissertation
submitted in partial fulfillment of the
requirements for the degree of

Doctor of Philosophy

University of Washington
2022

Reading Committee:
Aurel Bulgac
Silas Beane
Alejandro Garcia

Program Authorized to Offer Degree:
Physics

Abstract

This thesis investigates fission within the framework of the time-dependent superfluid local density approximation (TDSLDA), the most complete microscopic theory to describe low energy nuclear phenomena currently available. This work covers studies of fission for ^{236}U, ^{240}Pu, and ^{252}Cf. We describe their general properties (for ^{236}U, ^{240}Pu): fission fragment (FF) masses, FF charges, TKE, and FF excitation energies; all essential ingredients for describing the properties of emitted neutrons, gammas, and de-excited FFs, all of which are directly measurable by experiment. We also investigated the angular momenta properties of the FFs (for all three systems), including the intrinsic spin distributions, role of orbital angular momenta, and directional correlations between the FF angular momenta vectors. Following, we discussed mathematical features of TDSLDA, including a discussion on chaos within TDSLDA, involving both fission and heavy ion collision case studies, and the role of entropy in TDSLDA. We conclude with a summary of key results, and potential future work.

Contents

1 Introduction

1.1 Discovery of Fission

In 1938, Otto Hahn and Fritz Strassmann discovered nuclear fission by bombarding uranium (Z=92) nuclei with neutrons, causing the reaction to produce barium (Z=56), a much lighter nucleus. Shortly after (in 1939) Lise Meitner and Otto Frisch explained the phenomena theoretically as a competition between Coulomb and surface energies [76]. This explanation was expanded upon by Bohr and Wheeler in the same year [21]. In detail, an excited nucleus will undergo oscillations in it's shape, causing it to elongate. During the elongation, protons begin to move further apart, causing the Coulomb energy to decreases, while the surface energy increases (since the surface area of a shape increases as it deforms away from a sphere for a fixed volume, and the volume of a nucleus remains fixed during the fission process, as it is a mostly incompressible fluid). This competition leads to the formation of a potential barrier (shown in figure 1) beyond which the nucleus will continue to elongate and eventually split into two (or in rare instances more) fission fragments.

This description is semi classical, based on the liquid drop model (LDM), which treats the nucleus as a classically charged liquid drop with the inclusion of the Pauli exclusion principle and pairing. In this model the binding energy of a nucleus is parameterized by the semi empirical mass formula [114]:

$$E_B = -a_v A + a_s A^{2/3} + a_c \frac{Z(Z-1)}{A^{1/3}} + a_A \frac{(N-Z)^2}{A} + \delta(N,Z), \qquad (1)$$

where a_v, a_s, a_c, a_A are parameters fit to experiment or in the case of a_c derived theoretically, and Z, N, A refer to the charge (proton number), neutron number, and mass number (sum of proton and neutron numbers) of the nucleus respectively. The pairing term, $\delta(N,Z)$ is given by:

$$\delta(N,Z) = \begin{cases} -\delta_0 & N,Z \text{ are both even} \\ 0 & A \text{ is odd} \\ \delta_0 & N,Z \text{ are both odd} \end{cases}, \tag{2}$$

where δ_0 (~ 1 MeV for heavy nuclei) is a parameter fit to experimental data.

Equation 1 ignores quantum effects, which lead to additional important correlations, for example classically we would expect the potential to follow the dashed line instead of the solid one in figure 1. The realistic "double hump" potential emerges from shell effects, which cause a local minima to emerge at β_2. As calculations have moved towards more sophisticated microscopic models, which will be discussed in section 1.4, it is still important for all properties of the LDM to be accounted for, namely all microscopic theories must have the correct saturation and surface properties, the Coulomb interaction, asymmetry properties, and include pairing. The importance of pairing, which is crucial for fission, will be argued for in section 1.2.

1.2 Role of Pairing

For attractive, short range, two nucleon forces (the pairing interaction), pairs of time reversed states of opposite angular momenta ($j_z^1 = -m$, $j_z^2 = m$) will form. These cooper pairs represent the most energetically favorable grouping of two nucleons, because the spatial overlaps of the corresponding wave-functions is maximized for states with opposite angular momenta, proven by Maria Goeppert Mayer in 1950 [75]. The proof is as follows, assume a local attractive force between two nucleons,

$$V(\vec{r}_1, \vec{r}_2) = -g\delta(\vec{r}_1 - \vec{r}_2). \tag{3}$$

For simplicity consider the following two particle system, described by an antisymmetric (Fermion) two body wave-function:

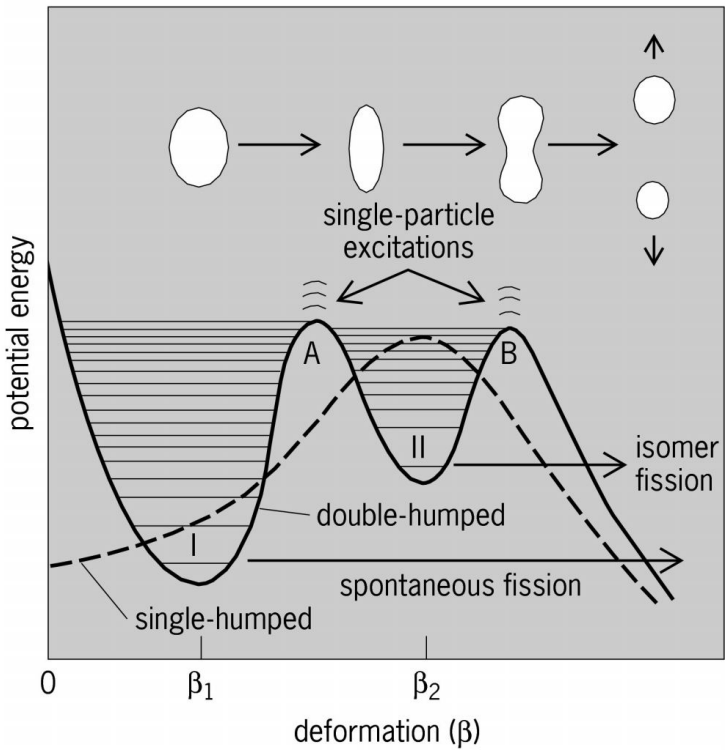

Figure 1: (Color online) Potential energy of a fissioning nucleus as a function of it's deformation along the axis of fission [63] .

$$\Psi(\vec{r}_1, s_1, \vec{r}_2, s_2) = \frac{1}{\sqrt{2}}\Big(\phi_{jm_1}(\vec{r}_1, s_1)\phi_{jm_2}(\vec{r}_2, s_2) - \phi_{jm_2}(\vec{r}_1, s_1)\phi_{jm_1}(\vec{r}_2, s_2)\Big), \quad (4)$$

where j refers to the total angular momenta in given shell, $m_{1,2}$ to it's projection, and we have ignored isospin. The interaction energy is given by,

$$\langle\Psi(\vec{r}_1, s_1, \vec{r}_2, s_2)|V(\vec{r}_1, \vec{r}_2)|\Psi(\vec{r}_1, s_1, \vec{r}_2, s_2)\rangle = -g\int d^3r_1 \sum_{s_1,s_2} \quad (5)$$

$$\Big(|\phi_{jm_1}(\vec{r}_1, s_1)|^2|\phi_{jm_2}(\vec{r}_1, s_2)|^2 - \phi_{jm_1}(\vec{r}_1, s_1)\phi^*_{jm_2}(\vec{r}_1, s_1)\phi^*_{jm_1}(\vec{r}_1, s_2)\phi^*_{jm_2}(\vec{r}_1, s_2)\Big),$$

It is straightforward to verify this term is minimized for $m_1 = -m_2$ pairs. For excitations via thermal neutrons or spontaneous fission, the transitions pairing enables are mandatory for fission. For excitations induced by higher energy neutrons pairing is still needed to obtain correct TKE and FF excitation energy distributions.

To more concretely understand the importance of pairing consider Hill and Wheeler's simplified model of the nucleus introduced in 1953 [62]. In their model, the nucleus is treated as a 3-D infinite square well, representing the attractive nature of the nuclear force (at short range). The volume is fixed, and simultaneously the well is stretched in one direction, the scission axis (the axis the FFs travel after separation). The energy levels of a 3-D infinite are given by:

$$E(n_x, n_y, n_z) = \frac{\pi^2 \hbar^2}{2m}\Big(\frac{n_x^2}{L_x^2} + \frac{n_y^2}{L_y^2} + \frac{n_z^2}{L_z^2}\Big). \tag{6}$$

Without loss of generality, let the scission axis point along the z direction, and the x, y directions be transverse to it. As the nucleus elongates, energy levels with greater transverse components ($n_x, n_y > n_z$) will increase, since L_x, L_y decrease and L_z increases, meanwhile those with smaller transverse components ($n_x, n_y < n_z$) will decrease. If the deformation occurs rapidly, occupied states on increasing levels don't have time to transition to lower lying levels during crossings. As a result, the energy required to deform a nucleus past the outer barrier, where it is guaranteed to scission, will be significantly greater than expected (a reasonable estimate can be obtained from only considering surface and Coulomb energies). Hence, in the case of thermal neutron induced fission or spontaneous fission, the nucleus will not fission, at least not within a realistic timescale (the time to fission will be increased by many orders of magnitude).

Pairing is the only mechanism that allows for the simultaneous transition of paired states during level crossings rather than single nucleons. As a result, nucleons continue to occupy states close to and below the Fermi energy while

the compound elongates, and thus the system requires far less total energy to reach scission (see figure 2). At low temperatures, when nucleons pair up, they form Bosonic compound particles allowing for these transitions to be further enhanced by the Bose enhancement factor [38].

A numerical experiment was performed by Aurel Bulgac et al [38] for the fission of ^{240}Pu using TDSLDA where the initial pairing gap was artificially enhanced for neutrons from 0.73 MeV to 2.57 MeV and for protons from 0.33 MeV to 1.62 MeV. They found the increase in pairing led to a significantly faster scission time, from ~ 14,000 fm/c to ~ 1,400 fm/c.

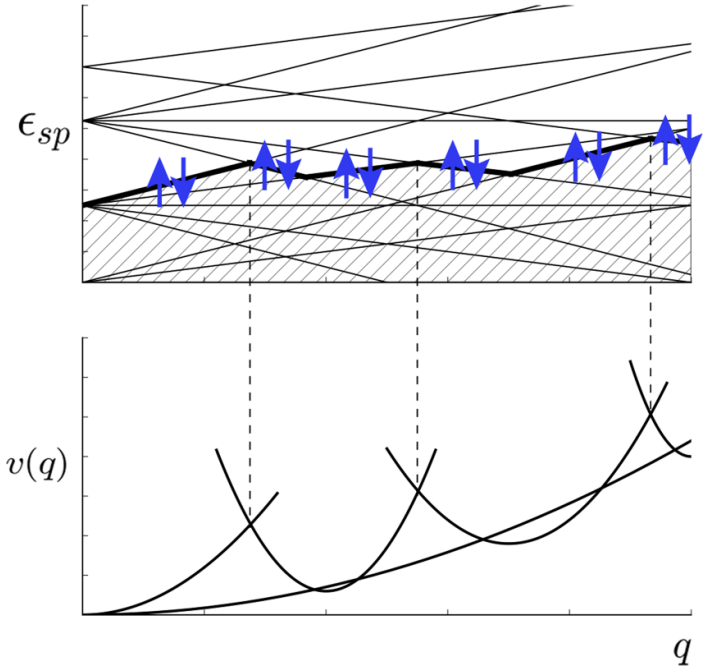

Figure 2: (Color online) The evolution of single particle energy levels as a function of the compound nucleus' deformation during fission [12].

1.3 Fission Time Scales

Fission is a highly complicated process, starting with the formation of the compound nucleus, to it's trajectory towards two separated fission fragments, and ending with the emission of neutrons and gammas (see figure 3). The first part of the process, the formation of the compound, takes at least of the order of 10^7 fm/c for neutron induced fission, and significantly longer for spontaneous fission. This estimate comes from the reaction of ^{235}U + n, where the spacing of energy levels is on average 10 eV [53]. The time it takes for the nucleus to reach the top of the potential barrier is approximated by the uncertainty principle as:

$$\Delta t \geq \frac{\hbar}{\Delta E} \sim 10^7 \text{fm/c}. \tag{7}$$

The fastest part of the process, scission, takes between 10^3 fm/c to 10^4 fm/c (see section 2.4), and currently cannot be probed directly by experiment. After the formation of the FFs, they de-excite, emitting prompt neutrons and gammas beginning at roughly 10^5 fm/c [56]. Scission neutrons pose an additional complication. If they exist they are expected to constitute $\sim 10\%$ of the prompt emitted neutrons [84], with some recent calculations by N. Carjan and M. Rizea suggesting such estimates could vary significantly, meaning the potential contribution of SNs could be much larger [44].

Currently, all parts of the fission process are treated via different theoretical approaches. TDSLDA simulates the formation of the fission fragments, the most non-equilibrium part of the process. Outputs from the simulation; FF masses, FF charges, the total kinetic energy (TKE), FF temperatures (excitation energies), and others; can be used as inputs for phenomenological models FREYA, CGMF (a Hauser Feshbach [59] evaporation code), and others to improve (or at least microscopically motivate) their predictions for the neutron and gamma emission spectra [109], [103]. The beginning of fission, the formation of the compound nucleus is typically treated by the

semiclassical WKB approximation [91] or imaginary time approaches [68], and currently cannot be simulated via TDSLDA due to the enormous separation in time scales between it and the formation of the FFs.

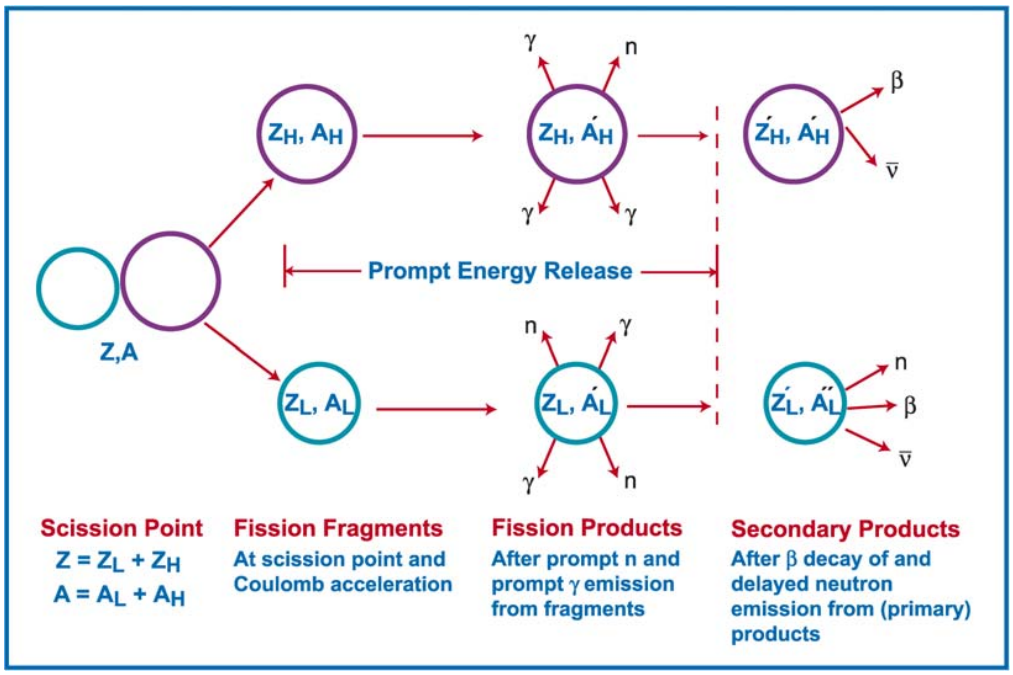

Figure 3: (Color online) Schematic of the fission process from scission to the emission of neutrons and gammas [69] .

1.4 Microscopic Models

Microscopic theories, i.e. quantum models starting at the level of the interactions between nucleons, are powerful tools for understanding nuclear phenomena, especially in regions with sparse or no data. As an example, scission, arguably the most important part of the fission process, occurs at a time scale too fast to be directly observed experimentally. For low energy nuclear physics, all microscopic approaches are derived from Schrödinger's equation, making them completely quantum treatments.

Most such models rely on three assumptions: relativistic effects can be ignored; the independent particle picture is valid, which is equivalent to stating that the many body wave-function can be expressed as a superposition of products of single (or quasi) particle states; and the effects of three body and higher order interactions can be ignored. The first is justified, since the average kinetic energy of a nucleon in a nucleus, given by $\langle \mathrm{KE} \rangle = \langle \frac{\mathrm{h}^2 \mathrm{p}^2}{2\mathrm{m}} \rangle \sim \frac{\mathrm{h}^2 \mathrm{A}^{2/3}}{2\mathrm{m}\mathrm{R}^2} \approx \frac{\mathrm{h}^2}{2\mathrm{m}\mathrm{r}_0^2} \approx 20$ MeV, is small relative to the rest mass of a nucleon ($\sim$ 940 MeV) [8]. The second, since the mean distance between two nucleons in a nucleus ($\sim$ 2.4 fm) is greater than the range of the nuclear interaction ($\sim$ 1.0 fm), if we ignore the Coulomb interaction. This is different than an ordinary liquid, where the two lengths would be roughly equal. This is because nucleons are Fermions, thus the Pauli exclusion principle prevents two or more of them from coming too close to each another, making scattering events rare [89]. This also justifies why three body and higher order interactions can (probably) be neglected: statistically if the probability of two nucleons colliding is small, the probability of three or more colliding must be miniscule.

The following section will cover three microscopic models: Hartree Fock, BCS, and Hartree Fock Bogoliubov. The simplest is **Hartree Fock**, which states that the many body wave function of A interacting nucleons can be decomposed as a anti-symmetric product state (Slater determinant) of A single particle wave functions:

$$\Phi(\vec{r}_1, \vec{r}_2, ...\vec{r}_A) = \frac{1}{\sqrt{A!}} \begin{vmatrix} \phi_1(\vec{r}_1) & \phi_1(\vec{r}_2) & ... & \phi_1(\vec{r}_A) \\ \phi_2(\vec{r}_1) & \phi_2(\vec{r}_2) & ... & \phi_2(\vec{r}_A) \\ ... & ... & ... & ... \\ \phi_A(\vec{r}_1) & \phi_A(\vec{r}_2) & ... & \phi_A(\vec{r}_A) \end{vmatrix}. \tag{8}$$

The Hartree-Fock Hamiltonian is defined by:

$$\hat{\mathrm{H}} = -\frac{\hbar^2}{2\mathrm{m}} \sum_{k=1}^{\mathrm{A}} \nabla_k^2 + \frac{1}{2} \sum_{k \neq n}^{\mathrm{A}} \mathrm{V}(\vec{r}_k, \vec{r}_n), \tag{9}$$

where the interactions are assumed to be local,

$$\mathrm{V}(\vec{r}_1, \vec{r}_2) = t_0 \delta(\vec{r}_1 - \vec{r}_2), \tag{10}$$

with the exception of the Coulomb interaction,

$$\mathrm{V}(\vec{r}_1, \vec{r}_2) = \frac{e^2}{4\pi\epsilon_0 |\vec{r}_1 - \vec{r}_2|}, \tag{11}$$

which depends on the relative distance between two nucleons, and the constant $\frac{e^2}{4\pi\epsilon_0}$ = 1.44 MeV - fm. Some partitioners work with non local interactions, specifically the Gogny interaction (for more details see [48]).

To obtain the Hartree-Fock equations, which are used to obtain the single particle states, which define the many body wave-function, we must solve the variational equation $\delta \mathrm{E} = 0$ where,

$$\mathrm{E} = \langle \Phi | H | \Phi \rangle - \sum_{k=1}^{A} \epsilon_k \int d^3 r |\phi_k(\vec{r})|^2. \tag{12}$$

Solving the variational equation is equivalent to solving Schrodinger's equation.

Expanded out, the system's energy is given by:

$$\mathrm{E} = \int d^3 r \sum_{k=1}^{A} \Big(- \frac{\hbar^2}{2m} \phi_k^*(\vec{r}) \nabla^2 \phi_k(\vec{r}) - \epsilon_k |\phi_k(\vec{r})|^2 \Big) \tag{13}$$

$$+ \int d^3 r \sum_{k=1}^{A} \Big(V^H(\vec{r}) \phi_k^*(\vec{r}) \phi_k(\vec{r}) + \int d^3 r' V^F(\vec{r}, \vec{r}\,') \phi_k^*(\vec{r}) \phi_k(\vec{r}\,') \Big),$$

where,

$$V^H(\vec{r}) = \int d^3 r' v(\vec{r}, \vec{r}\,') \rho(\vec{r}\,'), \tag{14}$$

represents the Hartree component of the interaction, and

$$V^F(\vec{r},\vec{r}\,') = -v(\vec{r},\vec{r}\,')\rho(\vec{r},\vec{r}\,'), \tag{15}$$

represents the Fock (or exchange) component of the interaction. The density matrix is defined by,

$$\rho(\vec{r}_1,\vec{r}_2) = \sum_{k=1}^{A} \phi_k^*(\vec{r}_2)\phi_k(\vec{r}_1), \tag{16}$$

where the diagonal elements define the one body density,

$$\rho(\vec{r}) = \sum_{k=1}^{A} |\phi_k(\vec{r})|^2. \tag{17}$$

The condition $\delta \mathrm{E} = 0$ is equivalent to,

$$\frac{\delta \mathcal{E}(\vec{r})}{\delta \phi_k^*} = 0, \tag{18}$$

where $\mathcal{E}(\vec{r})$ is known as the energy density functional (EDF) and related to the system energy via,

$$\mathrm{E} = \int d^3r \mathcal{E}(\vec{r}). \tag{19}$$

The EDF, $\mathcal{E}(\vec{r})$, is explicitly defined by equations 13 and 19. Then equation 18 leads to the Hartree-Fock equations,

$$\Big(-\frac{\hbar^2}{2m} + V^H(\vec{r})\Big)\phi_k(\vec{r}) + \int d^3r' V^F(\vec{r},\vec{r}\,')\phi_k(\vec{r}) = \epsilon_k \phi_k(\vec{r}). \tag{20}$$

Importantly, the Hartree Fock equations are self consistent, meaning the potentials depend on the single particle wave functions. As a result, to solve equation 20 we need an initial guess for either the densities, potentials, or wave-functions, and have to iterate on the solution until it converges. In practice, especially for extremely deformed nuclei using HFB (discussed later), this procedure is highly non trivial.

Hartree-Fock theory accounts for some of the long range part of the nu-

clear interaction, leading to particle-hole correlations. It does this by demanding all levels below the Fermi energy be fully occupied and all levels above be fully unoccupied. To treat the short range part of the force, leading to particle particle correlations, we must turn to a theory which includes pairing [89].

BCS theory was developed by Bardeen, Cooper, and Schrieffer in 1957 to explain superconductivity [6], and was applied to nuclei by Bohr, Mottelson, and Pines in 1958 [20], and Belyaev in 1959 [10]. Described in Ring and Schuck are six experimental facts which motivate the need for pairing in nuclei [89]. First, there is a gap of around 1 MeV between the low lying excited states of odd nuclei vs even-even nuclei. Second, theory overestimates the level density in the low lying excitation region by roughly a factor of two. Third, the binding energies of odd-even nuclei are smaller than the average of the binding energies of their closest even-even neighbors. Fourth, theory at the time underestimated the moments of inertia of deformed nuclei by a factor of two, and with pairing the agreement becomes much better. Fifth, in order to obtain deformed nuclei we want to partially occupy shells. Hartree-Fock only considers closed shell configurations. And sixth, there exists low lying 2^+ excitations for even-even systems, which are strongly tied to pairing correlations.

What follows is some brief formalism of the BCS Model as presented by Ring and Schunck [89]. Afterwards, the connection to a few experimental facts listed above will be made. Consider the BCS ground state wavefunction,

$$|\mathrm{BCS}\rangle = \prod_{k>0} \left(u_k + \nu_k a_k^\dagger a_{\bar{k}}^\dagger\right) |-\rangle \,. \tag{21}$$

The vacuum is given by $|-\rangle$; u_k, ν_k represent variational parameters; and $a^\dagger{}_k, a^\dagger{}_{\bar{k}}$ represent creation operators for levels k and conjugate levels $\bar{k}$. For systems where the Hamiltonian is time reversal invariant the conjugate states are given by,

$$|\bar{k}\rangle = T\,|k\rangle\,, \tag{22}$$

and specifically for fermions by,

$$\begin{bmatrix} \phi_{\bar{k}\uparrow}(\vec{r}) \\ \phi_{\bar{k}\downarrow}(\vec{r}) \end{bmatrix} = i\sigma_y \begin{bmatrix} \phi^*_{k\uparrow}(\vec{r}) \\ \phi^*_{k\downarrow}(\vec{r}) \end{bmatrix}. \tag{23}$$

The BCS Hamiltonian can be expressed as,

$$\mathrm{H} = \sum_{k_1,k_2} t_{k_1,k_2} {a^\dagger}_{k_1} a_{k_2} + \frac{1}{4} \sum_{k_1,k_2,k_3,k_4} \bar{\nu}_{k_1,k_2,k_3,k_4} {a^\dagger}_{k_1} {a^\dagger}_{k_2} a_{k_3} a_{k_4}, \tag{24}$$

where the variation,

$$\delta \left\langle \mathrm{BCS} \middle| \left(\mathrm{H} - \mu \hat{\mathrm{N}}\right) \middle| \mathrm{BCS} \right\rangle = 0, \tag{25}$$

leads to the BCS equation,

$$2\tilde{\epsilon}_k u_k v_k + \Delta_k(\nu_k^2 - u_k^2) = 0, \quad k > 0 \tag{26}$$

and the energy parameter $\tilde{\epsilon}_k$ and gap Δ_k are given by,

$$\tilde{\epsilon}_k = \frac{1}{2}\Big(t_{kk} + t_{\bar{k}\bar{k}} + \sum_{k'} (\bar{\nu}_{k,k',k,k'} + \bar{\nu}_{\bar{k},k',\bar{k},k'}) v_{k'}^2\Big), \tag{27}$$

$$\Delta_k = -\sum_{k'>0} \bar{\nu}_{k,\bar{k},k',\bar{k}'} u_{k'} v_{k'}. \tag{28}$$

The solutions to equation 24 are,

$$v_k^2 = \frac{1}{2}\Big(1 - \frac{\tilde{\epsilon}_k}{\sqrt{\tilde{\epsilon}_k^2 + \Delta_k^2}}\Big), \tag{29}$$

$$u_k^2 = \frac{1}{2}\Big(1 + \frac{\tilde{\epsilon}_k}{\sqrt{\tilde{\epsilon}_k^2 + \Delta_k^2}}\Big). \tag{30}$$

To illustrate briefly the success of the pairing model in nuclei let us re-

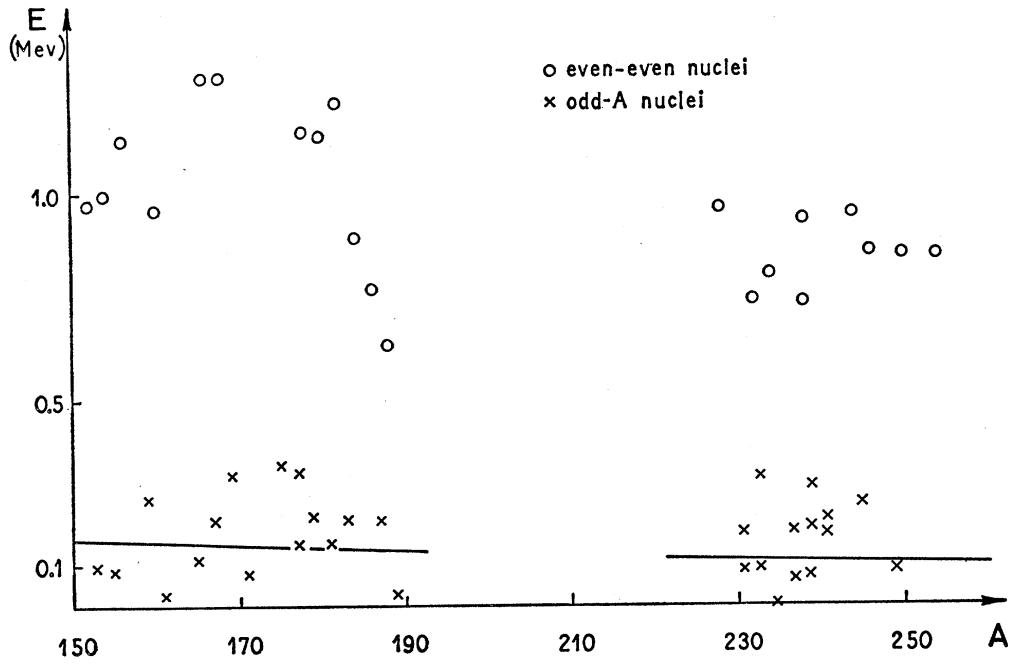

Figure 4: Energies of the first excited intrinsic states in deformed nuclei as a function of the mass number [20].

visit two of the phenomena mentioned above and justify them. First, the staggering between the binding energies of odd-even and even-even nuclei. The binding energy of a pair is 1-2 MeV. For odd-even nuclei, one nucleon is always unpaired, hence lowering the nucleus' total binding energy. Second, if we want to excite an even-even nucleus we would need to break up a pair, which accounts for the gap between the low lying excited states of even-even and odd-even nuclei.

In Hartree-Fock we considered a collection of independent particles moving through a mean potential. In BCS we introduced the concept of quasi-particles and the pairing operator leading to particle-particle correlations. **Hartree-Fock Bogoliubov theory (HFB)** unifies both approaches, where now the many body wave-function is comprised of a generalized product of

independent quasi-particles.

The Bogoliubov quasi-particles, introduced in [19], are connected via a linear transformation to the bare/real particles of the system (fundamental or composite particles, such as nucleons in a nucleus). In the absence of pairing, quasi-particles with $E_k < E_F$, where E_F refers to the Fermi energy, correspond to particles, and quasi-particles with $E_k > E_F$ correspond to holes. If pairing is non zero their physical interpretation becomes hazy. It is important to note the Bogoliubov quasi-particles are only approximate eigenfunctions of the many body Hamiltonian [89]. Then, strictly speaking, it follows that they have no precise physical interpretation. In order to be exact. one should use the Landau-Migdal quasi-particles [67], [77] which have no simple relationship to the bare particles of the system. Regardless, the Bogoliubov quasi-particles, are still immensely useful as a tool when studying Fermi systems, and some insight into a roughly true interpretation can be derived.

What follows will be a brief overview of HFB theory. The many body wave-function $|\Phi\rangle$ for the ground-state of a nucleus is defined as the vacuum with respect to the quasiparticle operators,

$$\beta_k |\Phi\rangle = 0. \tag{31}$$

The quasiparticle operators are related to the particle operators via,

$$\beta_k^\dagger = \sum_l \left[U_{lk} c_l^\dagger + V_{lk} c_l \right]. \tag{32}$$

Then given the Hamiltonian,

$$H = \sum_{k_1,k_2} t_{k_1,k_2} c_{k_1}^\dagger c_{k_2} + \frac{1}{4} \sum_{k_1,k_2,k_3,k_4} \bar{v}_{k_1,k_2,k_3,k_4} c_{k_1}^\dagger c_{k_2}^\dagger c_{k_3} c_{k_4}, \tag{33}$$

with the minimization condition,

$$\delta \frac{\langle \Phi | H - \mu \hat{N} | \Phi \rangle}{\langle \Phi | \Phi \rangle} = 0, \tag{34}$$

we arrive at the HFB equations,

$$\begin{bmatrix} h & \Delta \\ -\Delta^* & -h^* \end{bmatrix} \begin{bmatrix} U_k \\ V_k \end{bmatrix} = E_k \begin{bmatrix} U_k \\ V_k \end{bmatrix}, \tag{35}$$

where,

$$h_{k,k'} = \langle \Phi | [c_k, H], c^\dagger_{k'} | \Phi \rangle \,, \tag{36}$$

$$\Delta_{k,k'} = \langle \Phi | [c_k, H], c_{k'} | \Phi \rangle \,, \tag{37}$$

E_k represent the eigenvalues of the matrix in equation 35, and U_k, V_k are column vectors of the transformation matrices in equation 32.

2 Overview of Fission within TDSLDA

2.1 Theoretical Framework

This section will explicitly overview the theoretical framework of static SLDA and TDSLDA. For more details see [65], which covers LISE, the first program to implement TDSLDA. Additionally, although the focus here is TDSLA applied to fission, the LISE code can also be used to model heavy-ion collisions, neutron star crusts, or cold atom systems with little to no modifications [41] [36] [25] [35] [39]. The program can be found on GitHub [98].

Begin by considering the set of quasi-particle wave-functions,

$$\Psi_k = \begin{bmatrix} u_{k\uparrow}(\vec{r}) \\ u_{k\downarrow}(\vec{r}) \\ v_{k\uparrow}(\vec{r}) \\ v_{k\downarrow}(\vec{r}) \end{bmatrix}. \tag{38}$$

The ground state solution, or in the case of a constrained calculation, the lowest energy solution for fixed deformations, is given by the minimization condition,

$$\frac{\partial \mathcal{E}\big[n(\vec{r}), \tau(\vec{r}), \kappa(\vec{r}), \vec{s}(\vec{r}), \vec{J}(\vec{r}), \vec{j}(\vec{r})\big]}{\partial \Psi_k} = 0, \tag{39}$$

where $\mathcal{E}$ is known as the nuclear energy density functional (NEDF) of the system, and depends on the following densities and currents: the number density $n(\vec{r})$, the kinetic density $\tau(\vec{r})$, the anomalous density $\kappa(\vec{r})$, the spin density $\vec{s}(\vec{r})$, the spin current density $\vec{J}(\vec{r})$, and the current density $\vec{j}(\vec{r})$. The set of densities consist of products and sums of components of the set of quasi particle wave-functions and their derivatives,

$$n(\vec{r}) = \sum_{k,\sigma} v^*_{k,\sigma}(\vec{r}) v_{k,\sigma}(\vec{r}), \tag{40}$$

$$\kappa(\vec{r}) = \sum_{k} v^*_{k,\downarrow}(\vec{r}) u_{k,\uparrow}(\vec{r}), \tag{41}$$

$$\tau(\vec{r}) = \sum_{k,\sigma} \vec{\nabla} v^*_{k,\sigma}(\vec{r}) \cdot \vec{\nabla} v_{k,\sigma}(\vec{r}), \tag{42}$$

$$\vec{s}(\vec{r}) = \sum_{k,s,s'} \vec{\sigma}_{s,s'} v^*_{k,s}(\vec{r}) v_{k,s'}(\vec{r}), \tag{43}$$

$$\vec{J}(\vec{r}) = \frac{1}{2i} \sum_{k,s,s'} \Big(v^*_{k,s'}(\vec{r}) \big[\vec{\nabla} v_{k,s}(\vec{r}) \times \vec{\sigma}_{s,s'} \big] - v_{k,s}(\vec{r}) \big[\vec{\nabla} v^*_{k,s'}(\vec{r}) \times \vec{\sigma}_{s,s'} \big] \Big), \tag{44}$$

$$\vec{j}(\vec{r}) = \frac{1}{2i} \sum_{k,s} \Big(v^*_{k,s}(\vec{r}) \vec{\nabla} v_{k,s}(\vec{r}) - v_{k,s}(\vec{r}) \vec{\nabla} v^*_{k,s}(\vec{r}) \Big). \tag{45}$$

The EDF can be decomposed as a sum of four distinct terms,

$$\mathcal{E} = \mathcal{E}_{\text{kin}} + \mathcal{E}_{\text{interaction}} + \mathcal{E}_{\text{Coul}} + \mathcal{E}_{\text{pair}}. \tag{46}$$

(i) The kinetic term,

$$\mathcal{E}_{\text{kin}} = \sum_{\text{q=n,p}} \frac{\text{h}^2}{2\text{m}_\text{q}} \tau_\text{q}(\text{r}), \tag{47}$$

which is standard across all NEDFs, where often the neutron and proton masses are set equal to an average of the two,

$$\text{m}_\text{q} = \frac{\text{m}_\text{p} + \text{m}_\text{n}}{2}. \tag{48}$$

(ii) The Coulomb term,

$$\mathcal{E}_{\text{Coul}} = \frac{\text{e}^2}{2} \int \frac{\text{n}_\text{p}(\text{r})\text{n}_\text{p}(\text{r}')}{|\text{r} - \text{r}'|} \text{d}^3\text{r}' - \frac{3\text{e}^2}{4}\Big(\frac{3}{\pi}\Big)^{1/3} \text{n}_\text{p}^{4/3}(\text{r}), \tag{49}$$

where sometimes the exchange contribution (second term) is neglected.

(iii) The pairing term,

$$\mathcal{E}_{\text{pair}} = \sum_q g_{q,\text{eff}}(\vec{r}) |\kappa(\vec{r})|^2 \tag{50}$$

where the effective coupling constant $g_{q,\text{eff}}$ is obtained via renormalizing the bare coupling constant [43] [117] [23],

$$\frac{1}{g_{q,\text{eff}}(\vec{r})} = \frac{1}{g_0^{(q)}(\vec{r})} - \frac{m_q^*}{4\pi\hbar^2 a} K, \tag{51}$$

$$g_0^{(q)}(\vec{r}) = g_0^{(q)}\Big(1 - \alpha \frac{n(\vec{r})}{n_0}\Big), \tag{52}$$

and above, m_q^* represents the effective mass, a represents the lattice spacing, $n_0 = 0.16$ fm^{-3} is the saturation density, $\alpha = 0, 0.5, 1$ corresponds to volume, mixed, and surface pairing respectively [50] [14], and K is a transcendental constant defined via,

$$K = \frac{12}{\pi}\int_0^{\pi/4} d\theta \ln(1+1/\cos^2\theta) = 2.442749607806335.... \tag{53}$$

The renormalization scheme, described by equation 51, is an important distinction between SLDA and HFB. Typically, practitioners of HFB deal with the divergence in the pairing field by either introducing a finite range Gogny interaction [47], which greatly complicates any numerical implementation, or imposing a momentum cutoff, which lacks strong physical justifications [43].

(iv) The interaction term, which encodes the majority of the nucleon-nucleon interaction, has numerous suitable choices. For local NEDFs the most common choices come from the Skyrme family [11] [52],

$$\mathcal{E}_{\text{Skyrme}} = \sum_{t=0,1}\Big[C_t^n n_t^2 + C_t^\gamma n_t^2 n_0^\gamma + C_t^{n\Delta n} n_t \Delta n_t + C_t^\tau (n_t\tau_t - j_t\cdot j_t) + C_t^{\nabla J}\Big(n_t \nabla\cdot J_t + s_t\cdot(\nabla\times j_t)\Big)\Big], \tag{54}$$

where for any density ρ, ρ_0 represents the sum of the neutron and proton densities (the isoscalar component), and ρ_1 represents the difference of the neutron and proton densities (the isovector component).

Another attractive choice is the SeaLL1 EDF,

$$\mathcal{E}_{\text{SeaLL1}} = \sum_{j=0}^{2}\Big(a_j n_0^{5/3} + b_j n_0^2 + c_j n_0^{7/3}\Big)\Big(\frac{n_1}{n_0}\Big)^{2j} + \sum_{t=0,t=1}\Big[C_t^{n\Delta n} n_t \Delta n_t + C_t^{\nabla J}\Big(n_t\nabla\cdot J_t + s_t\cdot(\nabla\times j_t)\Big)\Big]. \tag{55}$$

SeaLL1 contains only seven independent parameters, less than other NEDFs, yet has superior accuracy to most Skyrme NEDFs for binding energies, one and two nucleon separation energies, charge radii, and so forth [34]. It contains all of the important components of the interaction term, including the correct volume and surface energies, isospin properties, spin orbit interaction, and symmetry energy. The coefficients for both SeaLL1 and SkM* (a Skyrme EDF well fitted for fission [7]) are contained in table 1. The unlisted

	SeaLL1	SkM*
a_0	0	-
b_0	-684.524043779	-
c_0	827.26287841	-
a_1	64.2474102072	-
b_1	119.862146959	-
c_1	-256.492703921	-
a_2	-96.8354102072	-
b_2	449.22189682	-
c_2	- 461.650174489	-
$g_0^{(p)}$	- 230	-325.90
$g_0^{(n)}$	- 230	-240.99
C_0^{τ}	-	34.6875
C_1^{τ}	-	-34.0625
C_0^{γ}	-	9724.6875
C_1^{γ}	-	-324.8958$\bar{3}$
$C_0^{n\Delta n}$	- 81.3917522003	-68.203125
$C_1^{n\Delta n}$	- 81.3917522003	17.109375
$C_0^{\nabla J}$	- 73.5210618422	-97.5
$C_1^{\nabla J}$	0	-32.5

Table 1: NEDF parameters for SeaLL1 and SkM*.

parameter $\gamma = 1/6$.

The minimization condition defined by equation 39 leads to a set of self-consistent eigenvalue equations, similar to the HFB equations (see section A for an explicit derivation):

$$H(\vec{r})\begin{bmatrix} u_{k\uparrow}(\vec{r}) \\ u_{k\downarrow}(\vec{r}) \\ v_{k\uparrow}(\vec{r}) \\ v_{k\downarrow}(\vec{r}) \end{bmatrix} = \begin{bmatrix} h_{\uparrow\uparrow}(\vec{r}) - \mu & h_{\downarrow\uparrow}(\vec{r}) & 0 & \Delta(\vec{r}) \\ h_{\downarrow\uparrow}(\vec{r}) & h_{\downarrow\downarrow}(\vec{r}) - \mu & -\Delta(\vec{r}) & 0 \\ 0 & -\Delta^*(\vec{r}) & -h^*_{\uparrow\uparrow}(\vec{r}) + \mu & -h^*_{\uparrow\downarrow}(\vec{r}) \\ \Delta^*(\vec{r}) & 0 & -h^*_{\downarrow\uparrow}(\vec{r}) & -h^*_{\downarrow\downarrow}(\vec{r}) + \mu \end{bmatrix} \begin{bmatrix} u_{k\uparrow}(\vec{r}) \\ u_{k\downarrow}(\vec{r}) \\ v_{k\uparrow}(\vec{r}) \\ v_{k\downarrow}(\vec{r}) \end{bmatrix} = E_k \begin{bmatrix} u_{k\uparrow}(\vec{r}) \\ u_{k\downarrow}(\vec{r}) \\ v_{k\uparrow}(\vec{r}) \\ v_{k\downarrow}(\vec{r}) \end{bmatrix}, \tag{56}$$

where μ is the chemical potential, E_k is the quasi particle energy $\langle\Psi_k|H|\Psi_k\rangle$, $h_{\sigma\sigma'}(\vec{r})$ is the local particle-hole Hamiltonian, and $\Delta(\vec{r})$ is the pairing field. The Hamiltonian $h_{\sigma\sigma'}(\vec{r})$ is obtained from functional derivatives of the NEDF, and can be expressed in terms of a set of potentials as,

$$h_q(\vec{r}) = \Big(-\vec{\nabla}\cdot\frac{\hbar^2}{2m_q^*(\vec{r})}\vec{\nabla}+U_q(\vec{r})\Big)-i\vec{W}_q(\vec{r})\cdot(\vec{\nabla}\times\vec{\sigma})+\vec{S}_q(\vec{r})\cdot\vec{\sigma}-i\Big(\vec{\nabla}\cdot\vec{A}_q(\vec{r})+\vec{A}_q(\vec{r})\cdot\vec{\nabla}\Big). \tag{57}$$

Term by term; the effective mass is given by,

$$\frac{\hbar^2}{2m_q^*(\vec{r})} = \frac{\partial\mathcal{E}}{\partial\tau_q(\vec{r})} = \frac{\hbar^2}{2m} + C_0^\tau n_0 + \xi_q C_1^\tau n_1, \tag{58}$$

with $\xi_{n,p} = \pm 1$; the central-part of the mean-field potential $U(\vec{r})$ is given by,

$$U_q(\vec{r}) = \frac{\partial\mathcal{E}}{\partial n_q(\vec{r})} = 2C_0^n n_0+2\xi_q C_1^n n_1+2C_0^\tau\tau_0+2\xi_q C_1^\tau\tau_1+2C_0^{\Delta n}\nabla^2 n_0+2\xi_q C_1^{\Delta n}\nabla^2 n_1 \tag{59}$$

$$+C_0^{\nabla J}\vec{\nabla}\cdot\vec{J}_0+\xi_q C_1^{\nabla J}\vec{\nabla}\cdot\vec{J}_1+C_0^\gamma(\gamma+2)n_0^{\gamma+1}+2\xi_q C_1^\gamma n_1 n_0^\gamma+\sum_{q'=p,n}\frac{\partial g_{q',\mathrm{eff}}(n)}{\partial n_q(\vec{r})}|\kappa_{q'}(\vec{r})|^2,$$

for Skyrme NEDFs, and

$$U_q(\vec{r}) = \frac{5}{3}a_0 n_0^{2/3}+2b_0 n_0+\frac{7}{3}c_0 n_0^{4/3}-\frac{a_1 n_1^2}{3n_0^{4/3}}+\frac{c_1 n_1^2}{3n_0^{2/3}}-\frac{7a_2 n_1^4}{3n_0^{10/3}}-\frac{2b_2 n_1^4}{n_0^3}-\frac{5c_2 n_1^4}{3n_0^{8/3}} \tag{60}$$

$$+\xi_q\Big(\frac{2a_1 n_1}{n_0^{1/3}}+2b_1 n_1+2c_1 n_1 n^{1/3}+\frac{4a_2 n_1^3}{n_0^{7/3}}+\frac{4b_2 n_1^3}{n_0^2}+\frac{4c_2 n_1^3}{n_0^{5/3}}\Big),$$

for the SeaLL1 NEDF; the spin-orbital potential $\vec{W}_q(\vec{r})$ is given by,

$$\vec{W}_q(\vec{r}) = \frac{\partial \mathcal{E}}{\partial \vec{J}_q(\vec{r})} = C_0^{\nabla J}\vec{\nabla} n_0 + \xi_q C_1^{\nabla J}\vec{\nabla} n_1; \tag{61}$$

the time odd potentials are given by,

$$\vec{S}_q(\vec{r}) = \frac{\partial \mathcal{E}}{\partial \vec{s}_q} = C_0^{\nabla J}\vec{\nabla} \times \vec{j}_0 + \xi_q C_0^{\nabla J}\vec{\nabla} \times \vec{j}_1, \tag{62}$$

$$\vec{A}_q(\vec{r}) = C_0^{\tau}\vec{j}_0 + \xi_q C_1^{\tau}\vec{j}_1 + \frac{1}{2}C_0^{\nabla J}\vec{\nabla} \times \vec{s}_0 + \frac{1}{2}\xi_q C_1^{\nabla J}\vec{\nabla} \times \vec{s}_1; \tag{63}$$

and the local pairing field is given by,

$$\Delta_q(\vec{r}) = -g_{q,\text{eff}}(\vec{r})\kappa_q(\vec{r}). \tag{64}$$

For constrained calculations, specifically constraints on the quadrupole and octuple deformations of the compound nucleus for fission,

$$\hat{Q}_{20} = \int d^3r(2z'^2 - x'^2 - y'^2), \tag{65}$$

$$\hat{Q}_{30} = \int d^3r z'(2z'^2 - 3x'^2 - 3y'^2), \tag{66}$$

the Hamiltonian includes Lagrange multipliers,

$$h' = h + \sum_i \lambda_i(\hat{Q}_i - Q_i^{(0)}). \tag{67}$$

To perform time dependent simulations (TDSLDA) the quasi particle energies are promoted to operators $E_k \to i\hbar\frac{\partial}{\partial t}$ leading to the evolution equations,

$$i\hbar\frac{\partial}{\partial t}\begin{bmatrix} u_{k\uparrow}(\vec{r}) \\ u_{k\downarrow}(\vec{r}) \\ v_{k\uparrow}(\vec{r}) \\ v_{k\downarrow}(\vec{r}) \end{bmatrix} = \begin{bmatrix} h_{\uparrow\uparrow}(\vec{r}) - \mu & h_{\downarrow\uparrow}(\vec{r}) & 0 & \Delta(\vec{r}) \\ h_{\downarrow\uparrow}(\vec{r}) & h_{\downarrow\downarrow}(\vec{r}) - \mu & -\Delta(\vec{r}) & 0 \\ 0 & -\Delta^*(\vec{r}) & -h^*_{\uparrow\uparrow}(\vec{r}) + \mu & -h^*_{\uparrow\downarrow}(\vec{r}) \\ \Delta^*(\vec{r}) & 0 & -h^*_{\downarrow\uparrow}(\vec{r}) & -h^*_{\downarrow\downarrow}(\vec{r}) + \mu \end{bmatrix}\begin{bmatrix} u_{k\uparrow}(\vec{r}) \\ u_{k\downarrow}(\vec{r}) \\ v_{k\uparrow}(\vec{r}) \\ v_{k\downarrow}(\vec{r}) \end{bmatrix}. \tag{68}$$

If required, the system can be given an overall momentum boost via (more important for heavy ion collisions),

$$\begin{bmatrix} u_{k\sigma}(\vec{r}) \\ v_{k\sigma}(\vec{r}) \end{bmatrix} \rightarrow \begin{bmatrix} e^{\frac{i\vec{R}(t)\cdot\vec{p}}{\hbar}} & 0 \\ 0 & e^{\frac{-i\vec{R}(t)\cdot\vec{p}}{\hbar}} \end{bmatrix}\begin{bmatrix} u_{k\sigma}(\vec{r}) \\ v_{k\sigma}(\vec{r}) \end{bmatrix}. \tag{69}$$

After finishing a time-dependent run, theoretical observables are computed. Many can be related to experimental observables, such as neutron multiplicities, post scission gamma ray spectra, and post neutron emission FF masses and charges, via statistical codes, such as FREYA and CGMF [109], [103]. For fission, there are a few important ones. (i) The fission fragment proton and neutron numbers:

$$N_f = \int_{V_f} n_n(\vec{r}) d^3r, \tag{70}$$

$$Z_f = \int_{V_f} n_p(\vec{r}) d^3r, \tag{71}$$

where V_f refers to the volume containing the FF.

(ii) The mass number of the FF, given by the sum of the proton and neutron numbers

$$A_f = N_f + Z_f. \tag{72}$$

(iii) The total kinetic energy (TKE):

$$\text{TKE} = \frac{1}{2}mA_H\vec{v}_H^2 + \frac{1}{2}mA_L\vec{v}_L^2 + E_{\text{Coul}}, \tag{73}$$

where,

$$\vec{v}_f = \frac{1}{M_f} \int_{V_f} d^3r \vec{j}(\vec{r}), \tag{74}$$

represents the FF's center of mass velocity, and,

$$E_{\text{Coul}} = e^2 \int_L d^3r_1 \int_R d^3r_2 \frac{n_p(\vec{r}_1) n_p(\vec{r}_2)}{|\vec{r}_1 - \vec{r}_2|}, \tag{75}$$

represents the Coulomb energy between the FFs. The subscripts H/L refer to the heavy/light FFs respectively, which is applicable in the case of asymmetric fission (the most common scenario).

(iv) The systems' collective flow energy,

$$E_{\text{coll}} = \sum_q \int d^3r \frac{\hbar^2}{2m} \vec{j}_q^2(\vec{r}). \tag{76}$$

(v) The FF's intrinsic energy,

$$\mathrm{E_{f,int}} = \int_{\mathrm{V_f}} \mathrm{d^3r} \mathcal{E}(\mathrm{r}) - \frac{1}{2} \mathrm{m A_f v_f^2}. \tag{77}$$

(vi) The FF's excitation energy,

$$\mathrm{E_f^*} = \mathrm{E_{f,int}} - \mathrm{E_{gs}}. \tag{78}$$

The ground state energy of a FF is obtained by performing a minimization of the desired NEDF, with no constraints, except on proton and neutron particle numbers, which are now allowed to be non-integer. Typically, an auxiliary/outside code HFBTHO [83], is used to generate such solutions.

(vii) The FF temperatures, are approximately related to the FF excitation energies via Bethe's formula [15],

$$T = \sqrt{\frac{10E^*}{A}}. \tag{79}$$

A few additional observables are recorded to monitor the accuracy of the numerical solutions, including the center of mass position, velocity, and kinetic energy,

$$\vec{r}_{cm} = \frac{\int d^3r \vec{r} n(\vec{r})}{\int d^3r n(\vec{r})}, \tag{80}$$

$$\vec{v}_{\rm cm}(t) = \int d^3r \frac{\hbar \vec{j}(\vec{r},t)}{M}, \tag{81}$$

$$E_{\rm cm} = \frac{1}{2} M \vec{v}_{\rm cm}^2, \tag{82}$$

which should all be close to zero, and the total particle numbers,

$$N = \int n_n(\vec{r}) d^3r, \tag{83}$$

$$Z = \int n_p(\vec{r}) d^3r, \tag{84}$$

which should be close to integers and conserved, and the total energy

$$E_{\rm tot} = \int d^3r \mathcal{E}(\vec{r}), \tag{85}$$

which should also be conserved.

2.2 Numerical Implementation

The static LISE solver is a 3-D coordinate based hybrid CPU/GPU code used to obtain self-consistent initial conditions for fission simulations (or more broadly any low energy nuclear simulations, such as low energy heavy ion collisions). The time-dependent LISE code is used to evolve those initial conditions, and is also a hybrid CPU/GPU code. Both codes are implemented on the lattice using the discrete variable representation (for more details see section B).

The framework for the static solver is described by the flowchart in figure 5. We start with an initial guess for either the quasi-particle wave-functions, densities, or potentials. Typically we use converged densities from HFBTHO, a static HFB solver in the harmonic oscillator basis [83]. The trial densities are used to construct the HFB Hamiltonian, which is diagonalized to obtain a set of quasi-particle wave-functions and energies. Specifically, the Hamiltonian is block cyclically distributed [17] (see section C for details) and diagonalized either via Scalapack [18] (CPU based) or ELPA [71] (GPU based), to obtain a set of new quasi-particle wave-functions.

The new set is used to construct densities, which are used to construct potentials, which are mixed with the prior potentials (usually linearly),

$$\mathbf{V}^{(m)} = \alpha \mathbf{V}^{new} + (1-\alpha)\mathbf{V}^{(m-1)}, \tag{86}$$

which are finally used to construct a new Hamiltonian. The chemical potential is also adjusted between iterations (separately for protons and neutrons) using the Thomas Fermi (TF) approximation:

$$\delta\mu = \frac{2}{3} E_F \frac{N^{(m)} - N}{N}, \tag{87}$$

where $E_F = \frac{h^2 k_F^2}{2m} \approx 35\text{MeV}$ is the Fermi energy of infinite symmetric nuclear matter, and also mixed linearly (as was done for the potentials):

$$\mu^{(m)} = \alpha \mu^{new} + (1-\alpha)\mu^{(m-1)}. \tag{88}$$

The mixing parameter α satisfies:

$$0 \leq \alpha \leq 1, \tag{89}$$

and is typically chosen to be $\alpha = 0.25$ or 0.5 (this helps the solver reach a converged solution significantly faster). The cycle, from the qpwfs to the Hamiltonian, is repeated until the total neutron number, proton number,

and energy reach the desired accuracy, after which, the final quasi-particle wave-functions (qpwfs) are written to disk.

The framework for the time-dependent solver is described by the flow chart in figure 6. The program starts by reading in the qpwfs. They are distributed across the various CPUs, and then copied to GPUs. On each GPU, partial densities are constructed, copied to the corresponding CPU, and globally reduced using MPI to construct the full densities. The densities are then copied back to the GPUs, which are used to construct the mean-field potentials. The mean-field potentials are used to take a step forward in time and obtain new qpwfs. When some physical condition is met, for example in fission when the FFs are well separated, the final qpwfs are written to disk and the program exits. Additionally, the densities are recorded every 10 time steps.

A time step is taken in one of two ways, either by using a series expansion method [74], if we are at the beginning of a simulation or performing a restart, or the ABM method [58], for the rest of the time evolution. The series expansion method uses a predictor-corrector scheme for higher accuracy. At time t, we perform a predictor step using the Hamiltonian H(t) constructed from densities $n(t)$ constructed from qpwfs $\psi_k(t)$:

$$\psi_{\text{pred}} = \exp\Big(- \frac{i}{\hbar} H(t)\Delta t\Big)\psi_k(t). \tag{90}$$

The predictor qpwfs, ψ_{pred}, are used to construct predictor densities, n_{pred}, which are mixed with the previous densities to construct corrector densities:

$$n_{\text{cor}} = \frac{n_{\text{pred}} + n(t)}{2}. \tag{91}$$

The corrector densities are used to construct the corrector Hamiltonian, which is applied on $\psi_k(t)$ to obtain the qpwfs at the next time step:

$$\psi_k(t + \Delta t) = \exp\Big(- \frac{i}{\hbar} H_{\text{cor}}\Delta t\Big)\psi_k(t). \tag{92}$$

The matrix exponential is expanded via:

$$\exp\Big(-\frac{i}{\hbar}H\Delta t\Big) = \sum \frac{(-i)^n}{\hbar^n n!}H^n\Delta t^n, \tag{93}$$

where typically $n = 4$ is chosen.

After 4 time steps the program transitions to the ABM method, which requires only 2 matrix vector products as opposed to 8 matrix vector products for an $n = 4$ series expansion. The error for both methods is of the order $O(\Delta t^5)$. Especially, the ABM method is given by the set of equations:

$$p_{n+1} = \frac{y_n + y_{n-1}}{2} + \frac{\Delta t}{48}(119\dot{y}_n - 99\dot{y}_{n-1} + 69\dot{y}_{n-2} - 17\dot{y}_{n-3}) + \frac{161}{480}(\Delta t)^5 y^{(5)}, \tag{94}$$

$$m_{n+1} = p_{n+1} - \frac{161}{170}(p_n - c_n) + \frac{923}{2880}(\Delta t)^6 y^{(6)}, \tag{95}$$

$$c_{n+1} = \frac{y_n + y_{n-1}}{2} + \frac{\Delta t}{48}(17\dot{m}_{n+1} + 51\dot{y}_n + 3\dot{y}_{n-1} + \dot{y}_{n-2}) - \frac{9}{480}(\Delta t)^5 y^{(5)}, \tag{96}$$

$$y_{n+1} = c_{n+1} + \frac{9}{170}(p_{n+1} - c_{n+1}) - \frac{43}{2880}(\Delta t)^6 y^{(6)}, \tag{97}$$

where p, m, c denote the predictor, modifier, and corrector. The prime marks indicate a time derivative:

$$\dot{y}_n = -\frac{i}{\hbar}y_n, \tag{98}$$

and $y_{n+1} = y(t + \Delta t),\ y_n = y(t),\ y_{n-1} = y(t - \Delta t),\ y_{n-2} = y(t - 2\Delta t)$, etc..

During the evolution a unneeded phase factor is introduced:

$$\exp\Big[-\frac{i}{\hbar}\int_0^t \langle\psi_k(t')|H(t')|\psi_k(t')\rangle\, dt'\Big]. \tag{99}$$

This phase is removed by subtracting the instantaneous qp energy:

$$i\hbar\partial_t\psi_k(t) = [H(t) - \eta_k(t)]\psi_k(t), \tag{100}$$

with,

$$\eta_k(t) = \langle\psi_k(t)|H(t)|\psi_k(t)\rangle\,, \tag{101}$$

to improve the program's numerical accuracy and stability.

Post processing is handled by the LISE post processing code which uses the time-dependent densities to compute observables listed in section 2.4. Recently, post-processing also involves operations performed on wave-functions, specifically projections of good quantum numbers on FFs [31], [30] (for more details see section 3). The LISE projection code has unfortunately not yet been made public.

To conclude this section, we will focus on numerical tests performed using LISE to understand it's accuracy, stability, and scaling capabilities. The first test looked into the dependence of the total energy on the lattice constant, shown in figure 7. Conservation of energy, along with particle number conservation (which is very well conserved for all three lattice constants and thus not shown), are the most clear indicators that the program is both accurate and stable. Note, this doesn't mean results are necessarily correct if energy is conserved, but it acts as a reasonable first check. In the case of the fission of ^{236}U performed on a 30x30x60 fm lattice the energy was conserved to ~ 1 MeV for lattice spacing $a = 1.25$ fm, ~ 0.1 MeV for lattice spacing $a = 1.00$ fm, and ~ 0.01 MeV for lattice spacing $a = 0.75$ fm. In figure 7, for times beyond 1200 fm/c the results become unreliable as parts of the FF neutron densities begin to interact unphysical through the periodic boundary conditions (the tails of the neutron densities reach the edge of the box).

The second numerical investigation deals with time reversal invariance. It is expected, in a perfect realization of TDDFT, time reversal will be a good symmetry, since Schrodinger's equation for isolated systems is time

reversal invariant. In figures 8, 9 we performed simulations of fission and heavy ion collisions, where we evolved the nuclear systems both forward and backwards in time and examined the relative difference in the total energy. The total energy in both cases is recovered with good accuracy: the relative energy difference is 10^{-6} for fission and 10^{-7} or better for heavy ion collisions. For a more complete analysis, one should investigate density differences as a function of time as well.

The third numerical investigation looks into the scaling properties of the TD LISE code, and is characterized by figure 10 . A ^{236}U fission trajectory was run for various numbers of GPUs on Oak Ridge's super computer: Summit [1]. Calculations performed strictly on GPUs, such as partial density calculations and time evolution, exhibit nearly perfect strong scaling. Calculations involving MPI communication, such as global reduction on partial densities, do not.

2.3 General Procedure

TDSLDA fission results are obtained using the following 4 steps procedure: (i) Generating the potential energy surface (PES) using HFBTHO. A PES is generated via many self consistent constrained static calculations. Fission calculations specifically require deformation constraints on β_{20}, β_{30}:

$$\beta_{20} = \frac{\sqrt{5\pi}}{3A(r_0A^{1/3})^2} \int (2z'^2 - x'^2 - y'^2)n(\vec{r})d^3r, \tag{102}$$

$$\beta_{30} = \frac{\sqrt{7\pi}}{3A(r_0A^{1/3})^3} \int z'(2z'^2 - 3x'^2 - 3y'^2)n(\vec{r})d^3r, \tag{103}$$

where $x' = x - x_{cm}$, $y' = y - y_{cm}$, $z' = z - z_{cm}$, and $r_0 = 1.2$ fm. (ii) Trajectories are selected beyond the outer saddle, shown in figure 11 for nuclear systems ^{236}U, ^{240}Pu using EDFs SeaLL1, SkM*. For clarity, sets of initial condition have distinct labels. The white and green points for ^{236}U using SeaLL1 are simply labeled SeaLL1. Similarly the white points for ^{236}U using SkM* are labeled

SkM*. The green points represent trajectories excluded in FF intrinsic spin calculations (see section 3). The white points for ^{240}Pu using SeaLL1 are labeled SeaLL1 1, the red points for ^{240}Pu using SeaLL1 are labeled SeaLL1 2, the white points for ^{240}Pu using SkM* are labeled SkM* 2, and the red points for ^{240}Pu using SkM* are labeled SkM* 1. The white/green points were chosen to have energies close to the outer saddle point. The red points were chosen to cross the potential energy valley. Figure 12 is similar to figure 11, except 1D, showing initial conditions on the minimum energy path as a function of β_{20}. (iii) Then, the compound nuclei are placed on a lattice (static SLDA) and evolved forward in time (TDSLDA). Simulations here were performed on a 30x30x60 lattice with spacing a = 1 fm. A simulation is terminated when the fission fragments reach a center of mass to center of mass separation at 30 fm, after which, (iv) theoretical observables are computed (see section 2.1).

2.4 Observables

In figure 13 we plot the collective flow energy, defined by equation 76, as a function of time for ^{236}U and ^{240}Pu. As the nucleus evolves from the outer saddle point, and elongates, the collective flow energy remains constant until scission. Aurel Bulgac et al. highlighted the importance of this result in prior simulations [38]. Their argument follows: if the collective flow energy is constant, and the total energy, which is the sum of the collective flow energy and intrinsic energy, is conserved, then the intrinsic energy must be constant. The intrinsic energy is given as the sum of the potential energy (minimal energy or a fixed deformation) and heat (excitation energy above the minimum):

$$E_{int} = V(\beta_{20}) + Q. \tag{104}$$

This all implies that the compound nucleus heats up prior to scission. Why is this significant? This result contradicts the adiabatic approximation, foundational for TDGCM [110], which assumes the intrinsic energy of the nucleus remains fixed on the PES, or equivalently the compound stays cold. This is analogous to free falling in the absence of air resistance, where potential energy gets converted, one to one, to collective kinetic energy. The TDSLDA results show the compound heats up, analogous to free falling at terminal velocity, where potential energy gets converted, one to one, to heat. Importantly, if TDSLDA results prove to be true, static calculations cannot be used to describe fission dynamics.

Figures 14 and 15 show β_{20} and β_{30} as functions of time for the FFs of ^{236}U and ^{240}Pu. What's key, shown previously by Bulgac et al [38], is the deformations relax significantly after scission. This has an important influence on the spin properties of FFs [31], highlighting the importance of having well separated FFs, since the deformations stabilize only after the FF center of mass to center of mass distance (the separation distance) reaches ~ 22 fm. Another key observation was described by Scamps et al. [95]. They argue one possible reason the HFF has neutron and proton numbers greater than ^{132}Sn (see table 2) is the presence of shell effects emerging from the large octuple deformation of the HFF at scission.

In tables 2 and 3 we record the following theoretical observables (defined in sections 2.1 and 2.3): the HFF's mass, the HFF's charge, the LFF's mass, the LFF's charge, the HFF's quadrupole deformation, the HFF's octuple deformation, the LFF's quadrupole deformation, the LFF's octuple deformation, the initial total energy, the change in total energy, the compound's ground state energy, the compound's saddle energy, the HFF's excitation energy, the HFF's temperature, the LFF's excitation energy, the LFF's temperature, the TKE, the TXE, the Q value, and the scission time. The FF masses and charges, TKE, and FF temperatures are required for statistical reaction codes [57], [103]. Figure 16 shows the TKE as a function of time,

and figure 17 shows the nuclear ratio (N/Z) for individual trajectories. One surprising feature, discussed previously in [38], is the inconclusive nature of the FF temperatures. For some nuclei/EDF combinations the LFF on average is clearly hotter than the HFF, while for others the trend is reversed, although the difference is less pronounced.

Nuclei	NEDF	Property	A_H	Z_H	A_L	Z_L	β_{20}^H	β_{30}^H	β_{20}^L	β_{30}^L	E_{ini}	$E_{fin} - E_{ini}$
^{236}U	SeaLL1	Mean	133.84	51.73	102.16	40.27	0.08	-0.04	0.67	0.02	-1783.64	0.04
–	–	Std	1.74	0.57	1.74	0.57	0.04	0.02	0.05	0.03	0.62	0.01
–	–	Max	135.93	52.51	106.24	41.60	0.16	-0.02	0.79	0.07	-1782.20	0.07
–	–	Min	129.76	50.40	100.07	39.49	0.02	-0.07	0.57	-0.04	-1784.79	0.02
^{236}U	SKM*	Mean	138.05	53.06	97.95	38.94	0.09	-0.09	0.46	0.01	-1758.11	0.06
–	–	Std	1.16	0.42	1.16	0.42	0.03	0.03	0.10	0.07	0.33	0.02
–	–	Max	139.66	53.66	100.15	39.64	0.16	-0.03	0.62	0.19	-1757.62	0.10
–	–	Min	135.85	52.36	96.34	38.34	0.03	-0.12	0.30	-0.07	-1758.62	0.03
^{240}Pu	SeaLL1 1	Mean	136.41	53.05	103.59	40.96	0.06	-0.04	0.62	-0.00	-1804.23	0.03
–	–	Std	0.65	0.27	0.65	0.26	0.03	0.01	0.04	0.04	1.60	0.04
–	–	Max	137.36	53.43	105.46	41.58	0.16	-0.02	0.69	0.06	-1801.79	0.16
–	–	Min	134.54	52.42	102.65	40.59	0.04	-0.05	0.57	-0.10	-1807.15	-0.00
^{240}Pu	SeaLL1 2	Mean	135.58	52.68	104.42	41.32	0.06	-0.04	0.66	0.06	-1808.76	0.02
–	–	Std	0.47	0.26	0.47	0.26	0.02	0.02	0.04	0.01	1.50	0.01
–	–	Max	136.71	53.21	105.13	41.72	0.09	-0.02	0.73	0.08	-1806.16	0.04
–	–	Min	134.87	52.27	103.29	40.79	0.03	-0.07	0.56	0.03	-1810.70	0.00
^{240}Pu	SKM* 1	Mean	135.20	52.51	104.80	41.49	0.07	-0.05	0.55	0.03	-1778.69	0.06
–	–	Std	2.33	0.74	2.33	0.74	0.06	0.01	0.06	0.02	2.94	0.03
–	–	Max	137.10	53.22	111.56	43.60	0.25	-0.03	0.70	0.06	-1771.31	0.11
–	–	Min	128.44	50.40	102.90	40.78	0.03	-0.07	0.48	-0.00	-1781.21	0.03
^{240}Pu	SKM* 2	Mean	135.69	52.61	104.31	41.39	0.06	-0.05	0.54	0.01	-1780.05	0.04
–	–	Std	1.41	0.52	1.41	0.52	0.02	0.02	0.06	0.02	1.08	0.02
–	–	Max	137.88	53.46	107.34	42.32	0.11	-0.02	0.70	0.05	-1779.24	0.07
–	–	Min	132.66	51.68	102.12	40.54	0.03	-0.07	0.47	-0.01	-1783.35	0.02

Table 2: The mean, standard deviation, maximum, and minimum of the HFF mass, HFF charge, LFF mass, LFF charge, HFF quadrupole deformation, HFF octuple deformation, LFF quadrupole deformation, LFF octuple deformation, initial total energy, and change in energy for fission trajectories of ^{236}U and ^{240}Pu using EDFs SeaLL1 and SkM*.

Nuclei	NEDF	Property	E_{gs}	E_{saddle}	E^*_H	T_H	E^*_L	T_L	TKE	TXE	TKE + TXE	t_{sci}
^{236}U	SeaLL1	Mean	-1785.88	-1780.98	18.73	1.17	15.51	1.23	168.85	34.24	203.09	2515.37
–	–	Std	–	–	5.68	0.18	2.55	0.11	4.95	4.96	1.57	878.64
–	–	Max	–	–	32.57	1.58	19.51	1.40	175.84	47.96	204.76	3936.15
–	–	Min	–	–	11.75	0.93	11.52	1.05	156.43	28.84	199.44	1279.73
^{236}U	SKM*	Mean	-1764.58	-1757.18	15.43	1.05	10.14	1.01	167.24	25.57	192.81	1470.86
–	–	Std	–	–	2.00	0.07	2.90	0.14	3.35	2.31	2.38	297.58
–	–	Max	–	–	18.61	1.16	16.09	1.27	176.61	29.75	197.70	2203.99
–	–	Min	–	–	10.99	0.90	6.88	0.84	163.32	21.09	189.23	1105.22
^{240}Pu	SeaLL1 1	Mean	-1810.36	-1806.46	17.16	1.12	20.32	1.40	175.86	37.48	213.34	1951.49
–	–	Std	–	–	3.69	0.12	2.80	0.10	3.56	4.76	2.29	529.84
–	–	Max	–	–	27.57	1.43	24.99	1.56	180.11	51.12	218.51	3884.45
–	–	Min	–	–	12.57	0.96	14.82	1.19	167.39	32.50	208.63	1667.53
^{240}Pu	SeaLL1 2	Mean	-1810.36	-1806.46	16.06	1.08	15.45	1.22	178.78	31.51	210.29	1521.86
–	–	Std	–	–	2.95	0.10	1.32	0.05	2.35	3.42	1.52	245.17
–	–	Max	–	–	20.94	1.24	18.45	1.33	182.68	37.74	212.41	1848.50
–	–	Min	–	–	12.17	0.95	13.61	1.14	174.67	27.66	207.55	1195.71
^{240}Pu	SKM* 1	Mean	-1786.16	-1778.76	16.60	1.10	12.09	1.07	181.63	28.69	210.31	1691.04
–	–	Std	–	–	3.74	0.12	2.17	0.09	4.69	5.45	3.20	480.43
–	–	Max	–	–	27.15	1.45	17.39	1.29	186.36	42.58	217.81	2908.49
–	–	Min	–	–	12.30	0.95	10.26	0.99	168.41	23.98	206.66	1215.10
^{240}Pu	SKM* 2	Mean	-1786.16	-1778.76	15.69	1.07	12.83	1.10	180.39	28.52	208.91	1289.72
–	–	Std	–	–	1.95	0.07	3.23	0.15	4.35	3.45	2.12	275.53
–	–	Max	–	–	20.10	1.21	18.85	1.35	185.80	33.67	212.39	1796.80
–	–	Min	–	–	13.19	0.99	6.06	0.76	172.71	21.53	205.45	827.30

Table 3: The mean, standard deviation, maximum, and minimum of the ground state energy, saddle point energy, HFF excitation energy, HFF temperature, LFF excitation energy, LFF temperature, TKE, TXE, TKE+TXE (Q value), and scission time for fission trajectories of ^{236}U and ^{240}Pu using EDFs SeaLL1 and SkM*.

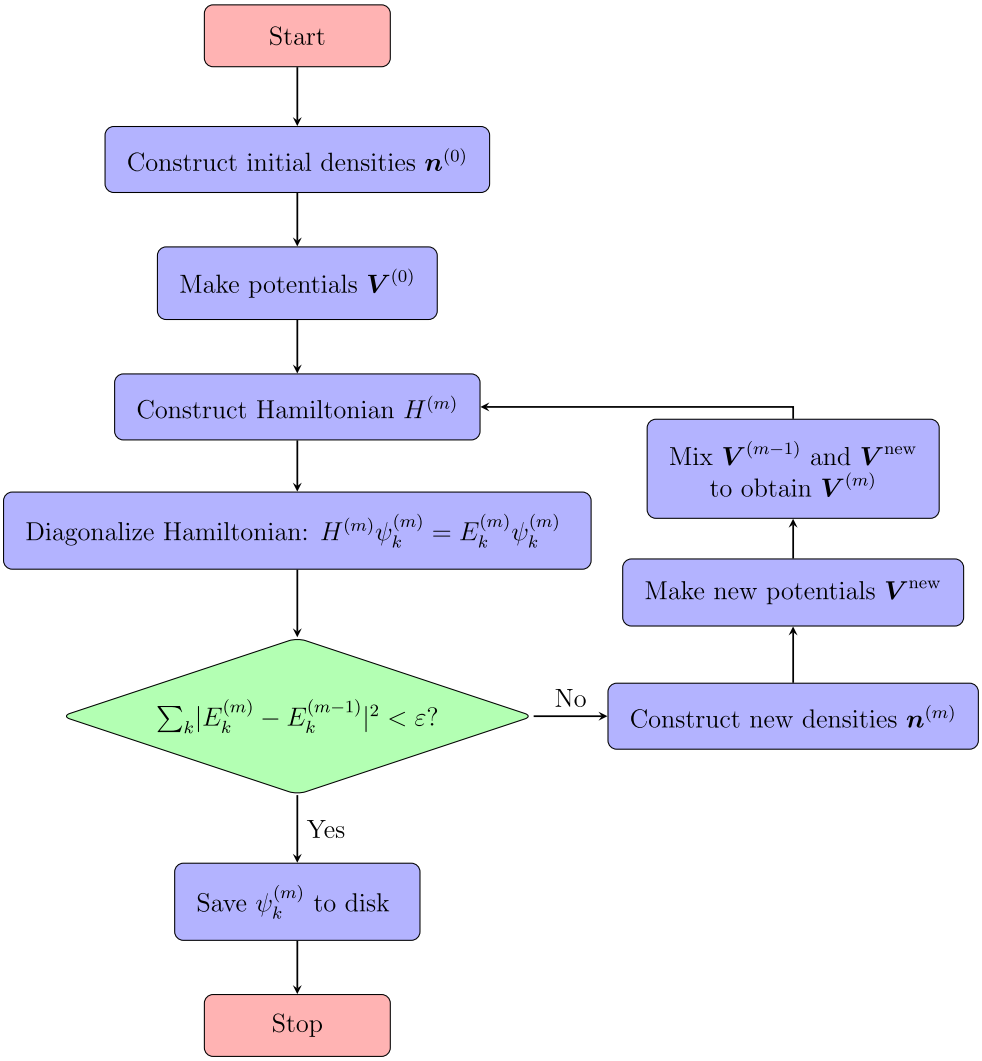

Figure 5: Flowchart of static LISE solver.

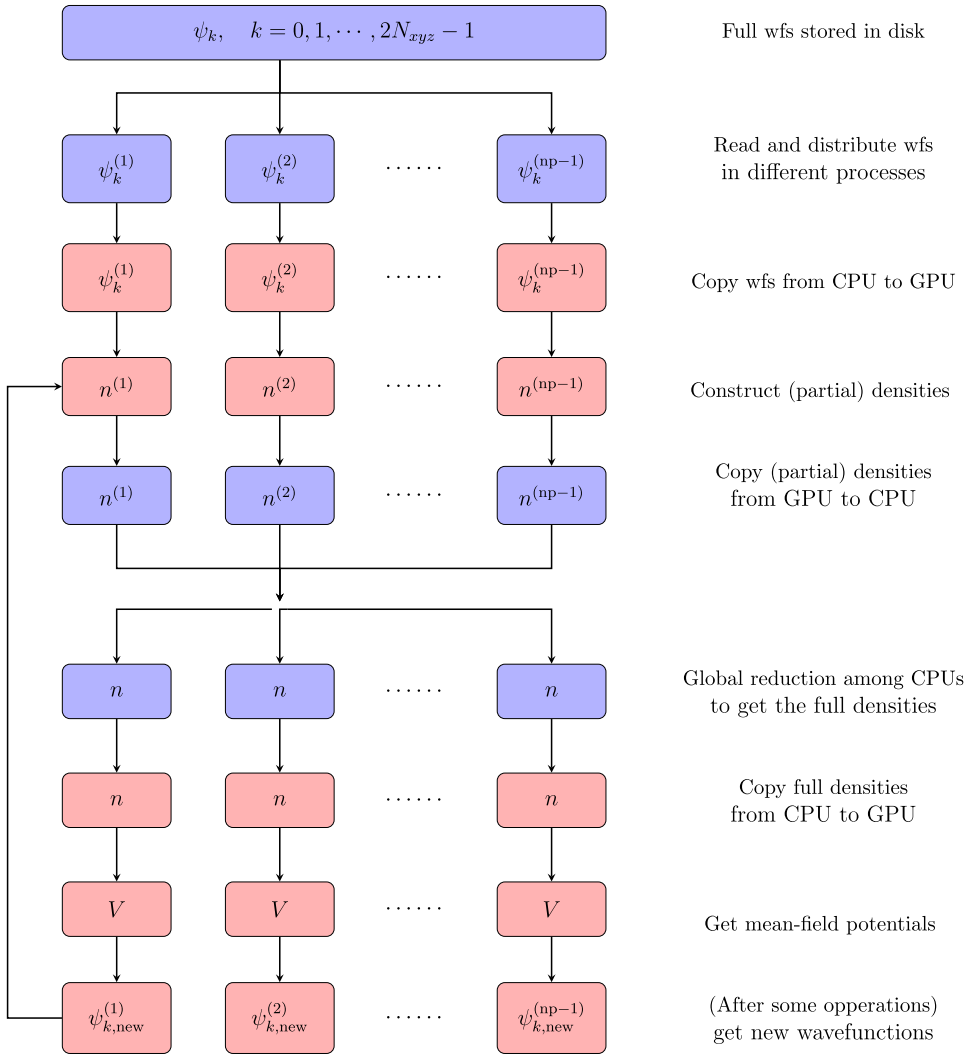

Figure 6: Parallelization structure of the TDSLDA code. The blue and red colored blocks refer to operations performed on either CPUs or GPUs respectively.

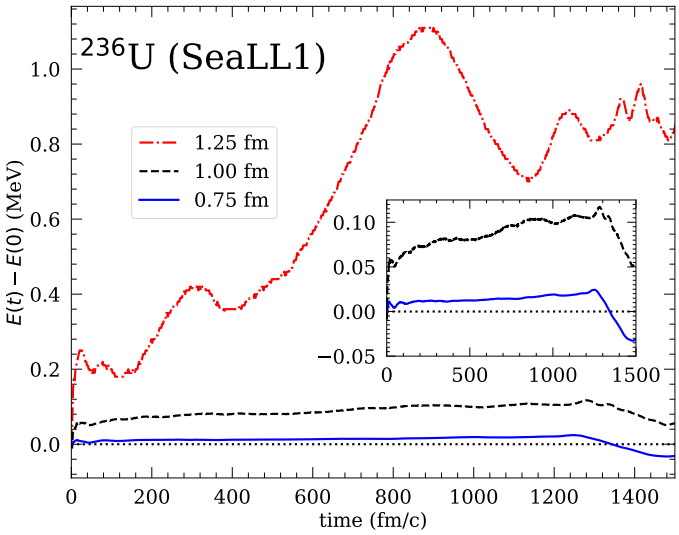

Figure 7: (Color online) Energy conservation of a ^{236}U fission trajectory for three different lattice constants.

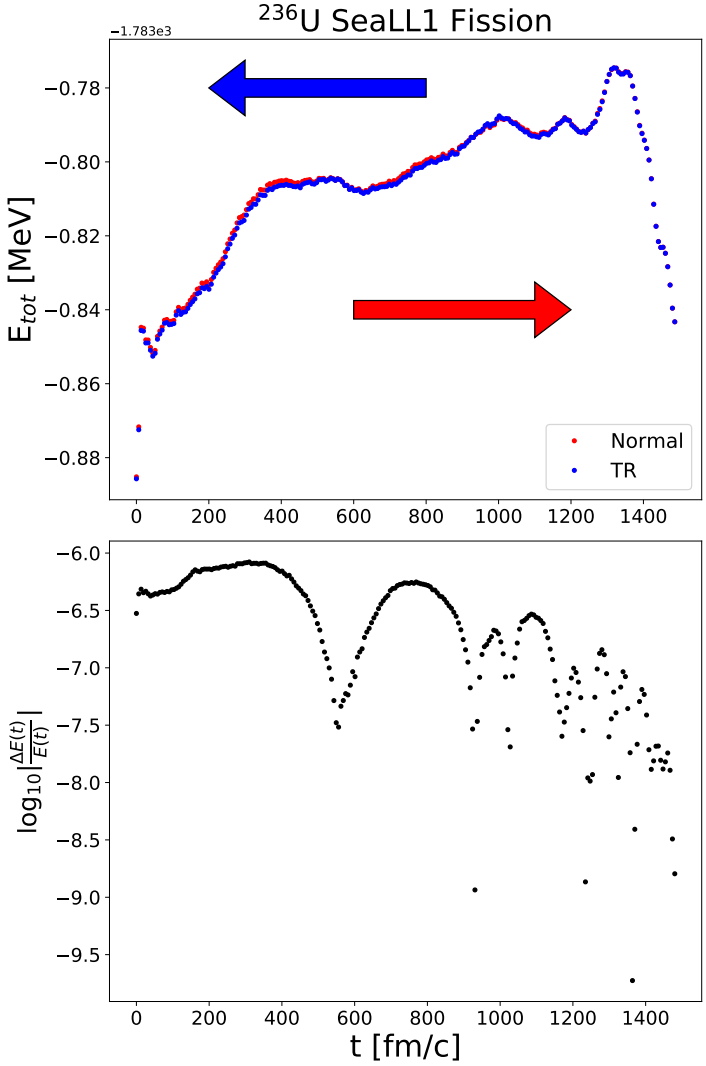

Figure 8: (Color online) Simulations of the fission of ^{236}U using the SeaLL1 EDF on a 30x30x60 lattice with spacing a = 1.00 fm have been performed forward and then backwards in time. The top panel shows the system's total energy as a function of time with the red points indicating the forward direction and the blue points indicating the backward direction. The bottom panel shows the relative difference in the total energies at fixed times.

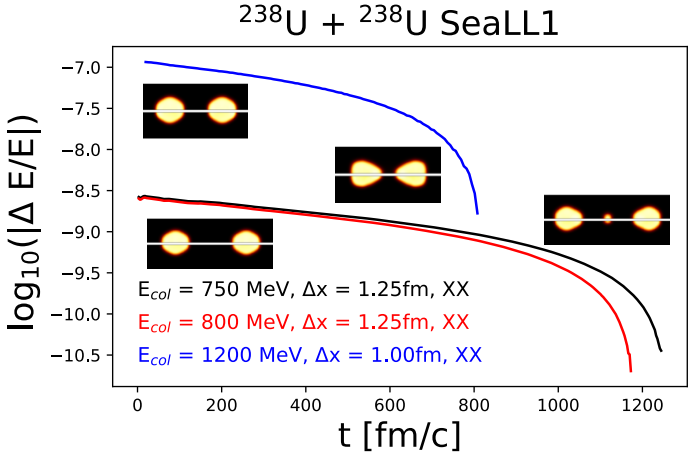

Figure 9: (Color online) Head on collisions of ^{238}U + ^{238}U in the center of mass frame have been performed forward and then backwards in time for two collision energies. The simulations were performed on a 24x24x64 lattice with spacing a = 1.25 fm and on a 30x30x64 lattice with spacing a = 1.00 fm using the EDF SeaLL1. The insets show the initial and final neutron and proton densities. The initial states are shown in the left graphics, and the final states in the right graphics. In each graphic the top/bottom panels represent the neutron/proton densities. The quantity $\Delta E/E_{tot}$ represents the energy difference between the forward and backwards trajectories divided by the total energy of the forward trajectory at a fixed time.

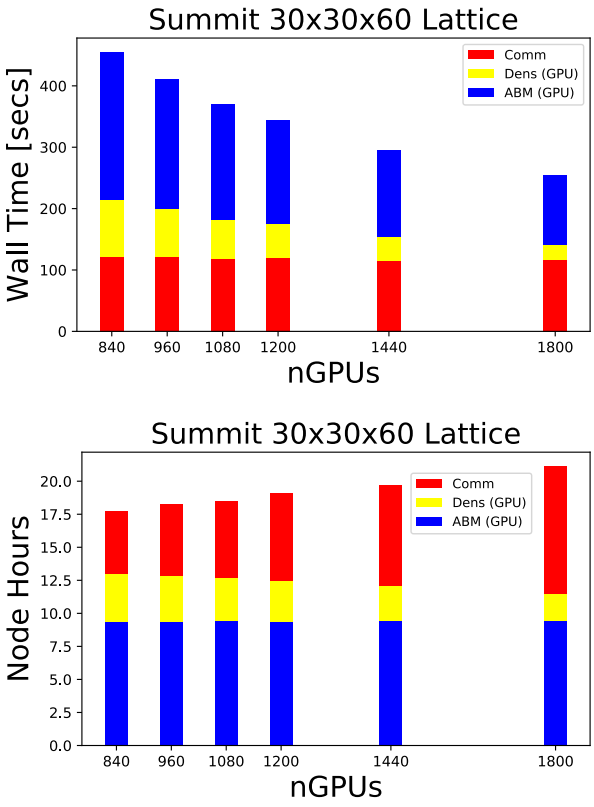

Figure 10: (Color online) Benchmarks for TDSLDA on Summit in the case of ^{236}U fission using the SeaLL1 EDF on a 30x30x60 lattice with spacing $a = 1$ fm. TDSLDA exhibits strong scaling, with the exception of communication performed during partial density reductions.

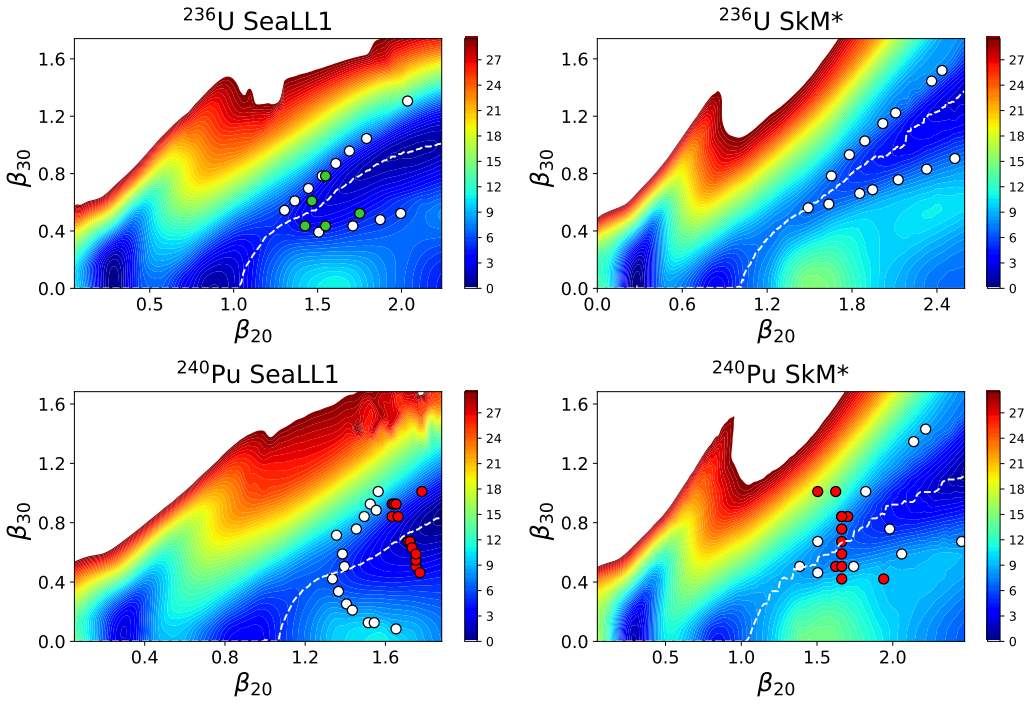

Figure 11: (Color online) Contours represent the difference in energy between a constrained nucleus (nucleus with fixed deformations) and the ground state. The deformations β_{20}, β_{30} are defined by equations 102, 103. The white points were chosen to have energies similar to the outer saddle, with the exception of ^{240}Pu using SeaLL1, where all energies are 1-2 MeV higher. The red points were chosen in a straight line across the PES. The green points for ^{236}U SeaLL1 were not included in the computation of the FF intrinsic spin distributions (see section 3). The white/red points for ^{240}Pu in the lower left panel are denoted by SeaLL1 1/2 respectively. In opposite fashion, the red/white points for ^{240}Pu in the lower right panel are denoted by SkM* 1/2 respectively.

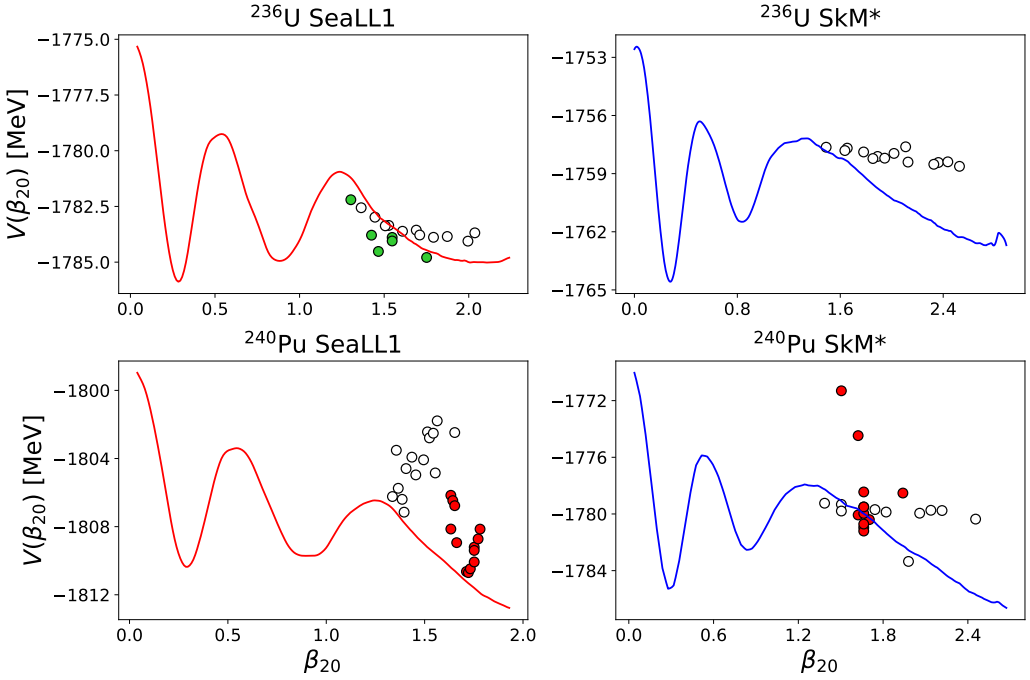

Figure 12: (Color online) The potential was obtained by fixing β_{20} while minimizing the energy with respect to β_{30} along the PES. The points are equivalent to the points in figure 11. The red and blue lines are equivalent to the white dotted lines in figure 11.

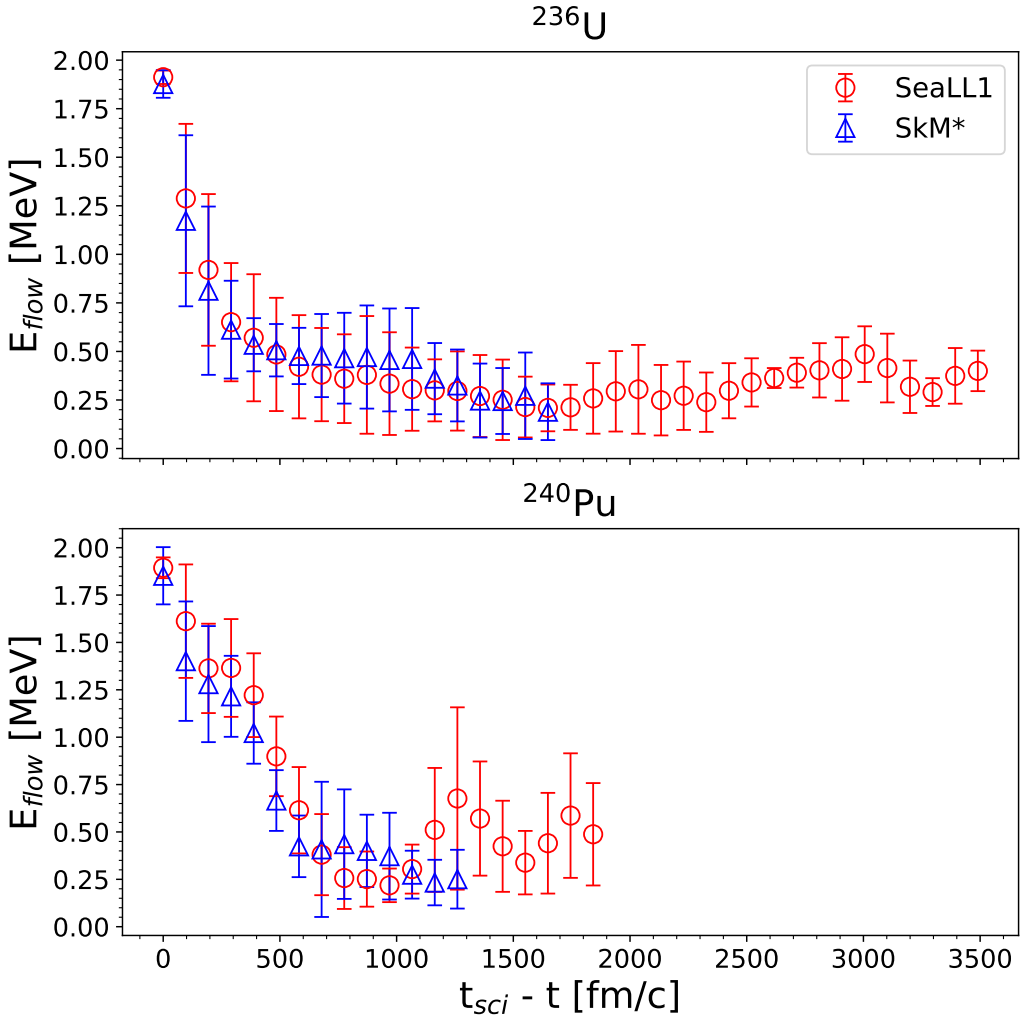

Figure 13: (Color online) Time t runs backwards from scission to the initial state of the compound nucleus, where scission is defined as the point when the flow energy exceeds 2 MeV. For ^{240}Pu, SeaLL1 denotes SeaLL1 1 trajectories, and SkM* denotes SkM* 2 trajectories. The points represent the mean value and the error bars represent the standard deviation.

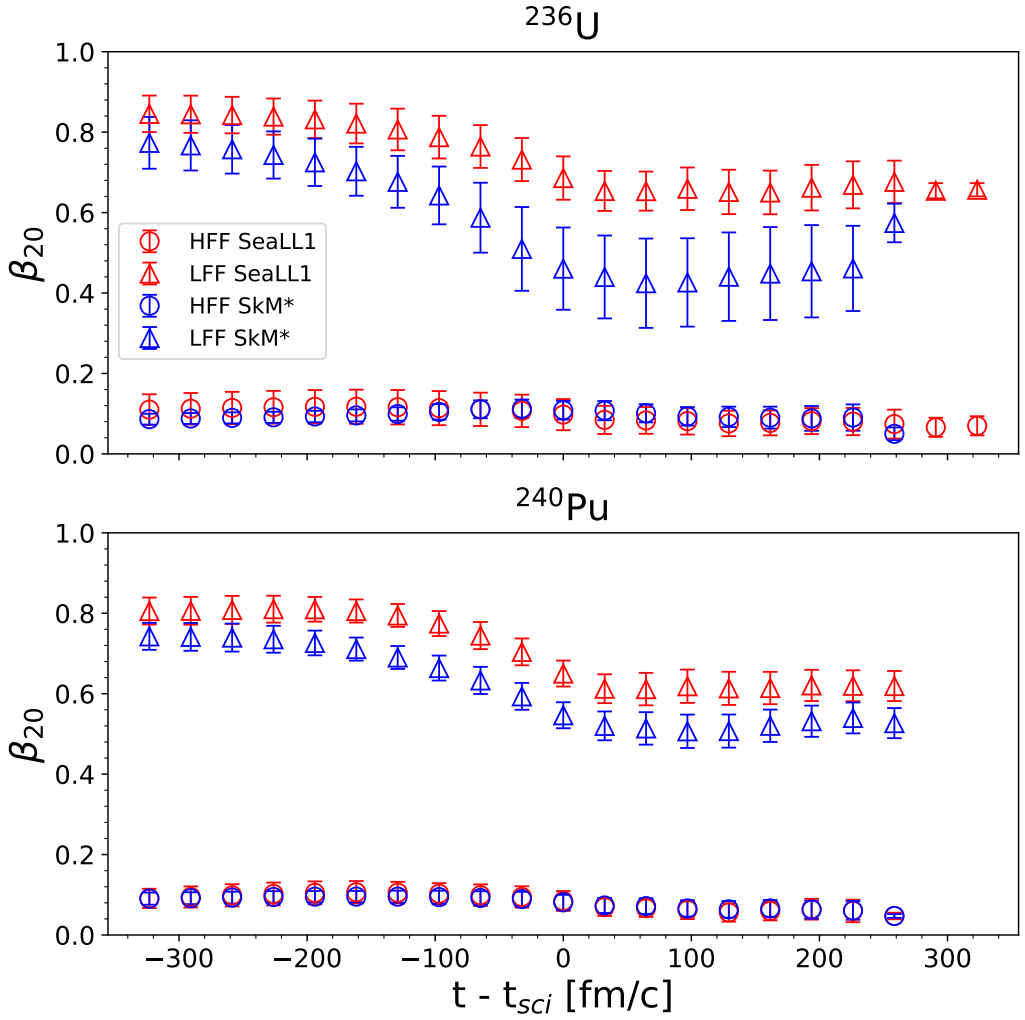

Figure 14: (Color online) The deformation parameter β_{20} as defined by equation 102 for the HFF (circles) and LFF (triangles) for EDFs SeaLL1 (color red) and SkM* (color blue) for ^{236}U (top panel) and ^{240}Pu (bottom panel) as a function of time from scission. For ^{240}Pu, SeaLL1 denotes SeaLL1 1 trajectories, and SkM* denotes SkM* 2 trajectories. The points represent the mean value and the error bars represent the standard deviation.

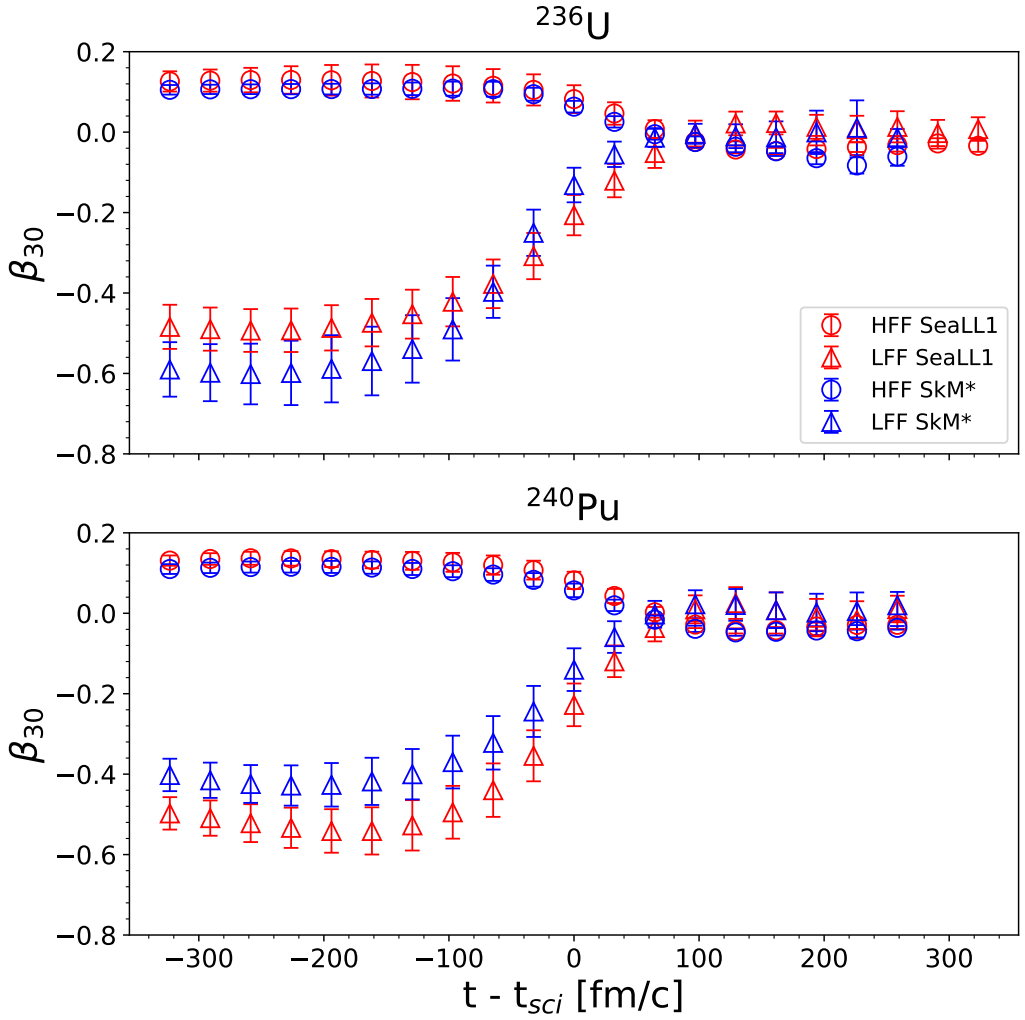

Figure 15: (Color online) The deformation parameter β_{30} as defined by equation 103 for the HFF (circles) and LFF (triangles) for EDFs SeaLL1 (color red) and SkM* (color blue) for ^{236}U (top panel) and ^{240}Pu (bottom panel) as a function of time from scission. For ^{240}Pu, SeaLL1 denotes SeaLL1 1 trajectories, and SkM* denotes SkM* 2 trajectories. The points represent the mean value and the error bars represent the standard deviation.

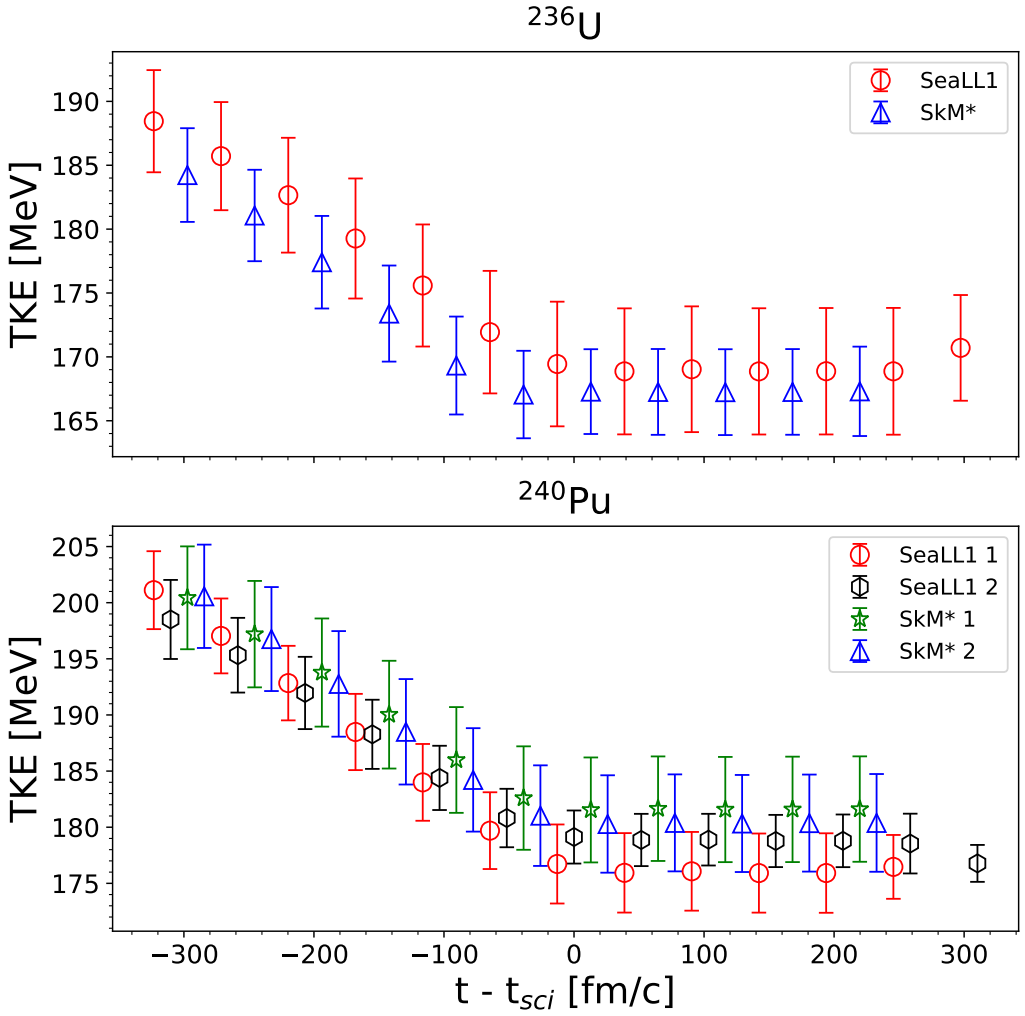

Figure 16: (Color online) The TKE as defined by equation 73. In the top panel results are shown for ^{236}U using SeaLL1 (red circles) and SkM* (blue triangles). In the bottom panel results are shown for ^{240}Pu using SeaLL1 1 (red circles), SeaLL1 2 (black circles), SkM* 1 (green stars), and SkM* 1 (blue triangles). The points represent the mean value and the error bars represent the standard deviation.

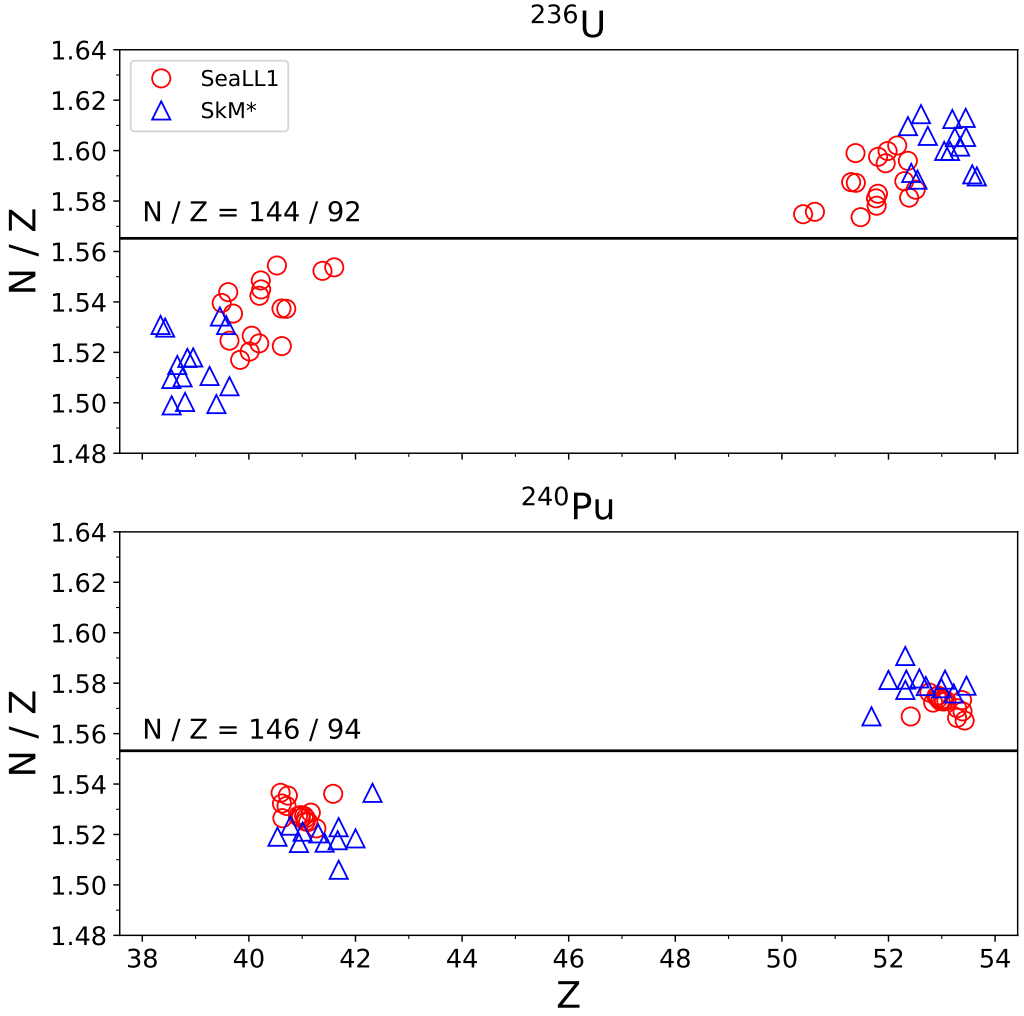

Figure 17: (Color online) In the top/bottom panels FF isomeric ratios are shown for ^{236}U/^{240}Pu respectively. The red circles represent SeaLL1 trajectories and the blue triangles represent SkM* trajectories. For ^{240}Pu, SeaLL1 denotes SeaLL1 1 trajectories, and SkM* denotes SkM* 2 trajectories.

3 FF Spin Properties

3.1 Background and Motivation for Symmetry Restoration

For systems with many particles and strong correlations the treatment of symmetry is a difficult one. We want to simultaneously describe the nucleus (or collection of nuclei) with simple wave functions (or quasi particle wave-functions) such as product states of independent particles moving through mean field potentials, and also capture important correlations and collective effects, such as superfluidity. To encapsulate both into a theoretical framework, symmetries present in real nuclear systems must be abandoned. As an example suppose we demand our system be translationally invariant. If we also want to construct the wave-function as a product of single particle wave-functions, as is the case for a Slater determinant, we are forced to use plane-waves (eigenstates of the momentum operator). Then the system is not localized in space, and hence cannot be used to simultaneous describe bound systems, such as nuclei. In principle we could consider a far more complicated form for the total wave-function, one different from a product state of single particle or quasi-particle wave-functions, which would have good quantum numbers, but in practice such a wave-function is untenable.

As a result we make the choice to use symmetry violating states; to favor collective effects over good quantum numbers. For large systems this is a very good approximation for many quantities, and exact for macroscopic systems. For example, consider the energy of systems with N particles and N + 1 particles, as N increases the percentage of error between the two decreases substantially. As an estimate, consider the systems ^{20}O, ^{21}O and ^{235}U, ^{236}U. ignoring odd-even effects, each nucleon will contribute roughly 7 MeV to the binding energy of the system. For ^{20}O vs ^{21}O the percent difference in energy is ~ 5 %, while for ^{235}U vs ^{236}U it is ~ 0.5 %, one order of magnitude smaller.

Regardless, it is still important to go beyond mean field theory to cap-

ture certain important phenomena [89]. For example, if we want transition probabilities and electromagnetic moments, these cannot be extracted from symmetry violating wave-functions, since some of the transitions will be forbidden based on the quantum numbers of the system and conservation laws. Second the nucleus is a finite system. This means phase transitions are not sharp, but gradual [16]. As an example, consider a closed shell or double magic nucleus. The nucleus is spherical, and hence rotationally invariant. If the lowest open shell is filled with one or two nucleons, the system will slightly deform, weakly violating rational invariance. If half the shell is filled, the system will reach it's maximum deformation, strongly violating rotational invariance. In the region with no symmetry violation or weak symmetry violation it is important to incorporate symmetry correctly. One way to do this is to restore symmetries by projecting the many body wave-function onto eigenstates of the symmetry operators, after evolving the system in an unrestricted manner (in order to avoid hindering collective effects during time evolution).

3.2 Theory for HFB States

This section covers derivations of the projection methods for HFB states presented by Aurel Bulgac in [26] and [28]. To begin, consider particle number projection (pnp). The projector onto a state with N particles is given by,

$$\hat{P}(N) = \int_{-\pi/2}^{\pi/2} \frac{d\eta}{\pi} e^{-i\eta N} e^{-i\eta \hat{N}}. \tag{105}$$

For a HFB wave function $|\Phi\rangle$ the probability to find N particles is then given by:

$$P(N) = \int_{-\pi/2}^{\pi/2} \frac{d\eta}{\pi} e^{-i\eta N} \langle \Phi | \Phi(\eta) \rangle , \tag{106}$$

with $\langle\Phi|\Phi(\eta)\rangle = \langle\Phi|e^{-i\eta\hat{N}}|\Phi\rangle$.

To derive a more explicit form for the overlap element, consider the HFB quasiparticle creation and annihilation operators,

$$\alpha_k^\dagger = \int d\xi\big[u_k(\xi)\psi^\dagger(\xi) + v_k(\xi)\psi(\xi)\big], \tag{107}$$

$$\alpha_k = \int d\xi\big[v_k^*(\xi)\psi^\dagger(\xi) + u_k^*(\xi)\psi(\xi)\big], \tag{108}$$

and peform the following gauge transformation:

$$u_k(\xi,\eta) = u_k(\xi), \quad v_k(\xi,\eta) = e^{2i\eta}v_k(\xi). \tag{109}$$

The operators transform as,

$$\alpha_k^\dagger(\eta) = \int d\xi\big[u_k(\xi)\psi^\dagger(\xi) + e^{2i\eta}v_k(\xi)\psi(\xi)\big], \tag{110}$$

$$\alpha_k(\eta) = \int d\xi\big[e^{-2i\eta}v_k^*(\xi)\psi^\dagger(\xi) + u_k^*(\xi)\psi(\xi)\big], \tag{111}$$

where the field operators are defined via:

$$\psi^\dagger(\xi) = \sum_k \big[u_k^*(\xi)\alpha_k^\dagger + v_k(\xi)\alpha_k\big], \tag{112}$$

$$\psi(\xi) = \sum_k \big[v_k^*(\xi)\alpha_k^\dagger + u_k(\xi)\alpha_k\big]. \tag{113}$$

Substituting equations 112 and 113 into equations 110 and 111 we arrive at:

$$\alpha_k^\dagger(\eta) = A_{kl}\alpha_l^\dagger + B_{kl}\alpha_l, \tag{114}$$

$$\alpha_k(\eta) = B_{lk}^*\alpha_l^\dagger + A_{lk}^*\alpha_l, \tag{115}$$

where,

$$A_{kl} = \Big[\langle u_l | u_k \rangle + \langle v_l | v_k \rangle \, e^{2i\eta} \Big], \tag{116}$$

$$B_{kl} = \Big[\langle v_l^* | u_k \rangle + \langle u_l^* | v_k \rangle \, e^{2i\eta} \Big]. \tag{117}$$

The Onishi and Yoshida formula,

$$\langle \Phi | \Phi(\eta) \rangle = \sqrt{\det A}, \tag{118}$$

can be used to obtain the overlap element:

$$\langle \Phi | \Phi(\eta) \rangle = \sqrt{\det \Big[\delta_{lk} + \langle v_l | v_k \rangle \, (e^{2i\eta} - 1) \Big]}. \tag{119}$$

Importantly, equation 119 and since the overlap matrix $O_{lk} = \langle v_l | v_k \rangle$ for HFB states has double degenerate eigenvalues, projections can only be performed onto even particle numbers.

Similarly projection can be performed onto both the FF and compound simultaneously using the projector:

$$\hat{P}(N, N_F) = \int_{-\pi/2}^{\pi/2} \frac{d\eta}{\pi} e^{-i\eta N} e^{-i\eta \hat{N}} \int_{-\pi/2}^{\pi/2} \frac{d\eta_F}{\pi} e^{-i\eta_F N_F} e^{-i\eta_F \hat{N}_F}, \tag{120}$$

and gauge transformation,

$$u_k(\xi, \eta, \eta_F) = u_k(\xi), \quad v_k(\xi, \eta, \eta_F) = e^{2i\eta} e^{2i\eta_F \Theta(\pm z)} v_k(\xi). \tag{121}$$

The theta function above is used to partition the space into a left and right half, where each should fully contain exactly one fission fragment.

The probability to simultaneously measure the compound with particle number N, and the FF with particle number N_F is then given by,

$$P(N, N_F) = \int_{-\pi/2}^{\pi/2} \frac{d\eta}{\pi} e^{-i\eta N} \int_{-\pi/2}^{\pi/2} \frac{d\eta_F}{\pi} e^{-i\eta_F N_F} \langle \Phi | \Phi(\eta, \eta_F) \rangle \,, \tag{122}$$

with overlap,

$$\langle \Phi | \Phi(\eta, \eta_F) \rangle = \sqrt{\det\Big[\delta_{lk} + (e^{2i\eta} - 1) \langle v_l | v_k \rangle + e^{2i\eta}(e^{2i\eta_F} - 1) \langle v_l | \Theta(\pm z) | v_k \rangle \Big]}. \tag{123}$$

In the case of extracting the FF intrinsic spins we use the projector,

$$\hat{P}(J) = (J + 1/2) \int_0^{\pi} d\eta \sin\eta P_J(\cos\eta) e^{i\hat{J}_x \Theta(\pm z)\eta}, \tag{124}$$

and gauge transformation,

$$u_k(\xi, \eta) = u_k(\xi), \quad v_k(\xi, \eta) = e^{iJ_x \Theta(\pm z)\eta} v_k(\xi). \tag{125}$$

The probability to measure a FF with total angular momentum J is then given by,

$$P(J) = (J + 1/2) \int_0^{\pi} d\eta \sin\eta P_J(\cos\eta) \langle \Phi | \Phi(\eta) \rangle \,, \tag{126}$$

with overlap element,

$$\langle \Phi | \Phi(\eta) \rangle = \sqrt{\det\Big[\delta_{lk} + \langle v_l | (e^{iJ_x\eta} - 1)\Theta(\pm z) | v_k \rangle \Big]}. \tag{127}$$

To extract the orbital angular momenta we begin with conservation of angular momentum,

$$\vec{S}_0 = \vec{\Lambda} + \vec{S}_L + \vec{S}_H, \tag{128}$$

where $\vec{S}_0$ represents the spin of the compound nucleus, $\vec{S}_L$, $\vec{S}_H$ the spins of the light and heavy FFs respectively, and $\vec{\Lambda}$ the orbital angular momenta

between them. To a good approximation,

$$\vec{\Lambda} - \vec{S}_0 \approx \vec{\Lambda} = -(\vec{S}_H + \vec{S}_L) \tag{129}$$

since for most typical nuclei studied $S_0 << |\vec{S}_H + \vec{S}_L|$. For example, for the neutron induced fission of ^{236}U, ^{240}Pu, S_0 is only a few units of $\hbar$ while the sum of the intrinsic spins is around 10 units of $\hbar$ [30]. For the spontaneous fission of ^{252}Cf, S_0 is exactly zero, however even in this case we are using an approximation, since the HFB wave-function exists as superposition of different nuclei and only on average as ^{252}Cf. For exact results particle projection is needed.

Moving forward with this approximate framework, the projector for the orbital angular momenta is given by,

$$\hat{P}(\Lambda) = (\Lambda + 1/2) \int_0^\pi d\eta \sin\eta P_\Lambda(\cos\eta) e^{-i\left[\hat{J}_x^L \Theta^L + \hat{J}_x^H \Theta^H\right]\eta}, \tag{130}$$

with gauge transformation,

$$u_k(\xi,\eta) = u_k(\xi), \quad v_k(\xi,\eta) = e^{-i\left[\hat{J}_x^L \Theta^L + \hat{J}_x^H \Theta^H\right]\eta} v_k(\xi). \tag{131}$$

The probability to measure the system with orbital angular momenta Λ then is,

$$P(\Lambda) = (\Lambda + 1/2) \int_0^\pi d\eta \sin\eta P_\Lambda(\cos\eta) \left\langle \Phi | \Phi(\eta) \right\rangle, \tag{132}$$

with overlap element,

$$\left\langle \Phi | \Phi(\eta) \right\rangle = \sqrt{\det\left[\delta_{lk} + \langle v_l | (e^{iJ_x^L \eta} - 1)\Theta^L | v_k \rangle + \langle v_l | (e^{iJ_x^H \eta} - 1)\Theta^H | v_k \rangle\right]}. \tag{133}$$

To obtain the correlations between the FF intrinsic spins and orbital angular momenta we use the projector,

$$\hat{P}(S_L, S_H, \Lambda) = (S_L + 1/2)(S_H + 1/2)(\Lambda + 1/2) \int_0^\pi d\eta_L \sin\eta_L \int_0^\pi d\eta_H \sin\eta_H \tag{134}$$
$$\int_0^\pi d\eta \sin\eta P_{S_L}(\cos\eta_L) P_{S_H}(\cos\eta_H) P_\Lambda(\cos\eta) e^{-i\left[\hat{J}_x^L \Theta^L(\eta+\eta_L) + \hat{J}_x^H \Theta^H(\eta+\eta_H)\right]}$$

with gauge transformation,

$$u_k(\xi, \eta, \eta_L, \eta_H) = u_k(\xi), \quad v_k(\xi, \eta, \eta_L, \eta_H) = e^{-i\left[\hat{J}_x^L \Theta^L(\eta+\eta_L) + \hat{J}_x^H \Theta^H(\eta+\eta_H)\right]} v_k(\xi). \tag{135}$$

The probability to measure the system with orbital angular momenta Λ, and intrinsic fission fragment spins S_L, S_H is,

$$P(S_L, S_H, \Lambda) = (S_L + 1/2)(S_H + 1/2)(\Lambda + 1/2) \int_0^\pi d\eta_L \sin\eta_L \int_0^\pi d\eta_H \sin\eta_H \tag{136}$$
$$\int_0^\pi d\eta \sin\eta P_{S_L}(\cos\eta_L) P_{S_H}(\cos\eta_H) P_\Lambda(\cos\eta) \left\langle \Phi | \Phi(\eta_L, \eta_H, \eta) \right\rangle,$$

with overlap element,

$$\left\langle \Phi | \Phi(\eta_L, \eta_H, \eta) \right\rangle = \sqrt{\det\left[\delta_{lk} + \langle v_l | (e^{iJ_x^L(\eta+\eta_L)} - 1)\Theta^L | v_k \rangle + \langle v_l | (e^{iJ_x^H(\eta+\eta_H)} - 1)\Theta^H | v_k \rangle\right]}. \tag{137}$$

3.3 FF Intrinsic Angular Momenta

The intrinsic spin distributions of FFs cannot be directly measured in the laboratory, yet significantly influence the neutron and gamma emission spectra of the FFs (consequently a significant portion of the energy released in fission) which can be measured in the laboratory. Their correlations have been investigated since the late 50s for decades [102] [64] [108] [80] [88] [115]

[79] [51] [78] [22] [112], and the debate surrounding them, driven primarily by non-microscopic models, remains unsettled to this day. The most interesting correlations are the various collective angular modes of the FFs: rotating, twisting, wriggling, and bending (see figure 20), whose existence still lacks direct experimental proof.

In [31] we performed the first fully unconstrained microscopic calculation of the FF intrinsic spin distributions in literature (for previous microscopic results see [13]), as well as provided proof for the existence of the aforementioned collective angular momenta modes. Two TDDFT calculations were performed for the fission of ^{235}U(n,f) and ^{239}Pu(n,f) using two different EDFs SkM* and SeaLL1, in boxes with dimensions 30x30x60 and lattice constant Δx = 1 fm. The momentum cutoff is given by $p_{cut} = \frac{\hbar\pi}{\Delta x}$ = 619.92 MeV/c. The initial configurations were chosen at the outer saddle point, and evolved until the FF were separated by 30 fm. The time to go from the saddle point to fully separated FF fragments is of the order of $\sim 10^3$ fm/c. The distributions were obtained from the final wave-functions using equation 126 and are shown in figure 18.

The distributions show that the LFF carries more spin on average than the HFF. This is exactly opposite to what two leading phenomenological models, FREYA [57] and CGMF [103], assumed at the time of publication. A reasonable explanation is that the LFF emerges from scission significantly more deformed than the HFF (see table 4). In the intrinsic (rest) frame of a fragment, deformations determine it's spin, with a highly deformed nucleus carrying more angular momenta per nucleon than a less deformed nucleus, and a spherical nucleus carrying identically zero. The heavy fragment likely emerges less deformed due to Shell effects, since the number of protons and neutrons for most trajectories fall close to the double magic nucleus ^{132}Sn, which in it's ground state is spherical, and recall deformations are maximized for half filled shells.

Comparing with experiment, TDSLDA spins are larger in value than

Nucleus	NEDF	S^L	S^H	β_2^L	β_2^H
^{236}U	SeaLL1	10.5 (0.6)	6.8 (0.7)	0.67 (0.07)	0.09 (0.04)
^{236}U	SkM*	8.6 (0.6)	6.3 (0.7)	0.46 (0.10)	0.09 (0.03)
^{236}U	SkM*	10.4 (0.3)	6.7 (0.5)	0.62 (0.04)	0.06 (0.03)
^{236}U	SkM*	9.4 (0.4)	5.8 (0.5)	0.54 (0.06)	0.06 (0.03)

Table 4: The averages (standard deviations) of the fragment spins and quadrupole deformations, with the later defined by $\beta_2 = \frac{4\pi}{3A(1.2A^{1/3})^2}\int d^3rn(\vec{r})r^2Y_{20}(\vec{r})$.

recent results obtained by Wilson et al [116]. They measure the spins of the FFs post neutron and gamma emission, and then correct for the spin removed by both sources to obtain the intrinsic distribution. This correction is potentially where a discrepancy arrises, with a recent study showing that neutrons could be expected to remove 2 $\hbar$ of angular momentum from each fragment [99]. If this amount of removal turns out to be realistic, TDSLDA values become comparable with experiment.

Currently this remains the only microscopic approach suitable for computing accurate FF spin distributions. Static approaches [72] run into an issue of requiring a finite neck to avoid a discontinuity in the PES. In order to obtain steady FF spins, the shapes of the fragments must be allowed to relax, which only occurs after they are well separated. From previous studies performed with TDSLDA [38], it is known the deformations relax significantly after scission, and the inset of figure 18 shows the spins follow, with the LFF/HFF losing 2/1 units of $\hbar$ of angular momenta respectively after scission.

An additional study was performed for ^{240}Pu, where the incident neutron energy was varied from ~ 0 MeV (thermal) to ~ 24 MeV (see figure 19), causing the spins to increase for both the LFF and HFF. On average the LFF's spin will increase by 1 unit of $\hbar$ for every 60 MeV of excitation energy (with respect to the saddle point), and the HFF's spin will increases by 1 unit

Nucleus	NEDF	S^L	S^H	β_2^L	β_2^H
^{236}U	SeaLL1	10.5 (0.6)	6.8 (0.7)	0.67 (0.07)	0.09 (0.04)
^{236}U	SkM*	8.6 (0.6)	6.3 (0.7)	0.46 (0.10)	0.09 (0.03)
^{236}U	SkM*	10.4 (0.3)	6.7 (0.5)	0.62 (0.04)	0.06 (0.03)
^{236}U	SkM*	9.4 (0.4)	5.8 (0.5)	0.54 (0.06)	0.06 (0.03)

Table 5: The averages (standard deviations) of $\langle\Phi|J_\alpha^L J_\alpha^H|\Phi\rangle$, with $\alpha = x, y, z$.

of $\hbar$ for every 13 MeV of excitation energy. From this it seems the average spin of the FFs is not significantly influenced by the excitation energy of the compound nucleus.

The last topic of investigation is the collective angular momenta modes. Components of the tensor $\langle\Phi|J_\alpha^L J_\alpha^H|\Phi\rangle$ are recored in table 5. The off diagonal elements are negligible and were excluded. Elements $\langle\Phi|J_x^L J_x^H|\Phi\rangle$ and $\langle\Phi|J_y^L J_y^H|\Phi\rangle$ are double degenerate and correspond to the wriggling mode (if positive) or bending mode (if negative). The element $\langle\Phi|J_z^L J_z^H|\Phi\rangle$ corresponds to the tilting mode (if positive) and twisting mode (if negative). All three components of the tensor are negative, confirming for the first time, by a microscopic theory, the existence of both twisting and bending modes.

3.4 Role of Orbital Angular Momenta

In the 1960s it was conjectured that the intrinsic spins of the FFs post scission are controlled by their collective spin modes. Despite this, the origin of the relative orbital angular momenta between FFs has never been explored within a fully microscopic framework, until recently [30]. On it's way to scission the compound nucleus elongates and eventually splits into two fragments. The longer the elongation, for a fixed value of the orbital angular momentum Λ, the greater the inertia of the system, and hence the slower the system's rotation about the center of mass (consider $\Lambda = I\omega$). Until scission, the FF intrinsic spins and orbital angular momenta can vary, so long as the

condition $\vec{\Lambda} + \vec{S}^L + \vec{S}^H = \vec{S}_0$ (where $\vec{S}_0 = 0$ for ^{252}Cf) is respected. After scission all three angular momenta values remain fixed, baring the slight influence of the Coulomb interaction, until after neutron and gamma emission. Before emission and post scission the picture becomes analogous to a person standing on a freely rotating stand ($\vec{\Lambda}$) holding two bicycle wheels ($\vec{S}^{L,H}$).

In figure 21 we compute the orbital angular momenta of ^{236}U, ^{240}Pu, and ^{252}Cf for two EDFs, SkM* and SeaLL1, using equation 132. All simulations were performed on a 30x30x60 lattice with spacing $a = 1$ fm. The distributions of the FF orbital angular momenta are the first extraction of these quantities from a microscopic theory in literature. The distributions of the three systems are similar, because the compound nuclei all have similar masses. In figure 22 we performed a triple projection on both FF intrinsic spins and orbital momenta, defined by equation 136, with the inclusion of the constraint:

$$|S^L - S^H| \leq \Lambda \leq S^L + S^H. \tag{138}$$

This was also the first such calculation of its kind. Two types of correlations are present in figure 136: the tilting of the ellipses for fixed orbital angular momenta values, representing intrinsic correlations, and the sharp rectangular regions representing geometric correlations (caused by an imposition of the triangle constraint defined by equation 138).

Additionally, for ^{252}Cf, the intrinsic spin distributions were computed using two methods (see figure 23). In the first, a single projection was performed as defined by equation 126, similar to previous work [31]. In the second correlated 1-D distributions were computed by summing over two degrees of freedom, for example, the intrinsic spin distribution of the LFF is given by,

$$P(S^L) = \frac{\sum_{S^H,\Lambda} P(S^L, S^H, \Lambda)\Delta}{\sum_{S^L,S^H,\Lambda} P(S^L, S^H, \Lambda)\Delta}, \tag{139}$$

$$\Delta = \Theta(\Lambda \geq |S^L - S^H|)\Theta(\Lambda \leq S^L + S^H). \tag{140}$$

Between the two distributions the most noticeable difference is the suppression of the lower angular momenta modes when correlations are included. The suppression comes from the geometric constraint (equation 138), which restricts the number of available states (values of Λ) for fixed S_L, S_H. Specifically for small values of S_L, S_H, there are fewer allowed values of Λ, hence the number of available orbital angular momenta states acts as a weight factor.

To see this more explicitly consider a simplified example. Let the triple spin distribution be given by:

$$P_S(S^L, S^H, \Lambda) = P_S(S^L)P_S(S^H)P_S(S^\Lambda), \tag{141}$$

where S denotes uncorrelated angular momenta distributions obtained via method one (defined above). Two different intrinsic spin distributions can be defined for the LFF (with similar definitions for the HFF and orbital momenta):

$$P_S(S^L) = \frac{\sum_{S^H,\Lambda} P_S(S^L, S^H, \Lambda)}{\sum_{S^L,S^H,\Lambda} P_S(S^L, S^H, \Lambda)} = f_S(S^L)P_S(S^L), \tag{142}$$

with $f_S(S_L) = 1$, and,

$$P_T(S^L) = \frac{\sum_{S^H,\Lambda} P_S(S^L, S^H, \Lambda)\Delta}{\sum_{S^L,S^H,\Lambda} P_S(S^L, S^H, \Lambda)\Delta} = f_T(S^L)P_S(S^L), \tag{143}$$

with $f_T(S_L)$ shown in figure 24. The factor $f_T(S^L) < 1$ for $S^L < 6\hbar$ and $S^L > 17\hbar$, and $f_T(S^L) > 1$ for $6\hbar < S^L < 17\hbar$. This factor, emerging purely from geometric constraints, clearly suppresses both low and high AM modes, while slightly enhancing middle AM modes (those closer to the mean AM values of the FF intrinsic spin distributions and orbital momenta distributions). Note, current statistical models assume the following form for the spin distributions:

$$P_S(S) = (S + \frac{1}{2})\exp\Big(\frac{-S(S+1)}{2B^2}\Big), \tag{144}$$

where B depends on the FF masses, charges, and temperatures [103]. The above distribution must be modified to include the factor $f_T(S)$ in order to accurately describe the FF intrinsic spin distributions i.e. no choice of B will lend to a functionally correct form for the spin distributions.

In literature it is assumed that the two intrinsic spins are weakly correlated [113], [87]. In the case of FF intrinsic spin magnitude correlations (see figure 25):

$$P(S^L, S^H) = \sum_{\Lambda} P(S^L, S^H, \Lambda)\Delta, \tag{145}$$

TDSLDA confirms these assumptions. However, for correlations between the FF intrinsic spin vectors, this isn't the case. The opening angle distribution (angle between the FF intrinsic spin vectors) is shown in figure 28 and given by:

$$\cos\phi^{LH} = \frac{\Lambda(\Lambda+1) - S^L(S^L+1) - S^H(S^H+1)}{2(S^L+1/2)(S^H+1/2)}, \tag{146}$$

The black and red circles represent TDSLDA results, where there was found to be a strong preference for the angle to be between 0.4 π rads and 0.8 π rads, and zero probability for it to be exactly 0 rads or π rads. If the correlations are weak the distribution would be mostly isotropic or flat. This is represented by the blue line, produced by FREYA [87], which assumes the FF spin dynamics are governed by the rotation energy,

$$E_{rot} = \frac{\vec{S}^L \cdot \vec{S}^L}{2I^L} + \frac{\vec{S}^H \cdot \vec{S}^H}{2I^H} + \frac{\Lambda \cdot \Lambda}{2I^R}, \tag{147}$$

where $I^{L,H,R}$ are the FFs and orbital moments of inertia, with $I^R \approx 10I^{L,H}$, causing the contribution from the orbital component to be insignificant. However, the most general form for the rotation energy is provided by:

$$E_{rot} = (S^L, S^H, \Lambda)^T \otimes \overleftrightarrow{I} \otimes (S^L, S^H, \Lambda), \tag{148}$$

where $\overleftrightarrow{I}$ is a 3x3 non diagonal inertia tensor, and these additional terms should be accounted for. Another way to understand the differences between the TDSLDA and FREYA results is as follows: the distribution from FREYA is similar to the distribution of the angle between two randomly generated 2D vectors; the distribution from TDSLDA is similar to the distribution of the angle between two randomly generated 3D vectors, with the caveat that a completely random distribution would be symmetric with a mean value of 0.5 π rads, unlike the TDSLDA case which is skewed with a mean value of ~ 0.6 rads. The debate over which interpretation is correct is ongoing, with the hope that future experiments can settle the matter.

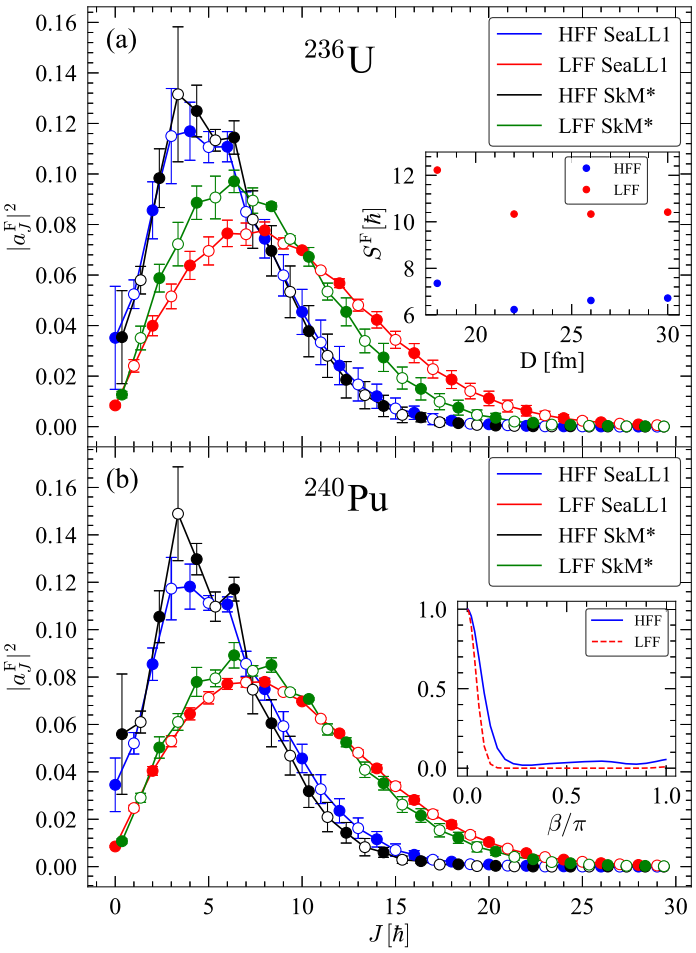

Figure 18: (Color online) The top/bottom panels show the spin distributions for ^{236}U and ^{240}Pu respectively. The blue/black lines represent the spin distributions for the heavy fission fragment for EDFs SeaLL1/SkM*, while the red/green lines represent the spin distributions for the light fission fragment for EDFs SeaLL1/SkM*. The inset in the top panel shows the average spin, defined by $S^{L,H} = \sqrt{\sum_J J(J+1)P_{L,H}(J) + 1/4} - 1/2$, for a single trajectory as a function of the FF separation distance. The inset in the bottom panel shows the overlap element $\langle\Phi|\Phi(\eta)\rangle$ as a function of the rotation angle for both FF fragments.

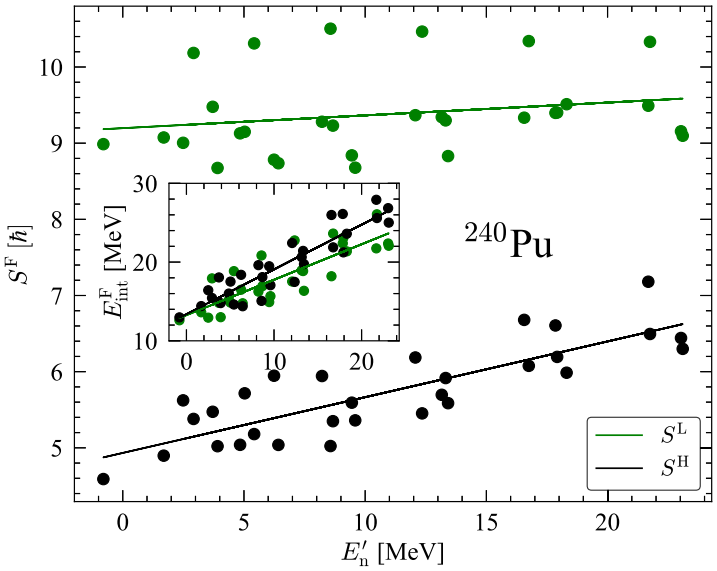

Figure 19: (Color online) The average FF intrinsic spins vs the incident neutron energy $E'_n = E^* - S_n$, where E^* is the compound's excitation energy and S_n is the neutron separation energy for the reaction $^{239}\mathrm{Pu}(n, f)$ with the SkM* NEDF. The inset contains the FF excitation energies versus the incident neutron energy.

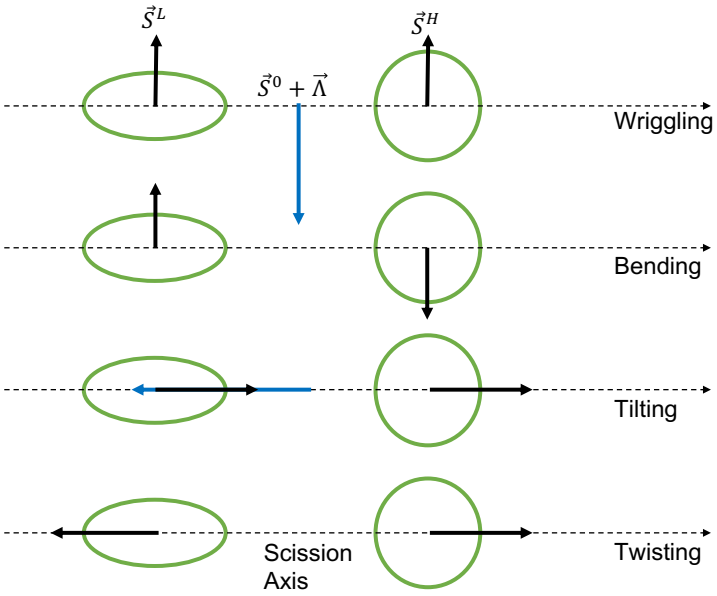

Figure 20: (Color online) Various collective angular momenta modes: wriggling, bending, tilting, and twisting.

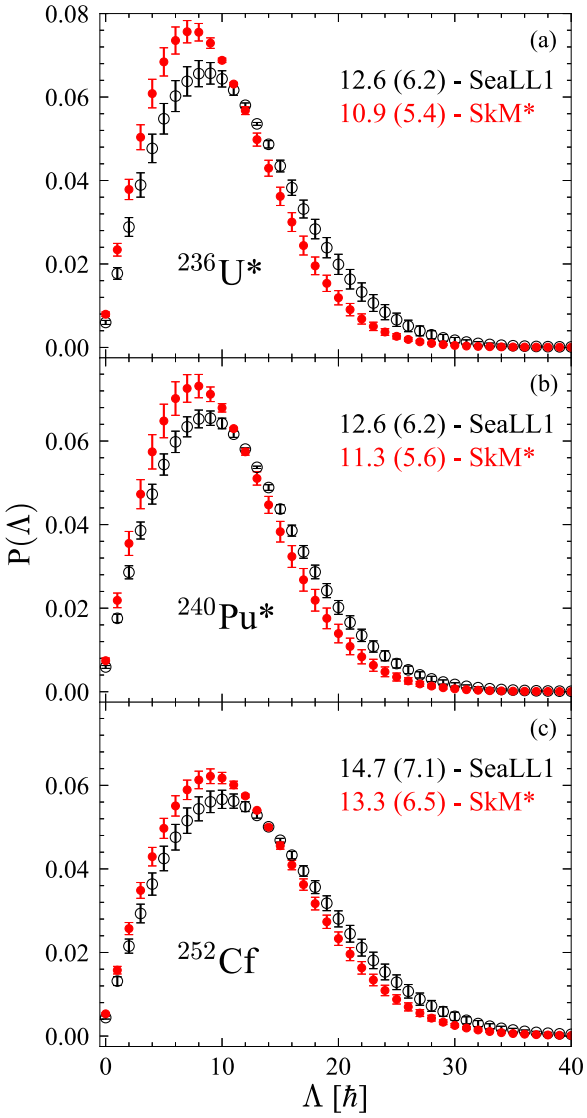

Figure 21: (Color online) The orbital angular momentum distributions for three nuclear systems ^{236}U, ^{240}Pu, and ^{252}Cf. For each nucleus the average orbital momentum and corresponding standard deviations are shown in the legend. The uncertainties are the standard deviations that characterize the range of the variations due to the spread of the initial values of the multipole moments and the energies of the fissioning nucleus.

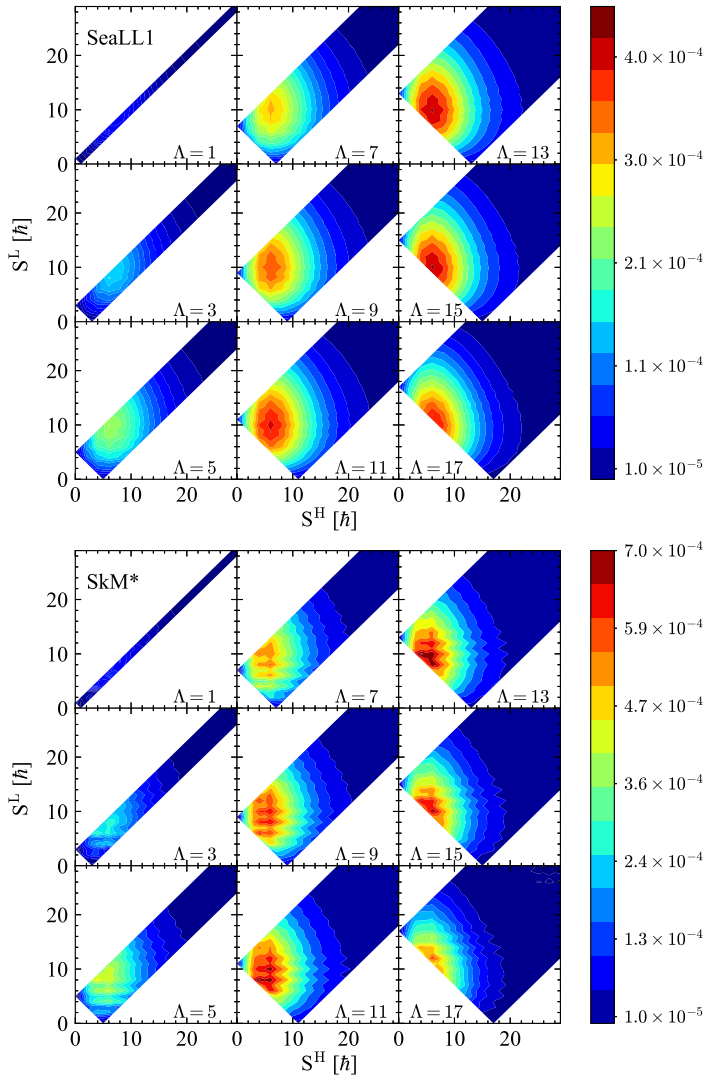

Figure 22: (Color online) The triple probability distribution for ^{252}Cf for SeaLL1 (upper panel) and SkM* (lower panel) NEDFs for odd values of Λ. Even values of Λ are similar.

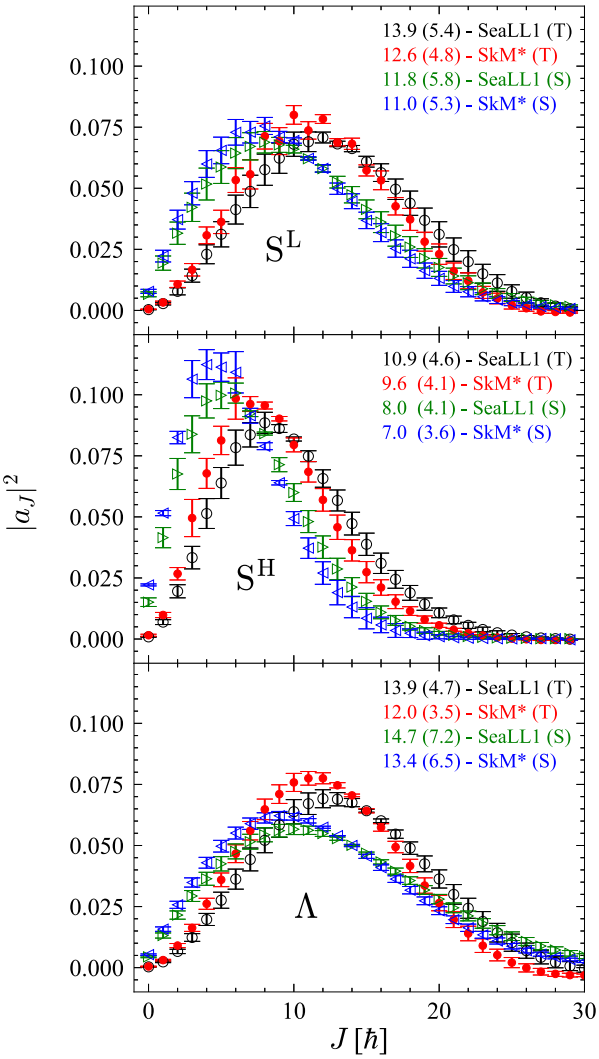

Figure 23: (Color online) The LFF and HFF intrinsic spins and orbital angular momenta distributions in the case of the spontaneous fission of ^{252}Cf using the triple projection distributions and equation 139 (denoted by T), and from the single projection of the FF intrinsic spins and orbital angular momenta defined by equations 126, 132 (denoted by S). The average and corresponding standard deviations are shown in the legend.

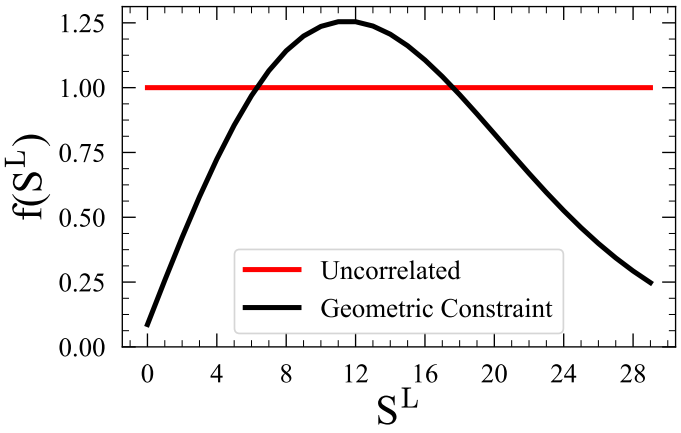

Figure 24: (Color online) From the triple distribution $P(S^L, S^H, \Lambda) = P_S(S_L)P_S(S_H)P_S(\Lambda)$, where S denotes AM distributions obtained from equation 126. The uncorrelated spin factor (red line) was obtained by summing $P(S^L, S^H, \Lambda)$ over S_H and Λ without applying the selection rules. The correlated spin factor (black line) was obtained by summing $P(S^L, S^H, \Lambda)$ over S_H, Λ with applying the selection rules (geometric constraints). The calculation was performed for the fission of ^{252}Cf on a 30x30x60 lattice with spacing a = 1 fm using the EDF SeaLL1.

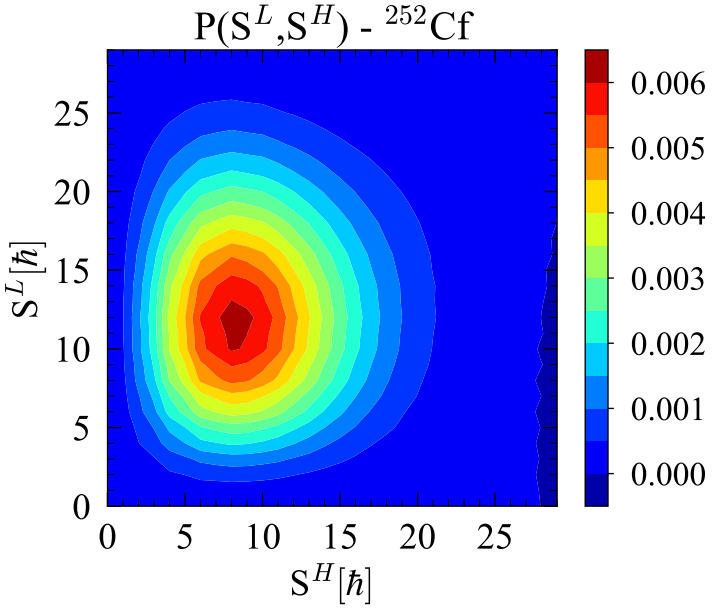

Figure 25: (Color online) The FF intrinsic spin magnitude probability distribution for the fission of ^{252}Cf on a 30x30x60 lattice with spacing a = 1 fm using the EDF SeaLL1.

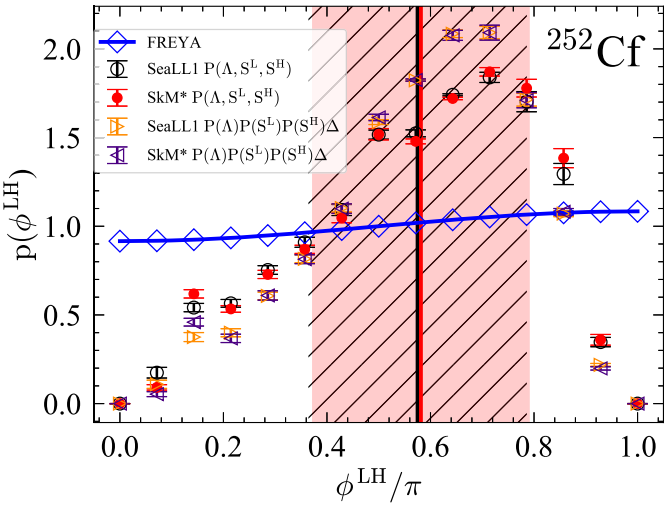

Figure 26: The circles and bullets represent the histogram (with a bin size of 0.22 rads) of the angle between the FF intrinsic S^L and S^H extracted using equation 146. The triangle represents the histogram obtained with $P(\Lambda)P(S^L)P(S^H)\Delta$, where Δ is defined in equation 140, and the distributions are described by equation 139. The blue line and diamonds are the prediction from FREYA [87].

4 Mathematical Properties of TDSLDA

4.1 Chaos in TDSLDA

The following section will summarize studies performed investigating chaos in TDDFT [32]. A system is defined as chaotic if small variations in the initial conditions lead to vastly different trajectories in phase space. This is characterized by the Lyapunov exponent of the system,

$$\lambda = \lim_{t\to\infty} \frac{1}{t} \frac{|\delta Z(t)|}{|\delta Z(0)|}, \tag{149}$$

where $\delta Z(t)$ represents the difference in time between two full sets of phase-space variables. If the Lyapunov exponent is positive, the two trajectories will diverge and the system is called chaotic; if it is zero the trajectories will be parallel, akin to circles of different radii in a 2-D phase space diagram; if it is negative the trajectories will be restorative converging to the same path after sufficient time has passed, true in the case of dissipative systems.

This leads to the primary focus of our investigation. Schrodinger's equation for an interacting many body system is linear and hence it's Lyapunov exponents are vanishing. TDDFT is functionally equivalent to Schrodinger's equation, however it is formulated as a set of highly nonlinear coupled partial differential equations. So for real implementations of TDDFT is the chaos? This issue has rarely been studied in literature, specifically for time-dependent phenomena, except for a few instances where the subject was touched upon briefly [37] [27] [65], and one case in more detail [4]. The more detailed study considered the narrower problem of the Lyapunov stability of TDHF and RPA only in cases when the initial state minimized either the micro canonical, canonical, or grand canonical partition functions. In [32], a much more general problem is addressed, namely when the initial state of the quantum system is an excited, or in one case highly excited, state. Three systems are investigated (two of which are realistic nuclear systems): vortices

in the unitary Fermi gas, the fission of ^{236}U, and collisions of ^{238}U+^{238}U. The later two will be emphasized, consistent with the overall theme of this thesis.

It has been demonstrated, by Maldacena et al [70] and Tsuji et al [106], that upper bound for the Lyapunov exponent of a quantum system is given by,

$$\lambda_{\mathrm{MSS}} \leq \frac{\pi T}{\hbar}. \tag{150}$$

For classical systems ($\hbar \to 0$) this implies no upper bound. Since the system of interest are quantum this limit is not considered. Additionally λ_{MSS} can only be defined after a long time, when the system has obtained thermal equilibrium [66], however for most real cases shorter timescales can be considered. For example, for fission, the time it takes for the nucleus splits into two well separated fragments, can (for all practical purposes) act as the "infinite" time limit.

To carry out these studies the initial quasi particle wave-functions were perturbed via,

$$\begin{bmatrix} u_{k\uparrow}(\vec{r},0) \\ u_{k\downarrow}(\vec{r},0) \\ v_{k\uparrow}(\vec{r},0) \\ v_{k\downarrow}(\vec{r},0) \end{bmatrix} \to \begin{bmatrix} u_{k\uparrow}(\vec{r},0)[1+\epsilon\alpha_{u\uparrow}(\vec{r})] \\ u_{k\downarrow}(\vec{r},0)[1+\epsilon\alpha_{u\downarrow}(\vec{r})] \\ v_{k\uparrow}(\vec{r},0)[1+\epsilon\alpha_{v\uparrow}(\vec{r})] \\ v_{k\downarrow}(\vec{r},0)[1+\epsilon\alpha_{v\downarrow}(\vec{r})] \end{bmatrix}, \tag{151}$$

where $\alpha_{(uv)(\uparrow\downarrow)}$ is a complex field with entries of the form, $Z = X + iY$, and where X, Y are random numbers between -1 and 1. The parameter ϵ represents the strength of the perturbation, and was evaluated at levels $\epsilon = 10^{-4}, 10^{-2}, 3\times10^{-2}$ for fission and for $\epsilon = 10^{-2}, 3\times10^{-2}$ for collisions. Alternatively, we could have perturbed the densities, since DFT states there exists a one to one mapping $\Psi \leftrightarrow n$. The choice of perturbation should not influence the final results.

For the case study of the fission of ^{236}U, the SeaLL1 EDF was used, and the simulation was performed on a $30^2 \times 60$ lattice with spacing a = 1 fm corresponding to $(4 \times 30^2 \times 60)^2 \approx 4.7 \times 10^{10}$ phase space elements.

The compound was evolved from the outer barrier past scission until the fragments were well separated, i.e. no longer exchanged energy, nucleons, or momenta, excluding the Coulomb interaction. The MSS upper bound was estimated via,

$$\lambda_{\mathrm{MSS}} = \frac{\pi T}{\hbar} \approx 0.016 \text{ c/fm}, \tag{152}$$

with a characteristic temperature $T = O(1)$ MeV for an excited nucleus. The Lyapunov exponent is defined as,

$$\lambda(t) = \frac{1}{2t} \frac{\int d^3r [n_\epsilon(\vec{r},t) - n_0(\vec{r},t)]^2}{\int d^3r [n_\epsilon(\vec{r},0) - n_0(\vec{r},0)]^2}, \tag{153}$$

where, $n_\epsilon(\vec{r},t), n_0(\vec{r},0)$ represent the perturbed, unperturbed number density respectively.

Figure 28 shows $\lambda(t)$, the maximum Lyapunov exponent, is well below the MSS bound. Interestingly, during the compound's descent from the neighborhood of the outer fission barrier, the evolution is over-damped, similar to a group of parachutists who all exit a plane at different times, but reach the same terminal velocity. This causes the Lyapunov exponent to be negative prior scission, meaning the process is restorative i.e. all trajectories descend towards the same mean path. For a more detailed (related) discussion see [38].

Another example involves the heavy-ion collision of ^{238}U + ^{238}U at a center-of-mass energy of 1200 MeV. The SeaLL1 EDF was used, and simulations were performed on a $30^2 \times 60$ fm^3 lattice with spacing $a = 1$ fm. After the collision, the two fragments emerge highly excited, with roughly 600 MeV of kinetic energy being converted into intrinsic energy. Using Bethe's formula, $T = \sqrt{\frac{10E^*}{A}}$, to estimate the temperature as $T = 3.55$ MeV, the corresponding MSS Lyapunov exponent is given by $\lambda_{\mathrm{MSS}} \approx 0.057$ c/fm. Figure 28 shows $\lambda(t)$, which saturates two orders of magnitude below the MSS upper bound. Similar to fission, after separation, the fragments only interact via Coulomb.

To conclude, two real nuclear systems were analyzed. We found the maximum Lyapunov exponent to be smaller by one order of magnitude for fission and two orders for heavy ion collisions relative to the MSS bound. This means, even though the exponents are non-vanishing, they are small enough not to alter the quality of the conclusions inferred within TDSLDA. That said, the fact that TDDFT is mathematically equivalent to Schrodinger's equation, but also contains a small positive Lyapunov exponent must be investigated. The most obvious source of error is the energy density functional. The exact TDDFT functional doesn't only depend on the instantaneous densities, but also all prior densities in time as well [90] [73]. This is absent from all current implementations of TDDFT. A second cause, which cannot be ruled at this time, could be an accumulation of numerical errors. The systems studied are computationally massive containing $O(10^{10})$ phase space elements, each of which evolve at least for 10,000 time-steps and up-to potentially 100,000 time-steps. Both sources must be considered to determine the quality of the TDDFT implementation.

4.2 Discussion on Entropy

Typically, for nuclear systems with pairing correlations, treated either in a shell model or mean field theory, practitioners are interested in the total binding energy, collective low lying levels, and other quantities, which can be evaluated accurately in calculations with low momentum cutoffs. However, certain observables cannot be reproduced with a low momentum cutoff such as the long tail of the nucleon momentum distribution, and observables which depend on it. This behavior has been studied extensively for decades in both cold atom and nuclear systems [94] [55] [54] [49] [93] [85] [97] [104] [101] [118] [24] [45] [92] [60] [2] [61] [86], and this section summarizes complementary investigations, focusing on the complexity of HFB wave-functions, with an emphasizes on a realistic ^{236}U fission case study. More details can be found in [40].

The complexity of many body wave-functions can be characterized by the quantum Boltzmann one-body entropy,

$$S = -\sum\!\!\!\!\!\!\int_k n_k \ln n_k - \sum\!\!\!\!\!\!\int_k [1-n_k]\ln[1-n_k], \tag{154}$$

and Shannon entropy,

$$\bar{S} = -\sum\!\!\!\!\!\!\int_k \tilde{n}_k \ln \tilde{n}_k. \tag{155}$$

Above, n_k refers to the canonical occupation probabilities, $\tilde{n}_k = \frac{n_k}{N}$, the integral implies a sum over discrete variables when appropriate, and

$$\sum\!\!\!\!\!\!\int_k n_k = N, \tag{156}$$

where N is the total particle number. The canonical occupation probabilities are defined as eigenvalues of the density matrix,

$$n(\xi,\gamma) = \langle\phi|\Psi^\dagger(\gamma)\Psi(\xi)|\phi\rangle \tag{157}$$

where $\Psi^\dagger(\gamma), \Psi(\xi)$ represent the creation, annihilation field operators. The Boltzmann entropy is an extensive quantity, while the Shannon entropy is a intensive quantity.

The canonical basis can be used to address (at least partially) the question: how many single (or quasi) particle states are required to accurately describe superfluid nuclei. First, the case of 1-D HFB was considered, which is used to describe spherical nuclear systems. In figure 29 the momentum distribution is given for different lattice constants. The distribution in all cases contains two knees, one at the Fermi level called the infrared (IR) knee, and one at high energies called the ultraviolet (UV) knee. At the IR knee the distribution has the expected BCS behavior. The region between the two knees decays as a power law. This behavior is due to the short range nature of nuclear forces, predicted by Sartor and Mahaux in 1980 [94], verified experimentally by O Hen in 2014 [60], and proven analytically to be a generic

feature for any system of many strongly interacting Fermions by Shina Tan in 2008 [104]. The region past the UV knee is unphysical, directly related to the cutoff momentum $p_{cutoff} = \frac{h\pi}{\Delta x}$, which in the limit $\Delta x \to 0$ goes to infinity.

The case of a realistic ^{236}U fission trajectory using TDSLDA was also considered. For pure Hartree-Fock, the Boltzmann entropy is minimized. For TDSLDA, inter-particle interactions cause the system to exists as a mixed state, leading to increasing entropy. For TDSLDA the many body wave-function is not an eigenstate of the total particle number operators, thus requiring a projection technique to restore the symmetry (see [28] for details). In figure 30, the Boltzmann entropy was shown as a function of time for both the particle projected and unprojected cases with only a minor difference in magnitude between both cases.

For fission, the entropy roughly doubles from the initial to final state, however, during intermediate time it exhibits non monotonic behavior. This highlights a key point: the complexity of an isolated many body wave-function does not always increase monotonically for finite time intervals. The erratic behavior can be understood. Start from the initial state, the compound nucleus at the outer barrier, and go up until the formation of the neck, which occurs at $\sim 400-500$ fm/c. In this time interval the entropy rapidly increases, as pairing allows for states to repopulate. The neck continues to form until roughly $\sim 700 - 800$ fm/c, during which the transfer of nucleons from one half of the compound to the other is inhibited, suppressing the spread of the single particle strength. From here the nucleus scissions, forming two fragments which evolve largely independently, except for the long range Coulomb interaction. The excited FFs thermalize, causing the single particle strength to spread, and the entropy to increase. In this sense, entropy provides a rich insight into the dynamics of fission.

A few key conclusions can be drawn from this study. Although the results were obtained strictly for the Bogoliubov-Valatin Canonical basis, they should hold for an arbitrary quantum many-body state $|\Phi\rangle$. This should

be the case, since in nuclear fission the fragments emerge highly excited, with an excitation energy beyond which pairing vanishes. This means the increase in entropy mostly arises from the significantly larger degree of complexity and entanglement in the final wave-function compared to the initial wave-function. This holds true even after particle projection. Second, a complete picture of nuclei should incorporate both mean field and short-range correlations, which are needed to produce he realistic long tail of the quantum momentum distribution. And last, we expect that the canonical bases, quantum Boltzmann and Shannon entropies, can be powerful tools for understanding the degree of complexity and entanglement for most quantum many body systems.

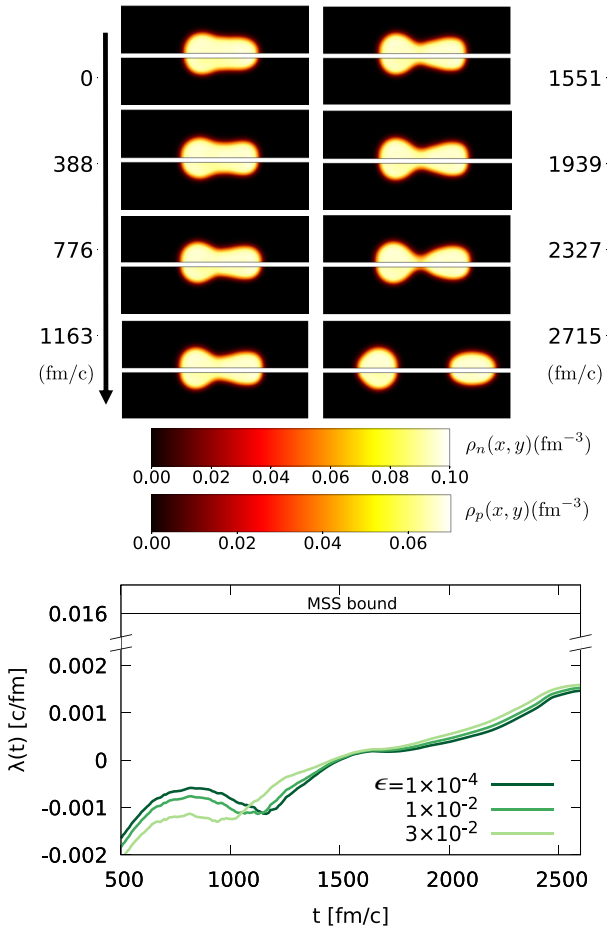

Figure 27: (Color online) The upper panel displays the evolution of the neutron number density (upper half of each frame) and proton number density (lower half of each frame) of a fissioning ^{236}U in a simulation box with dimensions $30^2 \times 60$ fm^3 into a heavy (left) and light (right) fragments. The neutron and proton numbers of the heavy (left) and light (right) fragments are (83.6, 52.2) and (60.4, 39.8) respectively. The shapes of the neutron and proton distributions are hardly affected by the noises level. The lower panel shows the time evolution of $\lambda(t)$. After scission, which occurs at $t \approx 2400$ fm/c, the excited fission fragments emerge. After thermalization they reach temperatures ~ 1 MeV [42], fixing the MSS upper bound as $\lambda_{\mathrm{MSS}}^{\mathrm{nuclear}} \approx 0.016$ c/fm.

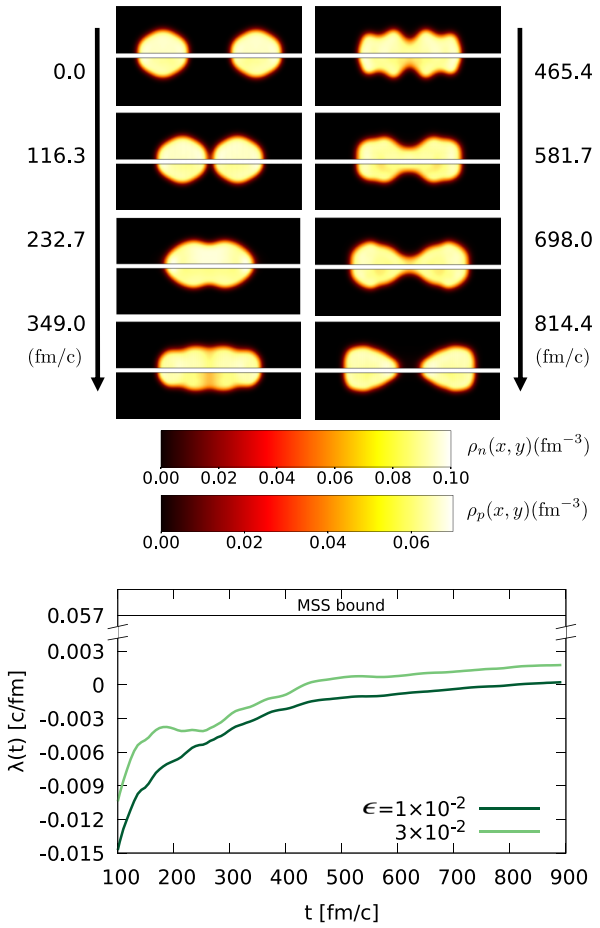

Figure 28: (Color online) The upper panel shows the evolution of the neutron number density (upper half of each frame) and proton number destiny (lower half of each frame) of the collision of ^{238}U + ^{238}U in a simulation box with dimensions $30^2 \times 64$ fm^3. After interacting the nuclei split two highly excited and not yet equilibrated fragments. The shapes of the neutron and proton distributions are hardly affected by the noises level. In the lower panel, the time evolution $\lambda(t)$, is shown at a center of mass energy of 1200 MeV. After separation the fragments emerge with temperatures T = 3.55 MeV, which results in a $\lambda_{\mathrm{MSS}}^{\mathrm{nuclear}} \approx 0.057$ c/fm.

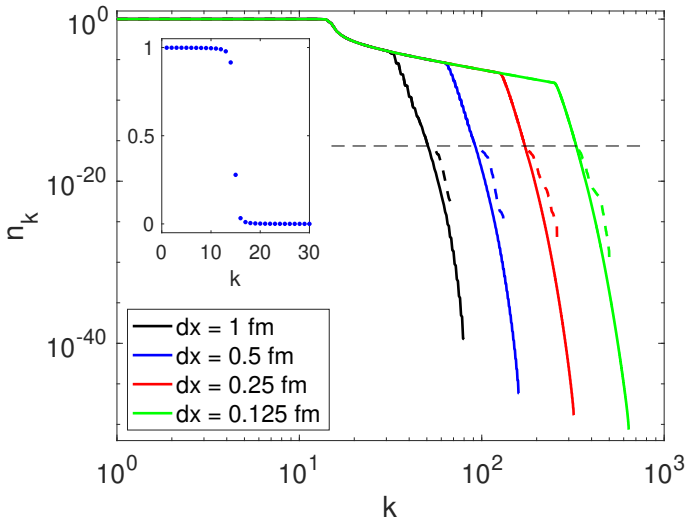

Figure 29: (Color online) The canonical occupation probabilities for four lattice constants dx in a log-log scale, corresponding to a momentum cutoff of $\Lambda = \pi/\mathrm{dx}$. The inset shows n_k in the linear scale close to the Fermi surface. Results obtained with increased machine precision 10^{-40} are shown with continuous solid lines, and those obtained with typical machine precision are shown with dashed lines.

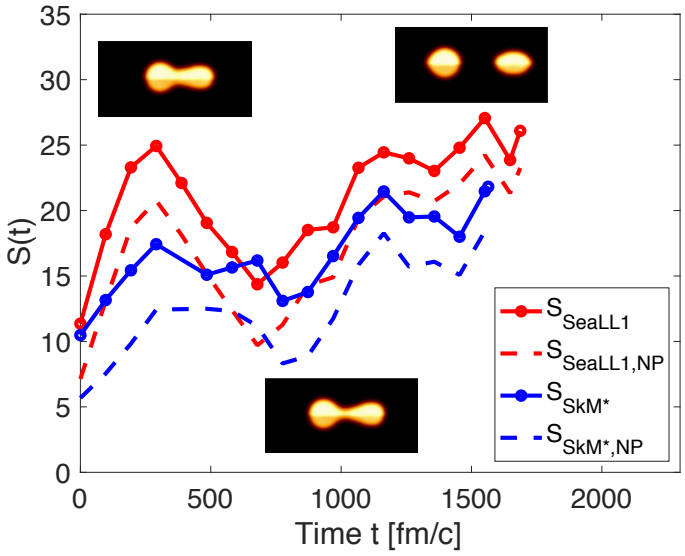

Figure 30: (Color online) The time-dependence of the entropy S evaluated in the case of induced fission of ^{235}U(n,f) with a low energy neutron, performed with two different nuclear energy density functionals SeaLL1 and SkM* as a function of time. The nuclei are evolved from the outer saddle point until the two fission fragments are fully separated. Even though there are small quantitative differences between the values of the entropies evaluated before and after a total particle projection was performed, the qualitative behavior of the quantum Boltzmann one -body entropy is by and large the same. The nuclear shapes in the case of SkM* are shown during at times 400, 1000, and 1500 fm/c.

5 Conclusion

5.1 Key Results

The following section summarizes key results pertaining to fission within TDSLDA. The underlying theory and numerical implementation of the LISE program, which is the first code to treat TDSLDA, is detailed in [65]. The program is self contained, providing everything needed to perform and analyze fission and heavy ion collision simulations from scratch: a static solver, time dependent program, and post processing script. Also part of the LISE program (although not yet publicly available) is the LISE projection code, which has been used to obtain FF spin distributions [31], [30]. In section 2.4 we applied TDSLDA to systematic fission studies of ^{236}U and ^{240}Pu, reiterating important points established by Bulgac et al in [38]: namely the adiabatic approximation isn't valid for fission, FF deformations relax after scission, and more.

We performed the first microscopic extraction of FF intrinsic spin distributions for ^{236}U and ^{240}Pu [31]. We showed the LFF carries more spin on average than the HFF pre neutron emission, contrary to what leading phenomenological models at the time assumed [57], [103]. We provided the first microscopic evidence for the existence of collective angular momenta modes bending and twisting. We highlighted the importance of performing time dependent fission simulations, since the FF deformations and hence the intrinsic spins, relax significantly after scission. And we investigated the FFs intrinsic spin distributions dependence on the compound's excitation energy, finding a weak dependence.

We investigated the role of the orbital angular momenta on the FF intrinsic spin distributions for ^{236}U, ^{240}Pu, and ^{252}Cf [30]. We performed the first microscopic extractions of the FF relative AM distributions, triple AM projection (for ^{252}Cf), and FF AM opening angle distribution (for ^{252}Cf). We found the opening angle distribution was completely anisotropic, imply-

ing strong correlations between the FF AM vectors, opposite to the isotropic distributions generated by FREYA [87].

Last of all, we investigated mathematical properties of TDSLDA. We tackled a crucial question: will TDSLDA, which is formulated through a set of highly nonlinear PDEs, but also functionally equivalent to the many body Schrodinger equation, which is linear and hence non-chaotic, exhibit chaos [32]? For realistic case studies using TDSLDA, for example the fission of ^{236}U, we found the answer to be no: the Lyapunov exponents in all cases were at least one order of magnitude below the MSS bound (defined in [70]), and not large enough to affect the system within the relevant timescale. In [40] we investigated the role of entropy (specifically one body entropy) in TDSLDA. The conclusion? In short, the situation is complicated. For the fission of ^{236}U, the entropy both increased and decreased, depending on the state of the system during the evolution. This suggests that the one-body entropy can be a useful tool to characterize the complexity and entanglement of quantum many body systems.

5.2 Future Outlook

This section will outline a few potential future direction for TDSLDA. First, particle number projection (pnp), which is required, since the many body wave-function exists in a super position of number eigenstates (for details see section 3.2). This topic has been studied for mean field theories since the 50s [82], with a renewed interest in recent times [5], [111]. One of the most persistent related issues is that microscopic theories tend to greatly underestimate the widths of the FF mass and charge distributions [96]. For heavy ion collisions, some progress has been made with the invention of the Balian Veneroni technique [3], however such a procedure is not applicable for asymmetric fission. TDSLDA can potentially help with this problem, since pairing is expected to widen the FFs masses and charge distributions [29]. Another major issue is that the FF mass and charge distributions are

uncorrelated for individual fission trajectories. A potential solution to both problems has been suggested by Aurel Bulgac: include proton neutron collision terms in TDSLDA [29] in the spirit of the Boltzmann-Uehling-Uhlenbeck (BUU) equation [81] [107].

This extension has been named gTDSLDA, and would introduce pn collision terms via pn pairing. The following will summarize arguments provided by Aurel Bulgac in [29] discussing the significance of such an extension. First, in heavy nuclei the number of np pairs is larger than the number of nn and pp pairs, and hence they could play an important role in fission. Second, pn pairing is expected to both widen and lead to correlated FF mass and charge distributions. To explain, in gTDSLDA the phases space increases significantly (a factor of two for any discrete representation), and during time evolution pairing will populate some of these additional states, which are statistically likely to exist away from the mean, and hence widen the distributions. Additionally the wave-function can longer be expressed as a product neutron and proton generalized slater determinants, meaning the neutron and proton number distributions become correlated. Formally the extension is given by:

$$i\hbar\frac{\partial}{\partial t}\begin{bmatrix} u_{nk\uparrow} \\ u_{nk\downarrow} \\ u_{pk\uparrow} \\ u_{pk\downarrow} \\ v_{nk\uparrow} \\ v_{nk\downarrow} \\ v_{pk\uparrow} \\ v_{pk\downarrow} \end{bmatrix} = \begin{bmatrix} h_{n\uparrow\uparrow} & h_{n\uparrow\downarrow} & 0 & 0 & 0 & \Delta_n & \Delta_1 & \Delta_0 \\ h_{n\downarrow\uparrow} & h_{n\downarrow\downarrow} & 0 & 0 & -\Delta_n & 0 & -\Delta_0 & \Delta_1 \\ 0 & 0 & h_{p\uparrow\uparrow} & h_{p\uparrow\downarrow} & -\Delta_1 & -\Delta_0 & 0 & \Delta_p \\ 0 & 0 & h_{p\downarrow\uparrow} & h_{p\downarrow\downarrow} & \Delta_0 & -\Delta_1 & -\Delta_p & 0 \\ 0 & -\Delta_n^* & \Delta_1^* & \Delta_0^* & -h_{n\uparrow\uparrow}^* & -h_{n\uparrow\downarrow}^* & 0 & 0 \\ \Delta_n^* & 0 & -\Delta_0^* & \Delta_0^* & -h_{n\downarrow\uparrow}^* & -h_{n\downarrow\downarrow}^* & 0 & 0 \\ \Delta_1^* & -\Delta_0^* & 0 & -\Delta_p^* & 0 & 0 & -h_{p\uparrow\uparrow}^* & -h_{p\uparrow\downarrow}^* \\ \Delta_0^* & \Delta_1^* & \Delta_p^* & 0 & 0 & 0 & -h_{p\downarrow\uparrow} & -h_{p\downarrow\downarrow}^* \end{bmatrix}\begin{bmatrix} u_{nk\uparrow} \\ u_{nk\downarrow} \\ u_{pk\uparrow} \\ u_{pk\downarrow} \\ v_{nk\uparrow} \\ v_{nk\downarrow} \\ v_{pk\uparrow} \\ v_{pk\downarrow} \end{bmatrix}, \tag{158}$$

with the singlet and triplet pairing fields defined via:

$$\Delta_0 = -g_0\kappa_0, \tag{159}$$

$$\Delta_1 = -g_1\kappa_1, \tag{160}$$

and the singlet and triplet anomalous densities defined via,

$$\kappa_0(\vec{r}) = \sum_k v^*_{kn\downarrow}(\vec{r})u_{kp\uparrow}(\vec{r}), \tag{161}$$

$$\kappa_1(\vec{r}) = \sum_k v^*_{kn\uparrow}(\vec{r})u_{kp\uparrow}(\vec{r}), \tag{162}$$

The extension to gTDSLDA is already ongoing.

An additional assortment of related projects are currently or plan to be worked on in upcoming years: such as the effects of the compound's excitation energy on FF properties (one result is already published [31]); the fission of odd-odd and odd-even nuclei, which comprise the majority of nuclear systems, making them paramount for understanding fission; investigating the existence (or prominence) of scission neutrons, which recent studies suggest may be more prevalent than previously expected [44]; the treatment of generalized angular momenta correlations [28],

$$P(S_L,\hat{n}_L,S_H,\hat{n}_H) = (S_L+1/2)(S_H+1/2)\int_0^\pi d\eta_L \sin\eta_L \int_0^\pi d\eta_H \sin\eta_H \tag{163}$$

$$P_{S_L}(\cos\eta_L)P_{S_H}(\cos\eta_H)\sqrt{\det\left[\delta_{lk} + \langle v_l|(e^{i\hat{J}^L_x\cdot\eta_L\hat{n}_L}-1)\Theta^L|v_k\rangle + \langle v_l|(e^{i\hat{J}^H_x\cdot\eta_H\hat{n}_H}-1)\Theta^H|v_k\rangle\right]};$$

and the evaluation of particle number projected FF excitation energy and TKE distributions, calculations yet to be found in literature (the formalism is detailed in [28])!

Acknowledgements

I am grateful to everyone who has helped me get to this point. All of my teachers and mentors in undergrad, in grad school, my classmates, my friends, and my family. Dr. Nicolas Schunck from LLNL for hosting and mentoring me a few summers ago, and his contributions to the fission studies performed by our group. Professor Gabriel Wlazlowski, from the University of Warsaw, for his contribution (and co authorship) of a recently published PRC. To all members of my exam committee: professors Alejandro Garcia, Sanjay Reddy, Gerald Miller, Ivana Bozic, Silas Beane, Alvaro Chavarria, and Aurel Bulgac. An extra thank you to members who are also in the reading committee: professors Alejandro Garcia, Silas Beane, and Aurel Bulgac. To CENTAUR for funding my research, and to it's various members for their inspiring research and insightful discussions. And further, to it's organizers for the incredible number of research opportunities: from a winter internship at LANL, to hosting yearly and bi yearly conferences, which helped facilitate important research connections and collaborations. A thank you to Katie Hennessey, the secretary of the nuclear theory group at the University of Washington, for numerous times she helped deal with administrative and logical issues. And a thank you to Matt Kafker in anticipation of a fruitful collaboration in the future.

This last section I reserved for individuals who helped me the most during my graduate career. First, Dr. Shi Jin, who constantly took time from his day to teach me when I first joined the group. Second, Kenny Roche of PNNL, who is an expect in computer science, and with whom I have had many insightful discussions related to the computational aspects of my work. Third, Dr. Kyle Godbey of FRIB. Our collaboration has been very fruitful: together we build the original version of the LISE projection package leading to two PRLs thus far, with more related projects planned in the future. Forth, Dr. Ionel Stetcu of LANL, my longest serving collaborator. He has played a

vital role in almost all of the projects I participated in, helped me in numerous occasions, and graciously hosted me for a winter internship at LANL. Fifth, and most importantly, Professor Aurel Bulgac. He introduced me to the wonderful world of nuclear physics, and got me involved in really interesting projects immediately, working on important and difficult problems such as fission, heavy ion collisions, and using the biggest super computers in the world to do so. He always pushed me to keep improving, and in this push I learned so much. Additionally he was always willing to offer up his time to teach me personally and has an inspiring level of physical insight. At this point in my career, he is the person I am most grateful for, alongside members of my family: my brother, my mom, and my dad for their constant love and support throughout the years. Thank you everyone!

Appendices

A Derivation of SLDA Static Equations from Variational Principle

This section covers explicitly the minimization described by equation 39 leading to the static SLDA equations described by equation 56. We will primarily make use of two formulas from the calculus of variations: the functional derivative and the chain rule. The variational derivative of a functional $\mathcal{E}[f(\vec{r}), \vec{\nabla} f(\vec{r}), \partial_{\alpha\beta} f(\vec{r})]$ is given by,

$$\frac{\partial \mathcal{E}[f(\vec{r})]}{\partial f(\vec{r})} = \frac{\partial \mathcal{E}}{\partial f} - \vec{\nabla} \cdot \frac{\partial \mathcal{E}}{\partial \vec{\nabla} f} + \partial_{\alpha\beta} \frac{\partial \mathcal{E}}{\partial_{\alpha\beta} f} + ... \tag{164}$$

where α, β represent spatial coordinates. If the functional $\mathcal{E}$ depends on densities $\rho[f(\vec{r}), \vec{\nabla} f(\vec{r}), \partial_{\alpha\beta} f(\vec{r})]$, which are functionals of f, the variational derivative of $\mathcal{E}$ can be expressed as,

$$\frac{\delta \mathcal{E}[\rho(\vec{r})]}{\delta f(\vec{r})} = \int d\vec{r}' \frac{\delta \rho(\vec{r}')}{\delta f(\vec{r})} \frac{\delta \mathcal{E}[\rho(\vec{r}')]}{\delta \rho(\vec{r}')}. \tag{165}$$

To minimize the EDF consider the derivative $\frac{\delta \mathcal{E}}{\delta v_{k\downarrow q}}$, which describes the last row of the static SLDA equations. The remaining rows can be obtained using the properties and symmetries of the quasi particle wave-functions. Since the computation of $\frac{\delta \mathcal{E}}{\delta v_{k\downarrow q}}$ is highly involved, the contribution from each density will be computed separately.

The number density contribution is straightforward:

$$\frac{\partial \mathcal{E}}{\partial v_{ksq}} = \frac{\partial \mathcal{E}}{\partial n_q} \frac{\partial n_q}{\partial v_{ksq}} = \frac{\partial \mathcal{E}}{\partial n_q} v^*_{ksq}, \tag{166}$$

with,

$$\frac{\partial \mathcal{E}}{\partial n_q} = 2C_0^n n_0 + 2\xi_q C_1^n n_1 + 2C_0^\tau \tau_0 + 2\xi_q C_1^\tau \tau_1 + 2C_0^{\Delta n}\nabla^2 n_0 + 2\xi_q C_1^{\Delta n}\nabla^2 n_1 \quad (167)$$

$$+C_0^{\nabla J}\vec{\nabla}\cdot\vec{J}_0 + \xi_q C_1^{\nabla J}\vec{\nabla}\cdot\vec{J}_1 + C_0^\gamma(\gamma+2)n_0^{\gamma+1} + 2\xi_q C_1^\gamma n_1 n_0^\gamma + \sum_{q'=p,n}\frac{\partial g_{q',\mathrm{eff}}(n)}{\partial n_q(\vec{r})}|\kappa_{q'}(\vec{r})|^2,$$

for Skyrme EDFs, and,

$$\frac{\partial \mathcal{E}}{\partial n_q} = \frac{5}{3}a_0 n_0^{2/3} + 2b_0 n_0 + \frac{7}{3}c_0 n_0^{4/3} - \frac{a_1 n_1^2}{3n_0^{4/3}} + \frac{c_1 n_1^2}{3n_0^{2/3}} - \frac{7a_2 n_1^4}{3n_0^{10/3}} - \frac{2b_2 n_1^4}{n_0^3} - \frac{5c_2 n_1^4}{3n_0^{8/3}} \quad (168)$$

$$+\xi_q\Big(\frac{2a_1 n_1}{n_0^{1/3}} + 2b_1 n_1 + 2c_1 n_1 n^{1/3} + \frac{4a_2 n_1^3}{n_0^{7/3}} + \frac{4b_2 n_1^3}{n_0^2} + \frac{4c_2 n_1^3}{n_0^{5/3}}\Big),$$

for SeaLL1 EDFs. This term has no spin dependence.

The kinetic density contribution is given by:

$$\frac{\partial \mathcal{E}}{\partial v_{ksq}} = -\vec{\nabla}\cdot\frac{\partial \mathcal{E}}{\partial \tau_q}\frac{\partial \tau_q}{\partial \vec{\nabla} v_{ksq}} = -\vec{\nabla}\cdot\frac{\partial \mathcal{E}}{\partial \tau_q}\vec{\nabla} v^*_{ksq}, \quad (169)$$

with,

$$\frac{\partial \mathcal{E}}{\partial \tau_q} = \frac{\hbar^2}{2m} + C_0^\tau n_0 + \xi_q C_1^\tau n_1. \quad (170)$$

This term also has no spin dependence.

The spin density contribution is given by:

$$\frac{\partial \mathcal{E}}{\partial v_{ksq}} = \frac{\partial \mathcal{E}}{\partial \vec{s}_q}\cdot\frac{\partial \vec{s}_q}{\partial v_{ksq}} = \frac{\partial \mathcal{E}}{\partial \vec{s}_q}\cdot\vec{\sigma}_{ss'}v^*_{ks'q}, \quad (171)$$

with,

$$\frac{\partial \mathcal{E}}{\partial \vec{s}_q} = C_0^{\nabla J} \vec{\nabla} \times \vec{j}_0 + \xi_q C_1^{\nabla J} \vec{\nabla} \times \vec{j}_1. \tag{172}$$

The anomalous density contribution is given by,

$$\frac{\delta \mathcal{E}}{\delta v_{k\downarrow q}} = \frac{\partial \mathcal{E}}{\partial \kappa_q^*} \frac{\partial \kappa_q^*}{\partial v_{k\downarrow q}} = \frac{\partial \mathcal{E}}{\partial \kappa_q^*} u^*_{k\uparrow q}, \tag{173}$$

with,

$$\frac{\partial \mathcal{E}}{\partial \kappa_q^*} = -\Delta. \tag{174}$$

The remaining spin term $\frac{\delta \mathcal{E}}{\delta v_{k\uparrow q}}$ will be considered later.

The contribution from the current density is significantly more complicated:

$$\begin{aligned} \frac{\delta \mathcal{E}}{\delta v_{ksq}} = \frac{\partial \mathcal{E}}{\partial \vec{j}_q} \cdot \frac{\partial \vec{j}_q}{\partial v_{ksq}} - \partial_\alpha \frac{\partial \mathcal{E}}{\partial \vec{j}} \cdot \frac{\partial \vec{j}}{\partial (\partial_\alpha v_{ksq})} \\ + \frac{\partial \mathcal{E}}{\partial (\partial_\alpha j_\beta)} \frac{\partial (\partial_\alpha j_\beta)}{\partial v_{ksq}} - \partial_\gamma \frac{\partial \mathcal{E}}{\partial (\partial_\alpha j_\beta)} \frac{\partial (\partial_\alpha j_\beta)}{\partial (\partial_\gamma v_{ksq})} \\ + \partial_{\gamma\omega} \frac{\partial \mathcal{E}}{\partial (\partial_\alpha j_\beta)} \frac{\partial (\partial_\alpha j_\beta)}{\partial (\partial_{\gamma\omega} v_{ksq})}, \end{aligned} \tag{175}$$

where $\alpha, \beta, \gamma, \omega$ refer to spatial indices. Term by term,

$$\frac{\partial \vec{j}}{\partial v_{ksq}} = -\frac{1}{2i} \vec{\nabla} v^*_{ksq}, \tag{176}$$

$$\frac{\partial j_\beta}{\partial (\partial_\alpha v_{ksq})} = \frac{1}{2i} \delta_{\alpha\beta} v^*_{ksq}, \tag{177}$$

$$\frac{\partial (\partial_\alpha j_\beta)}{\partial v_{ksq}} = -\frac{1}{2i} \partial_{\alpha\beta} v^*_{ksq}, \tag{178}$$

$$\frac{\partial(\partial_\alpha j_\beta)}{\partial(\partial_\gamma v_{ksq})} = \frac{1}{2i}\Big[\delta_{\beta\gamma}\partial_\alpha v^*_{ksq} - \delta_{\alpha\gamma}\partial_\beta v^*_{ksq}\Big], \tag{179}$$

$$\frac{\partial(\partial_\alpha j_\beta)}{\partial(\partial_{\gamma\omega} v_{ksq})} = \frac{1}{2i}\delta_{[\alpha\beta][\gamma\omega]} v^*_{ksq}, \tag{180}$$

where $\delta_{[\alpha\beta][\gamma\omega]}$ denotes the unordered set $[\alpha\beta]$ must be equal to the unordered set $[\gamma\omega]$. The derivatives of the EDF with respect to $\vec{j}$ and $\partial_\alpha j_\beta$ are given by:

$$\frac{\partial \mathcal{E}}{\partial \vec{j}_q} = -2\Big(C^\tau_0 \vec{j}_0 + \xi_q C^\tau_1 \vec{j}_1\Big), \tag{181}$$

$$\frac{\partial \mathcal{E}}{\partial(\partial_\alpha j_{q\beta})} = \frac{\partial}{\partial(\partial_\alpha j_{q\beta})} C^{\nabla J}_t \Big[s_x(\partial_y j_z - \partial_z j_y) \tag{182}$$

$$+ s_y(\partial_z j_x - \partial_x j_z) + s_z(\partial_x j_y - \partial_y j_x)\Big]$$

$$= \big(\hat{\alpha} \times \hat{\beta}\big) \cdot \big(C^{\nabla J}_0 \vec{s}_0 + \xi_q C^{\nabla J}_1 \vec{s}_1\big).$$

Combining terms,

$$\frac{\partial \mathcal{E}}{\partial \vec{j}_q} \cdot \frac{\partial \vec{j}_q}{\partial v_{ksq}} = -i\Big(C^\tau_0 \vec{j}_0 + \xi_q C^\tau_1 \vec{j}_1\Big) \cdot \vec{\nabla} v^*_{ksq}, \tag{183}$$

$$-\partial_\alpha \frac{\partial \mathcal{E}}{\partial \vec{j}} \cdot \frac{\partial \vec{j}}{\partial(\partial_\alpha v_{ksq})} = -i\Big[\vec{\nabla} \cdot \big(C^\tau_0 \vec{j}_0 + \xi_q C^\tau_1 \vec{j}_1\big)\Big] v^*_{ksq}, \tag{184}$$

$$\frac{\partial \mathcal{E}}{\partial(\partial_\alpha j_\beta)} \frac{\partial(\partial_\alpha j_\beta)}{\partial v_{ksq}} = \frac{i}{2}\big(\hat{\alpha} \times \hat{\beta}\big) \cdot \big(C^{\nabla J}_0 \vec{s}_0 + \xi_q C^{\nabla J}_1 \vec{s}_1\big) \partial_{\alpha\beta} v^*_{ksq}, \tag{185}$$

$$-\partial_\gamma \frac{\partial \mathcal{E}}{\partial(\partial_\alpha j_\beta)} \frac{\partial(\partial_\alpha j_\beta)}{\partial(\partial_\gamma v_{ksq})} = \frac{i}{2}\partial_\gamma\big(\hat{\alpha}\times\hat{\beta}\big)\cdot\big(C_0^{\nabla J}\vec{s}_0+\xi_q C_1^{\nabla J}\vec{s}_1\big)\Big[\delta_{\beta\gamma}\partial_\alpha v^*_{ksq}-\delta_{\alpha\gamma}\partial_\beta v^*_{ksq}\Big], \tag{186}$$

$$\partial_{\gamma\omega} \frac{\partial \mathcal{E}}{\partial(\partial_\alpha j_\beta)} \frac{\partial(\partial_\alpha j_\beta)}{\partial(\partial_{\gamma\omega} v_{ksq})} = -\frac{i}{2}\partial_{\gamma\omega}\big(\hat{\alpha}\times\hat{\beta}\big)\cdot\big(C_0^{\nabla J}\vec{s}_0+\xi_q C_1^{\nabla J}\vec{s}_1\big)\delta_{[\alpha\beta][\gamma\omega]} v^*_{ksq}. \tag{187}$$

Terms described by equations 185 and 187 vanish, since they are odd under the exchange of α and β, and the term described by equation 186 simplifies to:

$$\frac{\partial \mathcal{E}}{\partial(\partial_\alpha j_\beta)} \frac{\partial(\partial_\alpha j_\beta)}{\partial v_{ksq}} = -i\big(C_0^{\nabla J}\vec{\nabla}\times\vec{s}_0+\xi_q C_1^{\nabla J}\vec{\nabla}\times\vec{s}_1\big)\cdot\vec{\nabla}v^*_{ksq}, \tag{188}$$

which can be symmetrized:

$$\frac{\partial \mathcal{E}}{\partial(\partial_\alpha j_\beta)} \frac{\partial(\partial_\alpha j_\beta)}{\partial v_{ksq}} = -i\Big[\big(\frac{1}{2}C_0^{\nabla J}\vec{\nabla}\times\vec{s}_0+\frac{1}{2}\xi_q C_1^{\nabla J}\vec{\nabla}\times\vec{s}_1\big)\cdot\vec{\nabla}v^*_{ksq}, \tag{189}$$

$$+\vec{\nabla}\cdot\big(\frac{1}{2}C_0^{\nabla J}\vec{\nabla}\times\vec{s}_0+\frac{1}{2}\xi_q C_1^{\nabla J}\vec{\nabla}\times\vec{s}_1\big)v^*_{ksq}\Big]$$

Combining all results, the entire current density contribution is given by,

$$\frac{\delta \mathcal{E}}{\delta v_{ksq}} = -i\Big[\big(\frac{1}{2}C_0^{\nabla J}\vec{\nabla}\times\vec{s}_0+\frac{1}{2}\xi_q C_1^{\nabla J}\vec{\nabla}\times\vec{s}_1+C_0^{\tau}\vec{j}_0+\xi_q C_1^{\tau}\vec{j}_1\big)\cdot\vec{\nabla}v^*_{ksq} \tag{190}$$

$$+\vec{\nabla}\cdot\big(\frac{1}{2}C_0^{\nabla J}\vec{\nabla}\times\vec{s}_0+\frac{1}{2}\xi_q C_1^{\nabla J}\vec{\nabla}\times\vec{s}_1+C_0^{\tau}\vec{j}_0+\xi_q C_1^{\tau}\vec{j}_1\big)v^*_{ksq}\Big].$$

The contribution from the spin current density is given by:

$$\frac{\delta\mathcal{E}}{\delta v_{ksq}} = \frac{\partial\mathcal{E}}{\partial(\vec{\nabla}\cdot\vec{J}_q)}\frac{\partial(\vec{\nabla}\cdot\vec{J}_q)}{\partial v_{ksq}} - \vec{\nabla}\frac{\partial\mathcal{E}}{\partial(\partial_\alpha J_{q\alpha})}\frac{\partial(\partial_\alpha J_{q\alpha})}{\partial(\vec{\nabla}v_{ksq})} \tag{191}$$

$$+\partial_{\alpha\beta}\frac{\partial\mathcal{E}}{\partial(\vec{\nabla}\cdot\vec{J}_q)}\frac{\partial(\vec{\nabla}\cdot\vec{J}_q)}{\partial(\partial_{\alpha\beta}v_{ksq})}$$

This term is also complicated and will be handled part by part:

$$\vec{\nabla}\cdot\vec{J}_q = \frac{1}{2i}\sum_{kss'}\Big(\vec{\nabla}v^*_{ks'}\cdot[\vec{\nabla}v_{ks}\times\vec{\sigma}_{ss'}] - \vec{\nabla}v_{ks}\cdot[\vec{\nabla}v^*_{ks'}\times\vec{\sigma}_{ss'}] \tag{192}$$

$$+v^*_{ks'}\vec{\nabla}\cdot[\vec{\nabla}v_{ks}\times\vec{\sigma}_{ss'}] - v_{ks}\vec{\nabla}\cdot[\vec{\nabla}v^*_{ks'}\times\vec{\sigma}_{ss'}]\Big),$$

$$\frac{\partial(\vec{\nabla}\cdot\vec{J}_q)}{\partial v_{kqs}} = -\frac{1}{2i}\sum_{s'}\vec{\nabla}\cdot\big[\vec{\nabla}v^*_{ks'}\times\vec{\sigma}_{ss'}\big], \tag{193}$$

$$\frac{\partial\mathcal{E}}{\partial(\vec{\nabla}\cdot\vec{J}_q)} = C_0^{\nabla J}n_0 + \xi_q C_1^{\nabla J}n_1, \tag{194}$$

$$\frac{\partial(\partial_\alpha J_\alpha)}{\partial(\vec{\nabla}v_{kqs})} = \frac{1}{2i}\frac{\partial}{\partial(\vec{\nabla}v_{kqs})}\sum_{s'}\Big(\vec{\nabla}v^*_{ks'}\cdot[\vec{\nabla}v_{ks}\times\vec{\sigma}_{ss'}] - \vec{\nabla}v_{ks}\cdot[\vec{\nabla}v^*_{ks'}\times\vec{\sigma}_{ss'}]\Big) \tag{195}$$

$$= -\frac{1}{2i}\sum_{s'}[\vec{\nabla}v^*_{ks'}\times\vec{\sigma}_{ss'} + \vec{\nabla}v^*_{ks'}\times\vec{\sigma}_{ss'}]$$

$$= i\sum_{s'}[\vec{\nabla}v^*_{ks'}\times\vec{\sigma}_{ss'}].$$

The term $\frac{\partial(\vec{\nabla}\cdot\vec{J}_q)}{\partial(\partial_{\alpha\beta}v_{ks})}$ is zero for all combinations of α,β, since the two components of $\vec{\nabla}\cdot\vec{J}_q$, which contain second derivatives, each individually vanish (becomes self evident after minimal algebraic manipulation):

$$v^*_{ks'}\vec{\nabla}\cdot[\vec{\nabla}v_{ks}\times\vec{\sigma}_{ss'}] = 0, \tag{196}$$

$$v_{ks}\vec{\nabla}\cdot\left[\vec{\nabla}v^*_{ks'}\times\vec{\sigma}_{ss'}\right]=0. \tag{197}$$

Similarly the term described by equation 193 also vanishes.

Combining all non zero contributions from the spin current density we obtain:

$$\frac{\delta\mathcal{E}}{\delta v_{ksq}}=-\vec{\nabla}\frac{\partial\mathcal{E}}{\partial(\partial_\alpha J_{q\alpha})}\cdot\frac{\partial(\partial_\alpha J_{q\alpha})}{\partial(\vec{\nabla}v_{ksq})}=-i\sum_{s'}\vec{\nabla}\Big(C_0^{\nabla J}n_0+\xi_q C_1^{\nabla J}n_1\Big)\cdot\Big(\vec{\nabla}v^*_{ks'}\times\vec{\sigma}_{ss'}\Big) \tag{198}$$

With all densities accounted for, the last row of the static SLDA equations is given by:

$$\Delta(\vec{r})u^*_{k\uparrow}(\vec{r})-h_{\downarrow\uparrow}(\vec{r})v^*_{k\uparrow}(\vec{r})-(h_{\downarrow\downarrow}(\vec{r})-\mu)v^*_{k\downarrow}(\vec{r})=E_k v^*_{k\downarrow}(\vec{r}), \tag{199}$$

where $h_{ss'}$ is defined by equation 57. After complex conjugation:

$$\Delta^*(\vec{r})u_{k\uparrow}(\vec{r})-h^*_{\downarrow\uparrow}(\vec{r})v_{k\uparrow}(\vec{r})-(h^*_{\downarrow\downarrow}(\vec{r})-\mu)v_{k\downarrow}(\vec{r})=E_k v_{k\downarrow}(\vec{r}). \tag{200}$$

Since the HFB equations are time-reversal invariant, another solution to equation 200 given by:

$$i\sigma_y\begin{bmatrix}v_{k\uparrow}(\vec{r})\\v_{k\downarrow}(\vec{r})\end{bmatrix}=\begin{bmatrix}v_{k\downarrow}(\vec{r})\\-v_{k\uparrow}(\vec{r})\end{bmatrix}, \tag{201}$$

$$i\sigma_y\begin{bmatrix}u_{k\uparrow}(\vec{r})\\u_{k\downarrow}(\vec{r})\end{bmatrix}=\begin{bmatrix}u_{k\downarrow}(\vec{r})\\-u_{k\uparrow}(\vec{r})\end{bmatrix}, \tag{202}$$

leading to,

$$-\Delta^*(\vec{r})u_{k\downarrow}(\vec{r})-h^*_{\uparrow\downarrow}(\vec{r})v_{k\downarrow}(\vec{r})-(h^*_{\uparrow\uparrow}(\vec{r})-\mu)v_{k\uparrow}(\vec{r})=E_k v_{k\uparrow}(\vec{r}). \tag{203}$$

Applying the simultaneous transformation:

$$\begin{bmatrix} v_{k\uparrow}(\vec{r}) \leftrightarrow u^*_{k\uparrow}(\vec{r}) \\ v_{k\downarrow}(\vec{r}) \leftrightarrow u^*_{k\downarrow}(\vec{r}) \\ E_k \leftrightarrow -E_k \end{bmatrix}, \tag{204}$$

to equations 200, 203, we obtain:

$$\Delta^*(\vec{r})v^*_{k\uparrow}(\vec{r}) - h^*_{\downarrow\uparrow}(\vec{r})u^*_{k\uparrow}(\vec{r}) - (h^*_{\downarrow\downarrow}(\vec{r}) - \mu)u^*_{k\downarrow}(\vec{r}) = E_k u^*_{k\downarrow}(\vec{r}), \tag{205}$$

$$-\Delta^*(\vec{r})v^*_{k\downarrow}(\vec{r}) - h^*_{\uparrow\downarrow}(\vec{r})u^*_{k\downarrow}(\vec{r}) - (h^*_{\uparrow\uparrow}(\vec{r}) - \mu)u^*_{k\uparrow}(\vec{r}) = E_k u^*_{k\uparrow}(\vec{r}), \tag{206}$$

and after complex conjugation,

$$\Delta^*(\vec{r})v^*_{k\uparrow}(\vec{r}) - h^*_{\downarrow\uparrow}(\vec{r})u^*_{k\uparrow}(\vec{r}) - (h^*_{\downarrow\downarrow}(\vec{r}) - \mu)u^*_{k\downarrow}(\vec{r}) = E_k u^*_{k\downarrow}(\vec{r}), \tag{207}$$

$$-\Delta^*(\vec{r})v^*_{k\downarrow}(\vec{r}) - h^*_{\uparrow\downarrow}(\vec{r})u^*_{k\downarrow}(\vec{r}) - (h^*_{\uparrow\uparrow}(\vec{r}) - \mu)u^*_{k\uparrow}(\vec{r}) = E_k u^*_{k\uparrow}(\vec{r}). \tag{208}$$

Combining equations 200, 203, 207, and 208 we arrive at the SLDA static equations (equation 56).

B Discretization of LISE

Both the static and dynamic codes are implemented on a 3D cartesian lattice. In each direction of length $L = Na$, where N represents the number of lattice points along that direction and a represents the lattice spacing, the spatial coordinate x_n and Fourier component k_n are discretized via:

$$x_n = na, n = 0, ...N-1, \tag{209}$$

$$k_n = \begin{cases} 2n\pi/L, n = 0, ...N/2-1 \\ (2n-N)\pi/L, n = N/2, ...N-1 \end{cases}, \tag{210}$$

with periodic boundary conditions, i.e. all functions satisfy $F(x_0) = F(x_N)$.

When discretized on a 3D lattice, the wave functions and the Hamiltonian are represented in the discrete variable representation (DVR) [33], or Lagrange-mesh method [9], where functions (in 1D) are represented via:

$$\psi(x) = \sum_k a\psi(x_k) f_k(x), \tag{211}$$

with

$$f_k(x_l) = \sum_{n=-N/2}^{N/2-1} \frac{1}{L} \exp\left[ik_n(x_l - x_k)\right] \tag{212}$$

$$= \begin{cases} \frac{\sin[\pi(k-1)]}{Na} \cot\frac{\pi(k-l)}{N} & k \neq l, \\ 1/a \quad k = l, \end{cases}.$$

and with the DVR basis states forming a orthonormal set:

$$\langle f_k | f_l \rangle = \sum_n a f_k(x_n) f_l(x_n) = \delta_{kl}. \tag{213}$$

Static SLDA calculations require diagonalizing the HFB Hamiltonian. The local potential matrix elements (those which do not contain derivatives)

have a simple diagonal representation:

$$\langle f_k|U|f_l\rangle = \sum a f_k^*(x_n)U(x_n)f_l(x_n) = U(x_k)\delta_{kl}. \tag{214}$$

The non-local matrix elements, containing first ∂_x and second ∂_{xx} spatial derivatives in the kinetic and spin-orbit terms are represented as (see [33] for more details):

$$(\partial_x)_{nm} = \frac{\pi}{Na}(-1)^{n-m}(1-\delta_{nm})\cot\frac{\pi(n-m)}{N}, \tag{215}$$

$$(\partial_{xx})_{nm} = \frac{\pi^2}{2N^2a^2}\frac{(-1)^{(n-m)}(\delta_{nm}-1)}{\sin^2\frac{\pi(n-m)}{N}} - \frac{\pi^2}{3a^2}(1+\frac{2}{N^2})\delta_{nm}. \tag{216}$$

When applying the Hamiltonian on a wave-function, the most time consuming step is the calculation of the gradient and Laplacian. To make these operations efficient LISE uses fast Fourier transforms (FFTs):

$$\mathcal{F}[f(x)] : \tilde{f}(k_n) = \sum_{l=0}^{N-1} \exp(-ik_n x_l)f(x_l), \tag{217}$$

$$\mathcal{F}^{-1}[\tilde{f}(k)] : f(x_l) = \frac{1}{N}\sum_{n=0}^{N-1} \exp(ik_n x_l)f(x_n), \tag{218}$$

with $\mathcal{F}$ being the Fourier transform and $\mathcal{F}^{-1}$ being the inverse Fourier transform. To apply a derivative m times:

$$\mathcal{D}^{(m)}f(x) = \mathcal{F}^{-1}[(ik)^m\tilde{f}(k)]. \tag{219}$$

For odd powers of m a small and unphysical imaginary part is introduced. In order to eliminate this term we set $\tilde{f}(-k_N/2) = 0$ [105] [74] [25]. Note, an FFT approach for computing derivatives is often significantly faster and more accurate than any commonly used finite difference formula, requiring only $O(N \ln N)$ floating point operations.

For increasing numerical accuracy first derivatives are avoided whenever possible, for example products of two gradient functions are rewritten as,

$$\vec{\nabla}F(\vec{r})\cdot\vec{\nabla}G(\vec{r}) = \frac{1}{2}\Big(\Delta[F(\vec{r})G(\vec{r})] - \Delta[F(\vec{r})]G(\vec{r}) - F(\vec{r})\Delta[G(\vec{r})]\Big). \quad (220)$$

Additionally, terms which scale linearly with momentum are symmetrized,

$$\vec{A}(r,t)\cdot\vec{\nabla}\psi(\vec{r},t) = \frac{1}{2}\Big(\vec{A}(r,t)\cdot\vec{\nabla}\psi(\vec{r},t) + \vec{\nabla}\psi(\vec{r},t)\cdot\vec{A}(r,t)\Big). \quad (221)$$

and the Leibniz rule is used to evaluate derivatives of products of two functions via,

$$\vec{\nabla}[A(\vec{r})B(\vec{r})] = B(\vec{r})\vec{\nabla}A(\vec{r}) + A(\vec{r})\vec{\nabla}B(\vec{r}). \quad (222)$$

More choices are made when evaluating the kinetic term of the Hamiltonian;

$$-\vec{\nabla}\cdot\frac{\hbar^2}{2m^*(\vec{r})}\vec{\nabla}v_{k\sigma}(\vec{r}) = -\frac{1}{2}\Big(\frac{\hbar^2}{2m^*(\vec{r})}\Big)\nabla^2 v_{k\sigma}(\vec{r}) \quad (223)$$

$$+\frac{1}{2}\nabla^2\Big(\frac{\hbar^2}{2m^*(\vec{r})}v_{k\sigma}(\vec{r})\Big) - \frac{1}{2}\Big(\nabla^2\frac{\hbar^2}{2m^*(\vec{r})}\Big)v_{k\sigma}(\vec{r}),$$

and spin-orbit term;

$$-i\vec{W}(\vec{r})\cdot\big(\vec{\nabla}\times\vec{\sigma}\big)\psi(\vec{r}) = -\frac{i}{2}\Big[\vec{W}(\vec{r})\cdot\big(\vec{\nabla}\times\vec{\sigma}\big)\psi(\vec{r}) + \big(\vec{\sigma}\times\vec{W}(\vec{r})\big)\cdot\vec{\nabla}\psi(\vec{r})\Big], \quad (224)$$

for further increased numerical accuracy.

Perhaps the trickiest quality to evaluate numerically is the Coulomb potential, which must be treated carefully due to the existence of unphysical image charges introduced by the periodic boundary conditions, among other issues. Starting with Poisson's equation and it's solution,

$$\nabla^2\Phi(\vec{r}) = 4\pi e^2 n(\vec{r}), \quad (225)$$

$$\Phi(\vec{r}) = \int d^3r' \frac{e^2 n(\vec{r}')}{|\vec{r} - \vec{r}'|}, \tag{226}$$

which can be expressed in terms of FFTs via [46] [100],

$$\Phi(\vec{r}) = \int \frac{d^3k}{(2\pi)^3} \frac{4\pi e^2 \tilde{n}(\vec{k})}{k^2} \exp(i\vec{k} \cdot \vec{r}) = e^2 \mathcal{F}^{-1}[\tilde{n}(\vec{k}) \tilde{f}(\vec{k})], \tag{227}$$

with $\tilde{n}(\vec{k}) = \mathcal{F}[n(\vec{r})]$, the infrared divergence for $\vec{k} \to 0$ is avoided by using a truncated kernel $\tilde{f}(\vec{k})$ introduced in [46],

$$f(\vec{r}) = \begin{cases} 1/r, & \text{for } r < D \\ 0, & \text{otherwise} \end{cases} = \int \frac{d^3k}{(2\pi)^3} \tilde{f}(\vec{k}), \tag{228}$$

$$\tilde{f}(\vec{k}) = \begin{cases} 4\pi e^2 \big[1 - \cos(|\vec{k}|D)\big]/k^2 & |\vec{k}| \neq 0, \\ 2\pi e^2 D^2 & |\vec{k}| = 0, \end{cases} \tag{229}$$

where $D = \sqrt{3}L$ and L is the longest dimension of a box with lengths L_x, L_y, L_z. Then, the Coulomb potential is evaluated via,

$$\Phi(\vec{r}) = \frac{1}{27N^3} \sum_{\vec{k} \epsilon (3L)^3} e^2 \tilde{n}(\vec{k}) \tilde{f}(\vec{k}) \exp(i\vec{k} \cdot \vec{r}). \tag{230}$$

Due to the computation costs of performing such a large FFT, especially in simulations where one lattice dimension is significantly larger than the other two, the following method is used to reduce the large FFT into a sum of three smaller ones. First, note any function $f(x)$ defined on the interval $(0, L)$ can be expressed by a new function $g(x)$ defined on the interval $(-L, 2L)$ via,

$$g(x) = \begin{cases} f(x) & \text{if} \quad 0 \leq x \leq L, \\ 0 & \text{otherwise.} \end{cases} \tag{231}$$

On the interval $(0, L)$ the momentum components are given by:

$$k_i = -\frac{\pi}{a} + \frac{2\pi i}{L} \quad \text{for } i = 0, ...N-1, \tag{232}$$

and on the interval $(-L, 2L)$ by:

$$k_i = -\frac{\pi}{a} + \frac{2\pi i}{3L} \quad \text{for } i = 0, ...3N-1, \tag{233}$$

Then the Fourier transform of $f(x)$ can be written as a sum of the following three Fourier transforms,

$$h_n = \sum_l f(x_l)\exp(-ik_n x_l), \tag{234}$$

$$h_{n+1/3} = \sum_l f(x_l)\exp(-i\frac{2\pi}{3L}x_l)\exp(-ik_n x_l), \tag{235}$$

$$h_{n+2/3} = \sum_l f(x_l)\exp(-i\frac{4\pi}{3L}x_l)\exp(-ik_n x_l), \tag{236}$$

and consequently $g(x)$ can be expressed as,

$$g(x_l) = \frac{1}{3}\sum_n \exp(ik_n x_l)\Big[h_n + \exp(i\frac{2\pi}{3L}x_l)h_{n+1/3} + \exp(i\frac{4\pi}{3L}x_l)h_{n+2/3}\Big] \tag{237}$$

Each transformation h can be computed in parallel, and is three time smaller than computing the full FFT of g directly (in 1D). This is the big advantage of this trick. Using these transformations the Coulomb potential can be re-expressed as,

$$\Phi(\vec{r}) = \frac{1}{27N^3}\sum_{\alpha,\beta,\eta=0}^{2}\Big[\sum_{k\in L^3}\tilde{n}_{klm}(\vec{k},\alpha,\beta,\eta)\tilde{f}\big(\vec{k} + [\alpha\frac{2\pi}{3L}, \beta\frac{2\pi}{3L}, \eta\frac{2\pi}{3L}]\big)\exp(i\vec{k}\cdot\vec{r})\Big] \tag{238}$$
$$\exp\big(i[\alpha\frac{2\pi}{3L}x + \beta\frac{2\pi}{3L}y + \eta\frac{2\pi}{3L}z]\big),$$

with,

$$\tilde{n}_{klm}(\vec{k},\alpha,\beta,\eta) = \sum_{x,y,z\in L^3} n(x,y,z)\exp\Big(-i[\alpha\frac{2\pi}{3L}x+\beta\frac{2\pi}{3L}y+\eta\frac{2\pi}{3L}z]\Big)\exp(-i\vec{k}\cdot\vec{r}). \tag{239}$$

C Block Cyclic Decomposition

This section deals with the block cyclic decomposition (BCD) of the Hamiltonian matrix, needed for the diagonalization step of the static LISE solver. The HFB Hamiltonian matrix H is a $4\times N_{xyz}$ by $4\times N_{xyz}$ complex matrix with a degeneracy of 2 (protons and neutrons). To understand BCD, consider a more general matrix with m rows and n columns. Using column major indexing, meaning row indices $i \in [0, m-1]$ and column indices $j \in [0, n-1]$ can be related to the total matrix index k via,

$$k = i + j * m, \tag{240}$$

a matrix A, with $m = 9$, $n = 11$, can be expressed as,

$$A = \begin{bmatrix} a_{0,0} & a_{0,1} & a_{0,2} & a_{0,3} & a_{0,4} & a_{0,5} & a_{0,6} & a_{0,7} & a_{0,8} & a_{0,9} & a_{0,10} \\ a_{1,0} & a_{1,1} & a_{1,2} & a_{1,3} & a_{1,4} & a_{1,5} & a_{1,6} & a_{1,7} & a_{1,8} & a_{1,9} & a_{1,10} \\ a_{2,0} & a_{2,1} & a_{2,2} & a_{2,3} & a_{2,4} & a_{2,5} & a_{2,6} & a_{2,7} & a_{2,8} & a_{2,9} & a_{2,10} \\ a_{3,0} & a_{3,1} & a_{3,2} & a_{3,3} & a_{3,4} & a_{3,5} & a_{3,6} & a_{3,7} & a_{3,8} & a_{3,9} & a_{3,10} \\ a_{4,0} & a_{4,1} & a_{4,2} & a_{4,3} & a_{4,4} & a_{4,5} & a_{4,6} & a_{4,7} & a_{4,8} & a_{4,9} & a_{4,10} \\ a_{5,0} & a_{5,1} & a_{5,2} & a_{5,3} & a_{5,4} & a_{5,5} & a_{5,6} & a_{5,7} & a_{5,8} & a_{5,9} & a_{5,10} \\ a_{6,0} & a_{6,1} & a_{6,2} & a_{6,3} & a_{6,4} & a_{6,5} & a_{6,6} & a_{6,7} & a_{6,8} & a_{6,9} & a_{6,10} \\ a_{7,0} & a_{7,1} & a_{7,2} & a_{7,3} & a_{7,4} & a_{7,5} & a_{7,6} & a_{7,7} & a_{7,8} & a_{7,9} & a_{7,10} \\ a_{8,0} & a_{8,1} & a_{8,2} & a_{8,3} & a_{8,4} & a_{8,5} & a_{8,6} & a_{8,7} & a_{8,8} & a_{8,9} & a_{8,10} \end{bmatrix} \tag{241}$$

$$= \begin{bmatrix} a_0 & a_9 & a_{18} & a_{27} & a_{36} & a_{45} & a_{54} & a_{63} & a_{72} & a_{81} & a_{90} \\ a_1 & a_{10} & a_{19} & a_{28} & a_{37} & a_{46} & a_{55} & a_{64} & a_{73} & a_{82} & a_{91} \\ a_2 & a_{11} & a_{20} & a_{29} & a_{38} & a_{47} & a_{56} & a_{65} & a_{74} & a_{83} & a_{92} \\ a_3 & a_{12} & a_{21} & a_{30} & a_{39} & a_{48} & a_{57} & a_{66} & a_{75} & a_{84} & a_{93} \\ a_4 & a_{13} & a_{22} & a_{31} & a_{40} & a_{49} & a_{58} & a_{67} & a_{76} & a_{85} & a_{94} \\ a_5 & a_{14} & a_{23} & a_{32} & a_{41} & a_{50} & a_{59} & a_{68} & a_{77} & a_{86} & a_{95} \\ a_6 & a_{15} & a_{24} & a_{33} & a_{42} & a_{51} & a_{60} & a_{69} & a_{78} & a_{87} & a_{96} \\ a_7 & a_{16} & a_{25} & a_{34} & a_{43} & a_{52} & a_{61} & a_{70} & a_{79} & a_{88} & a_{97} \\ a_8 & a_{17} & a_{26} & a_{35} & a_{44} & a_{53} & a_{62} & a_{71} & a_{80} & a_{89} & a_{98} \end{bmatrix}$$

$$= \left[a_0, a_1, a_2, ...a_{97}, a_{98}\right].$$

For realistic fission calculations the HFB matrix will easily exceed the maximum memory of a single CPU. To overcome this issue, the memory is distributed across multiple CPUs, and with MPI (the message passing interface library) used to communicate between them. LISE has two distinct communicator spaces, one for protons and one for neutrons, and assigns np processors to each. For the test matrix A let's label the processor ids using iam = $0, ...\mathrm{np}-1$. Let np = p×q where p is the number of rows in the processor grid, and q is the number of columns. Then row processor ids can be assigned using ip = $0, ...\mathrm{p}-1$ and column processor ids using iq = $0, ...\mathrm{q}-1$. The row and column processor ids are related to the total processor id via,

$$\mathrm{iam} = \mathrm{ip} + \mathrm{iq} * \mathrm{p}, \tag{242}$$

with inverse relationships,

$$\mathrm{ip} = \mathrm{iam} \bmod \mathrm{p}, \tag{243}$$

$$\mathrm{iq} = \frac{\mathrm{iam} - (\mathrm{iam} \bmod \mathrm{p})}{\mathrm{p}}. \tag{244}$$

Label the portion of A assigned to processor $(\mathrm{ip}, \mathrm{iq})$ as $\mathrm{A}_{\mathrm{ip,iq}}$. It contains $\mathrm{m}_{\mathrm{ip}} \times \mathrm{n}_{\mathrm{iq}}$ complex coefficients. If $\mathrm{mb} \times \mathrm{nb}$ is the size of a block, then the total number of matrix elements each processor holds is given by,

$$\mathrm{m}_{\mathrm{ip}} = \frac{\mathrm{m}}{\mathrm{p} \cdot \mathrm{mb}}\,\mathrm{mb}, \tag{245}$$

$$\mathrm{n}_{\mathrm{iq}} = \frac{\mathrm{n}}{\mathrm{q} \cdot \mathrm{nb}}\,\mathrm{nb}, \tag{246}$$

where division above refers to integer division,

$$\mathrm{n/m} = \mathrm{floor(n/m)}. \tag{247}$$

Since the matrix A will rarely be evenly distributed across each processor an additional correction is needed to m_{ip} and n_{iq} based on the processor ids $(\mathrm{ip}, \mathrm{iq})$,

$$\text{if ip} < \frac{\mathrm{m\ mod(p\ mb)}}{\mathrm{mb}} \rightarrow \mathrm{m}_{\mathrm{ip}} = \mathrm{m}_{\mathrm{ip}} + \mathrm{mb}, \tag{248}$$

$$\text{if ip} = \frac{\mathrm{m\ mod(p\ mb)}}{\mathrm{mb}} \rightarrow \mathrm{m}_{\mathrm{ip}} = \mathrm{m}_{\mathrm{ip}} + \mathrm{m\ mod\ mb}, \tag{249}$$

$$\text{if iq} < \frac{\mathrm{n\ mod(q\ nb)}}{\mathrm{nb}} \rightarrow \mathrm{n}_{\mathrm{iq}} = \mathrm{n}_{\mathrm{iq}} + \mathrm{nb}, \tag{250}$$

$$\text{if iq} = \frac{\mathrm{n\ mod(q\ nb)}}{\mathrm{nb}} \rightarrow \mathrm{n}_{\mathrm{iq}} = \mathrm{n}_{\mathrm{iq}} + \mathrm{n\ mod\ nb}. \tag{251}$$

The local indices $(\mathrm{i}_{\mathrm{ip}}, \mathrm{j}_{\mathrm{iq}})$ (which describe the position of an element in a processor) can be now be related to the global indices (i, j) (which describe the position of an element in the global matrix A) via,

$$\mathrm{i}_{\mathrm{ip}} = \frac{\mathrm{i}}{\mathrm{p\ mb}}\mathrm{mb} + \mathrm{i\ mod\ mb}, \tag{252}$$

$$\mathrm{j_{iq}} = \frac{\mathrm{j}}{\mathrm{q\ nb}}\mathrm{nb} + \mathrm{j\ mod\ nb}. \tag{253}$$

The reverse map from $(\mathrm{i_{ip}}, \mathrm{j_{iq}})$ to (i, j) is given by,

$$\mathrm{i} = \mathrm{i_{ip}\ mod\ mb} + \frac{\mathrm{i_{ip}}}{\mathrm{mb}}\mathrm{p\ mb} + \mathrm{ip\ mb}, \tag{254}$$

$$\mathrm{j} = \mathrm{j_{iq}\ mod\ nb} + \frac{\mathrm{j_{iq}}}{\mathrm{nb}}\mathrm{q\ nb} + \mathrm{iq\ nb}. \tag{255}$$

The relationship between the local indices $(\mathrm{i_{ip}}, \mathrm{j_{iq}})$ and total local index $\mathrm{k_{ipq}}$ is given by,

$$\mathrm{k_{ipq}} = \mathrm{i_{ip}} + \mathrm{j_{iq}m_{ip}}. \tag{256}$$

Using the earlier example, let us explicitly lay out the mapping and reverse mapping for the case of $m = 9$, $n = 11$, $p = 2$, $q = 3$, $mb = 3$, $nb = 2$. The mapping from the global matrix A to the local matrices is given by,

$$\begin{bmatrix} \begin{bmatrix} a_{0,0} & a_{0,1} & a_{0,6} & a_{0,7} \\ a_{1,0} & a_{1,1} & a_{1,6} & a_{1,7} \\ a_{2,0} & a_{2,1} & a_{2,6} & a_{2,7} \\ a_{6,0} & a_{6,1} & a_{6,6} & a_{6,7} \\ a_{7,0} & a_{7,1} & a_{7,6} & a_{7,7} \\ a_{8,0} & a_{8,1} & a_{8,6} & a_{8,7} \end{bmatrix}_{(0,0)} & \begin{bmatrix} a_{0,2} & a_{0,3} & a_{0,8} & a_{0,9} \\ a_{1,2} & a_{1,3} & a_{1,8} & a_{1,9} \\ a_{2,2} & a_{2,3} & a_{2,8} & a_{2,9} \\ a_{6,2} & a_{6,3} & a_{6,8} & a_{6,9} \\ a_{7,2} & a_{7,3} & a_{7,8} & a_{7,9} \\ a_{8,2} & a_{8,3} & a_{8,8} & a_{8,9} \end{bmatrix}_{(0,1)} & \begin{bmatrix} a_{0,4} & a_{0,5} & a_{0,10} \\ a_{1,4} & a_{1,5} & a_{1,10} \\ a_{2,4} & a_{2,5} & a_{2,10} \\ a_{6,4} & a_{6,5} & a_{6,10} \\ a_{7,4} & a_{7,5} & a_{7,10} \\ a_{8,4} & a_{8,5} & a_{8,10} \end{bmatrix}_{(0,2)} \\ \begin{bmatrix} a_{3,0} & a_{3,1} & a_{3,6} & a_{3,7} \\ a_{4,0} & a_{4,1} & a_{4,6} & a_{4,7} \\ a_{5,0} & a_{5,1} & a_{5,6} & a_{5,7} \end{bmatrix}_{(1,0)} & \begin{bmatrix} a_{3,2} & a_{3,3} & a_{3,8} & a_{3,9} \\ a_{4,2} & a_{4,3} & a_{4,8} & a_{4,9} \\ a_{5,2} & a_{5,3} & a_{5,8} & a_{5,9} \end{bmatrix}_{(1,1)} & \begin{bmatrix} a_{3,4} & a_{3,5} & a_{3,10} \\ a_{4,4} & a_{4,5} & a_{4,10} \\ a_{5,4} & a_{5,5} & a_{5,10} \end{bmatrix}_{(1,2)} \end{bmatrix} \tag{257}$$

where the inner matrix subscript $(\mathrm{ip}, \mathrm{iq})$ identifies the host processor. The reverse mapping from processor ip = 0, iq = 0 is given by,

$$\begin{bmatrix} a_{0,0} & a_{0,1} & a_{0,6} & a_{0,7} \\ a_{1,0} & a_{1,1} & a_{1,6} & a_{1,7} \\ a_{2,0} & a_{2,1} & a_{2,6} & a_{2,7} \\ a_{6,0} & a_{6,1} & a_{6,6} & a_{6,7} \\ a_{7,0} & a_{7,1} & a_{7,6} & a_{7,7} \\ a_{8,0} & a_{8,1} & a_{8,6} & a_{8,7} \end{bmatrix}_{(0,0)} \rightarrow \begin{bmatrix} a_{0,0} & a_{0,1} & * & * & * & * & a_{0,6} & a_{0,7} & * & * & * \\ a_{1,0} & a_{1,1} & * & * & * & * & a_{1,6} & a_{1,7} & * & * & * \\ a_{2,0} & a_{2,1} & * & * & * & * & a_{2,6} & a_{2,7} & * & * & * \\ & & * & * & * & * & * & * & * & * & * & * & \\ & & * & * & * & * & * & * & * & * & * & * & \\ & & * & * & * & * & * & * & * & * & * & * & \\ a_{6,0} & a_{6,1} & * & * & * & * & a_{6,6} & a_{6,7} & * & * & * \\ a_{7,0} & a_{7,1} & * & * & * & * & a_{7,6} & a_{7,7} & * & * & * \\ a_{8,0} & a_{8,1} & * & * & * & * & a_{8,6} & a_{8,7} & * & * & * \end{bmatrix}. \quad (258)$$

References

[1] Summit user guide. `https://docs.olcf.ornl.gov/systems/summit_user_guide.html`.

[2] ER Anderson and Joaquin Emiliano Drut. Pressure, compressibility, and contact of the two-dimensional attractive fermi gas. *Physical Review Letters*, 115(11):115301, 2015.

[3] Roger Balian and Marcel Vénéroni. Time-dependent variational principle for predicting the expectation value of an observable. *Physical Review Letters*, 47(19):1353, 1981.

[4] Roger Balian and Marcel Vénéroni. Lyapunov stability and poisson structure of the thermal tdhf and rpa equations. *Annals of Physics*, 195(2):324–355, 1989.

[5] Benjamin Bally and Michael Bender. Projection on particle number and angular momentum: Example of triaxial bogoliubov quasiparticle states. *Physical Review C*, 103(2):024315, 2021.

[6] J. Bardeen, L. N. Cooper, and J. R. Schrieffer. Theory of superconductivity. *Phys. Rev.*, 108:1175–1204, Dec 1957.

[7] J Bartel, Ph Quentin, Matthias Brack, C Guet, and H-B Håkansson. Towards a better parametrization of skyrme-like effective forces: A critical study of the skm force. *Nuclear Physics A*, 386(1):79–100, 1982.

[8] Jean-Louis Basdevant and James Rich. *Fundamentals in nuclear physics: From nuclear structure to cosmology*. Springer Science & Business Media, 2005.

[9] Daniel Baye. The lagrange-mesh method. *Physics reports*, 565:1–107, 2015.

[10] ST Belyaev. *Effect of pairing correlations on nuclear properties*. E. Munksgaard Kobenhavn, 1959.

[11] Michael Bender, Paul-Henri Heenen, and Paul-Gerhard Reinhard. Self-consistent mean-field models for nuclear structure. *Rev. Mod. Phys.*, 75:121–180, Jan 2003.

[12] G Bertsch. The nuclear density of states in the space of nuclear shapes. *Physics Letters B*, 95(2):157–159, 1980.

[13] G. F. Bertsch, T. Kawano, and L. M. Robledo. Angular momentum of fission fragments. *Phys. Rev. C*, 99:034603, Mar 2019.

[14] George F Bertsch, CA Bertulani, Witold Nazarewicz, N Schunck, and Mario V Stoitsov. Odd-even mass differences from self-consistent mean field theory. *Physical Review C*, 79(3):034306, 2009.

[15] H. A. Bethe. Nuclear physics b. nuclear dynamics, theoretical. *Rev. Mod. Phys.*, 9:69–244, Apr 1937.

[16] K. Binder. Finite size effects on phase transitions. *Ferroelectrics*, 73(1):43–67, 1987.

[17] L. S Blackford. The two-dimensional block-cyclic distribution. `https://netlib.org/scalapack/slug/node75.html`, 1997.

[18] L. S. Blackford, J. Choi, A. Cleary, E. D'Azevedo, J. Demmel, I. Dhillon, J. Dongarra, S. Hammarling, G. Henry, A. Petitet, K. Stanley, D. Walker, and R. C. Whaley. *ScaLAPACK Users' Guide*. Society for Industrial and Applied Mathematics, Philadelphia, PA, 1997.

[19] NN Bogoljubov, Vladimir Veniaminovic Tolmachov, and DV Širkov. A new method in the theory of superconductivity. *Fortschritte der physik*, 6(11-12):605–682, 1958.

[20] A. Bohr, B. R. Mottelson, and D. Pines. Possible analogy between the excitation spectra of nuclei and those of the superconducting metallic state. *Phys. Rev.*, 110:936–938, May 1958.

[21] Niels Bohr and John Archibald Wheeler. The mechanism of nuclear fission. *Phys. Rev.*, 56:426–450, Sep 1939.

[22] L Bonneau, P Quentin, and IN Mikhailov. Scission configurations and their implication in fission-fragment angular momenta. *Physical Review C*, 75(6):064313, 2007.

[23] PJ Borycki, J Dobaczewski, W Nazarewicz, and MV Stoitsov. Pairing renormalization and regularization within the local density approximation. *Physical Review C*, 73(4):044319, 2006.

[24] Eric Braaten. Universal relations for fermions with large scattering length. In *The BCS-BEC Crossover and the Unitary Fermi Gas*, pages 193–231. Springer, 2012.

[25] Aurel Bulgac. Time-dependent density functional theory and the real-time dynamics of fermi superfluids. *Annual Review of Nuclear and Particle Science*, 63:97–121, 2013.

[26] Aurel Bulgac. Projection of good quantum numbers for reaction fragments. *Physical Review C*, 100(3):034612, 2019.

[27] Aurel Bulgac. Time-dependent density functional theory for fermionic superfluids: From cold atomic gases- to nuclei and neutron stars crust. *physica status solidi (b)*, 256(7):1800592, 2019.

[28] Aurel Bulgac. Restoring broken symmetries for nuclei and reaction fragments. *Physical Review C*, 104(5):054601, 2021.

[29] Aurel Bulgac. Pure quantum extension of the semiclassical boltzmann-uehling-uhlenbeck equation. *Physical Review C*, 105(2):L021601, 2022.

[30] Aurel Bulgac, Ibrahim Abdurrahman, Kyle Godbey, and Ionel Stetcu. Fragment intrinsic spins and fragments' relative orbital angular momentum in nuclear fission. *Physical Review Letters*, 128(2):022501, 2022.

[31] Aurel Bulgac, Ibrahim Abdurrahman, Shi Jin, Kyle Godbey, Nicolas Schunck, and Ionel Stetcu. Fission fragment intrinsic spins and their correlations. *Phys. Rev. Lett.*, 126:142502, Apr 2021.

[32] Aurel Bulgac, Ibrahim Abdurrahman, and Gabriel Wlazłowski. Sensitivity of time-dependent density functional theory to initial conditions. *Phys. Rev. C*, 105:044601, Apr 2022.

[33] Aurel Bulgac and Michael McNeil Forbes. Use of the discrete variable representation basis in nuclear physics. *Physical Review C*, 87(5):051301, 2013.

[34] Aurel Bulgac, Michael McNeil Forbes, Shi Jin, Rodrigo Navarro Perez, and Nicolas Schunck. Minimal nuclear energy density functional. *Phys. Rev. C*, 97:044313, Apr 2018.

[35] Aurel Bulgac, Michael McNeil Forbes, Michelle M Kelley, Kenneth J Roche, and Gabriel Wlazłowski. Quantized superfluid vortex rings in the unitary fermi gas. *Physical review letters*, 112(2):025301, 2014.

[36] Aurel Bulgac, Michael McNeil Forbes, and Piotr Magierski. The unitary fermi gas: From monte carlo to density functionals. In *The BCS-BEC Crossover and the Unitary Fermi Gas*, pages 305–373. Springer, 2012.

[37] Aurel Bulgac, Michael McNeil Forbes, and Gabriel Wlazłowski. Towards quantum turbulence in cold atomic fermionic superfluids. *Journal of Physics B: Atomic, Molecular and Optical Physics*, 50(1):014001, 2016.

[38] Aurel Bulgac, Shi Jin, Kenneth J. Roche, Nicolas Schunck, and Ionel Stetcu. Fission dynamics of ^{240}Pu from saddle to scission and beyond. *Phys. Rev. C*, 100:034615, Sep 2019.

[39] Aurel Bulgac, Shi Jin, and Ionel Stetcu. Unitary evolution with fluctuations and dissipation. *Physical Review C*, 100(1):014615, 2019.

[40] Aurel Bulgac, Matthew Kafker, and Ibrahim Abdurrahman. Measures of complexity and entanglement in fermionic many-body systems, 2022.

[41] Aurel Bulgac, Yuan-Lung Luo, and Kenneth J Roche. Quantum shock waves and domain walls in the real-time dynamics of a superfluid unitary fermi gas. *Physical Review Letters*, 108(15):150401, 2012.

[42] Aurel Bulgac, Piotr Magierski, Kenneth J. Roche, and Ionel Stetcu. Induced fission of ^{240}Pu within a real-time microscopic framework. *Phys. Rev. Lett.*, 116:122504, Mar 2016.

[43] Aurel Bulgac and Yongle Yu. Renormalization of the hartree-fock-bogoliubov equations in the case of a zero range pairing interaction. *Phys. Rev. Lett.*, 88:042504, Jan 2002.

[44] N Carjan and M Rizea. Similarities between calculated scission-neutron properties and experimental data on prompt fission neutrons. *Physics Letters B*, 747:178–181, 2015.

[45] Yvan Castin and Félix Werner. The unitary gas and its symmetry properties. In *The BCS-BEC crossover and the unitary Fermi gas*, pages 127–191. Springer, 2012.

[46] Alberto Castro, Angel Rubio, and MJ Stott. Solution of poisson's equation for finite systems using plane-wave methods. *Canadian Journal of Physics*, 81(10):1151–1164, 2003.

[47] J Dechargé and D Gogny. Hartree-fock-bogolyubov calculations with the d 1 effective interaction on spherical nuclei. *Physical Review C*, 21(4):1568, 1980.

[48] J. Dechargé and D. Gogny. Hartree-fock-bogolyubov calculations with the $d1$ effective interaction on spherical nuclei. *Phys. Rev. C*, 21:1568–1593, Apr 1980.

[49] C Ciofi Degli Atti and S Simula. Realistic model of the nucleon spectral function in few-and many-nucleon systems. *Physical Review C*, 53(4):1689, 1996.

[50] J Dobaczewski, W Nazarewicz, and MV Stoitsov. Nuclear ground-state properties from mean-field calculations. In *Exotic Nuclei and Atomic Masses*, pages 55–60. Springer, 2003.

[51] Thomas Døssing and Jørgen Randrup. Dynamical evolution of angular momentum in damped nuclear reactions:(i). accumulation of angular momentum by nucleon transfer. *Nuclear Physics A*, 433(2):215–279, 1985.

[52] M Dutra, O Lourenço, JS Sá Martins, A Delfino, J Rikovska Stone, and PD Stevenson. Skyrme interaction and nuclear matter constraints. *Physical Review C*, 85(3):035201, 2012.

[53] Till von Egidy and Dorel Bucurescu. Systematics of nuclear level density parameters. *Phys. Rev. C*, 72:044311, Oct 2005.

[54] Leonid Frankfurt and Mark Strikman. Hard nuclear processes and microscopic nuclear structure. *Physics Reports*, 160(5-6):235–427, 1988.

[55] Leonid L'vovič Frankfurt and Mark I Strikman. High-energy phenomena, short-range nuclear structure and qcd. *Physics Reports*, 76(4):215–347, 1981.

[56] Friedrich Gönnenwein. Neutron and gamma emission in fission, 2014.

[57] C Hagmann, J Randrup, and R Vogt. Freya—a new monte carlo code for improved modeling of fission chains. *IEEE Transactions on Nuclear Science*, 60(2):545–549, 2013.

[58] Richard Hamming. *Numerical methods for scientists and engineers*. Courier Corporation, 2012.

[59] Walter Hauser and Herman Feshbach. The inelastic scattering of neutrons. *Physical review*, 87(2):366, 1952.

[60] O Hen, M Sargsian, LB Weinstein, E Piasetzky, H Hakobyan, DW Higinbotham, M Braverman, WK Brooks, S Gilad, KP Adhikari, et al. Momentum sharing in imbalanced fermi systems. *Science*, 346(6209):614–617, 2014.

[61] Or Hen, Gerald A Miller, Eli Piasetzky, and Lawrence B Weinstein. Nucleon-nucleon correlations, short-lived excitations, and the quarks within. *Reviews of Modern Physics*, 89(4):045002, 2017.

[62] David Lawrence Hill and John Archibald Wheeler. Nuclear constitution and the interpretation of fission phenomena. *Phys. Rev.*, 89:1102–1145, Mar 1953.

[63] John R Huizenga. Nuclear fission revisited: Nuclear shells introduce structure into the fission barrier and lead to a number of interesting phenomena. *Science*, 168(3938):1405–1413, 1970.

[64] JR Huizenga and Rt Vandenbosch. Interpretation of isomeric cross-section ratios for (n, γ) and (γ, n) reactions. *Physical Review*, 120(4):1305, 1960.

[65] Shi Jin, Kenneth J Roche, Ionel Stetcu, Ibrahim Abdurrahman, and Aurel Bulgac. The lise package: solvers for static and time-dependent

superfluid local density approximation equations in three dimensions. *Computer Physics Communications*, 269:108130, 2021.

[66] L. D. Landau and E. M. Lifshitz. *Statistical Physics, Part 1*, volume 5 of *Course of Theoretical Physics*. Butterworth-Heinemann, Oxford, 1980.

[67] LD Landau. On the theory of the fermi liquid. *Sov. Phys. JETP*, 8(1):70, 1959.

[68] S. Levit, J. W. Negele, and Z. Paltiel. Barrier penetration and spontaneous fission in the time-dependent mean-field approximation. *Phys. Rev. C*, 22:1979–1995, Nov 1980.

[69] DG Madland. Total prompt energy release in the neutron-induced fission of 235u, 238u, and 239pu. *Nuclear Physics A*, 772(3-4):113–137, 2006.

[70] Juan Maldacena, Stephen H Shenker, and Douglas Stanford. A bound on chaos. *Journal of High Energy Physics*, 2016(8):1–17, 2016.

[71] Andreas Marek, Volker Blum, Rainer Johanni, Ville Havu, Bruno Lang, Thomas Auckenthaler, Alexander Heinecke, Hans-Joachim Bungartz, and Hermann Lederer. The elpa library: scalable parallel eigenvalue solutions for electronic structure theory and computational science. *Journal of Physics: Condensed Matter*, 26(21):213201, 2014.

[72] Petar Marević, Nicolas Schunck, Jørgen Randrup, and Ramona Vogt. Angular momentum of fission fragments from microscopic theory. *Physical Review C*, 104(2):L021601, 2021.

[73] Miguel AL Marques, Neepa T Maitra, Fernando MS Nogueira, Eberhard KU Gross, and Angel Rubio. *Fundamentals of time-dependent density functional theory*, volume 837. Springer, 2012.

[74] Joachim A Maruhn, P-G Reinhard, PD Stevenson, and A Sait Umar. The tdhf code sky3d. *Computer Physics Communications*, 185(7):2195–2216, 2014.

[75] Maria Goeppert Mayer. Nuclear configurations in the spin-orbit coupling model. ii. theoretical considerations. *Phys. Rev.*, 78:22–23, Apr 1950.

[76] Lise Meitner and Otto R Frisch. Products of the fission of the uranium nucleus. *Nature*, 143(3620):471–472, 1939.

[77] Arkadiĭ Migdal. Theory of finite fermi systems and applications to atomic nuclei.

[78] Luciano G Moretto, Graham F Peaslee, and Gordon J Wozniak. Angular—momentum—bearing modes in fission. *Nuclear Physics A*, 502:453–472, 1989.

[79] Luciano G Moretto and Richard P Schmitt. Equilibrium statistical treatment of angular momenta associated with collective modes in fission and heavy-ion reactions. *Physical Review C*, 21(1):204, 1980.

[80] James Rayford Nix and Wladyslaw J Swiatecki. Studies in the liquid-drop theory of nuclear fission. *Nuclear Physics*, 71(1):1–94, 1965.

[81] LW Nordhiem. On the kinetic method in the new statistics and application in the electron theory of conductivity. *Proceedings of the Royal Society of London. Series A, Containing Papers of a Mathematical and Physical Character*, 119(783):689–698, 1928.

[82] RE Peierls and J Yoccoz. The collective model of nuclear motion. *Proceedings of the Physical Society. Section A*, 70(5):381, 1957.

[83] R Navarro Perez, Nicolas Schunck, R-D Lasseri, C Zhang, and Jason Sarich. Axially deformed solution of the skyrme–hartree–fock–bogolyubov equations using the transformed harmonic oscillator basis (iii) hfbtho (v3. 00): A new version of the program. *Computer Physics Communications*, 220:363–375, 2017.

[84] GA Petrov. Current status of the search for scission neutrons in fission and estimation of their main characteristics. In *AIP Conference Proceedings*, volume 798, pages 205–212. American Institute of Physics, 2005.

[85] E Piasetzky, M Sargsian, L Frankfurt, M Strikman, and JW Watson. Evidence for strong dominance of proton-neutron correlations in nuclei. *Physical review letters*, 97(16):162504, 2006.

[86] William J Porter and Joaquín E Drut. Tan's contact and the phase distribution of repulsive fermi gases: Insights from quantum chromodynamics noise analyses. *Physical Review A*, 95(5):053619, 2017.

[87] Jørgen Randrup and Ramona Vogt. Generation of fragment angular momentum in fission. *Phys. Rev. Lett.*, 127:062502, Aug 2021.

[88] JO Rasmussen, W Nörenberg, and HJ Mang. A model for calculating the angular momentum distribution of fission fragments. *Nuclear Physics A*, 136(2):465–480, 1969.

[89] P. Ring and P. Schuck. *The nuclear many-body problem.* Springer-Verlag, New York, 1980.

[90] Erich Runge and E. K. U. Gross. Density-functional theory for time-dependent systems. *Phys. Rev. Lett.*, 52:997–1000, Mar 1984.

[91] Jhilam Sadhukhan, Witold Nazarewicz, and Nicolas Schunck. Microscopic modeling of mass and charge distributions in the spontaneous fission of ^{240}Pu. *Phys. Rev. C*, 93:011304, Jan 2016.

[92] Misak M Sargsian. New properties of the high-momentum distribution of nucleons in asymmetric nuclei. *Physical Review C*, 89(3):034305, 2014.

[93] MM Sargsian, TV Abrahamyan, MI Strikman, and LL Frankfurt. Exclusive electrodisintegration of he 3 at high q 2. ii. decay function formalism. *Physical Review C*, 71(4):044615, 2005.

[94] R. Sartor and C. Mahaux. Self-energy, momentum distribution, and effective masses of a dilute fermi gas. *Phys. Rev. C*, 21:1546–1567, Apr 1980.

[95] Guillaume Scamps and Cédric Simenel. Impact of pear-shaped fission fragments on mass-asymmetric fission in actinides. *Nature*, 564(7736):382–385, 2018.

[96] Guillaume Scamps, Cédric Simenel, and Denis Lacroix. Superfluid dynamics of fm 258 fission. *Physical Review C*, 92(1):011602, 2015.

[97] Rocco Schiavilla, Robert B Wiringa, Steven C Pieper, and J Carlson. Tensor forces and the ground-state structure of nuclei. *Physical review letters*, 98(13):132501, 2007.

[98] I. Stetcu. Github link for lise package. `https://github.com/lanl/LISE`, 2020.

[99] I. Stetcu, A. E. Lovell, P. Talou, T. Kawano, S. Marin, S. A. Pozzi, and A. Bulgac. Angular momentum removal by neutron and γ-ray emissions during fission fragment decays. *Phys. Rev. Lett.*, 127:222502, Nov 2021.

[100] Ionel Stetcu, CA Bertulani, Aurel Bulgac, Piotr Magierski, and KJ Roche. Relativistic coulomb excitation within the time dependent superfluid local density approximation. *Physical Review Letters*, 114(1):012701, 2015.

[101] JT Stewart, JP Gaebler, TE Drake, and DS Jin. Verification of universal relations in a strongly interacting fermi gas. *Physical Review Letters*, 104(23):235301, 2010.

[102] VM Strutinskii. Angular anisotropy of *gamma* quanta accompanying fission. *Zhur. Eksptl'. i Teoret. Fiz.*, 37, 1959.

[103] P. Talou, I. Stetcu, P. Jaffke, M.E. Rising, A.E. Lovell, and T. Kawano. Fission fragment decay simulations with the cgmf code. *Computer Physics Communications*, 269:108087, 2021.

[104] Shina Tan. Large momentum part of a strongly correlated fermi gas. *Annals of Physics*, 323(12):2971–2986, 2008.

[105] Lloyd N Trefethen. *Spectral methods in MATLAB*. SIAM, 2000.

[106] Naoto Tsuji, Tomohiro Shitara, and Masahito Ueda. Bound on the exponential growth rate of out-of-time-ordered correlators. *Phys. Rev. E*, 98:012216, Jul 2018.

[107] Edwin Albrecht Uehling and GE Uhlenbeck. Transport phenomena in einstein-bose and fermi-dirac gases. i. *Physical Review*, 43(7):552, 1933.

[108] R Vandenbosch and JR Huizenga. Isomeric cross-section ratios for reactions producing the isomeric pair hg 1 9 7, 1 9 7 m. *Physical Review*, 120(4):1313, 1960.

[109] Jerome M Verbeke, J Randrup, and R Vogt. Fission reaction event yield algorithm, freya—for event-by-event simulation of fission. *Computer Physics Communications*, 191:178–202, 2015.

[110] Marc Verriere and David Regnier. The time-dependent generator coordinate method in nuclear physics. *Frontiers in Physics*, 8:233, 2020.

[111] Marc Verriere, Nicolas Schunck, and David Regnier. Microscopic calculation of fission product yields with particle-number projection. *Physical Review C*, 103(5):054602, 2021.

[112] R Vogt and J Randrup. Event-by-event study of photon observables in spontaneous and thermal fission. *Physical Review C*, 87(4):044602, 2013.

[113] R. Vogt and J. Randrup. Angular momentum effects in fission. *Phys. Rev. C*, 103:014610, Jan 2021.

[114] CF von Weizsäcker. Zur theorie der kernmassen. *Zeitschrift für Physik*, 96(7):431–458, 1935.

[115] JB Wilhelmy, E Cheifetz, RC Jared, SG Thompson, HR Bowman, and JO Rasmussen. Angular momentum of primary products formed in the spontaneous fission of cf 252. *Physical Review C*, 5(6):2041, 1972.

[116] JN Wilson, D Thisse, M Lebois, N Jovančević, D Gjestvang, R Canavan, Matthias Rudigier, D Étasse, RB Gerst, L Gaudefroy, et al. Angular momentum generation in nuclear fission. *Nature*, 590(7847):566–570, 2021.

[117] Yongle Yu and Aurel Bulgac. Energy density functional approach to superfluid nuclei. *Physical review letters*, 90(22):222501, 2003.

[118] Wilhelm Zwerger. *The BCS-BEC crossover and the unitary Fermi gas*, volume 836. Springer Science & Business Media, 2011.